ELECTRONIC AND TRANSPORT PROPERTIES OF FUNCTIONALIZED CARBON NANOTUBES

Hyoungki Park

A dissertation submitted to the faculty of the University of North Carolina at Chapel Hill in partial fulfillment of the requirements for the degree of Doctor of Philosophy in the Department of Physics & Astronomy.

Chapel Hill

2006

Approved by

Advisor: Jianping Lu

Laurie E. McNeil

Lu-Chang Qin

Alfred Kleinhammes

Paul Tiesinga

ABSTRACT

Hyoungki Park: Electronic and transport properties of functionalized carbon nanotubes
(Under the direction of Jianping Lu)

Carbon nanotubes have received much attention in recent years due to their high structural stability and interesting electronic and transport properties. These novel properties can be utilized in many areas of applications. Many of these applications require modifications to pristine nanotubes. In particular, chemical functionalizations have been shown to be an attractive method to tailor some of electronic and mechanical properties. In this study, I present our computational study on electronic and transport properties of covalently side-wall functionalized carbon nanotubes. We found that functional-group-induced impurity states play important roles in modifying electronic and transport properties of nanotube near the Fermi level. A drastic difference has been found between monovalent and divalent functionalization cases. In monovalent functionalizations, the impurity states are located near the Fermi level and have strong effects on both electronic and transport properties. On the other hand, divalent functionalizations do not cause any significant disruption near the Fermi level due to rehybridization of two adjacent impurity states into bonding and antibonding states located relatively far away from the Fermi level. We believe that the covalent functionalization induced property changes provide a pathway for the band structure engineering, electronic, and chemical sensor applications of carbon nanotubes.

ACKNOWLEDGEMENTS

I would like to take this opportunity to sincerely thank my advisor Professor Jianping Lu for his guidance and support in the course of this work. He has witnessed and shaped my development as a scientist and I am very grateful to him for all he has done for me. He provided me with guidance when I needed it at the same time letting me explore and learn by myself.

I would also like to thank Dr. Jijun Zhao, who introduced me to the field of computational condensed matter physics, taught me computational skills, and supervised my initial research in this field. My gratitude also goes to Dr. Chih-Kai Yang for his encouragement, many comments, and suggestions about my work.

I am very much grateful to Professor Laurie E. McNeil and Professor Otto Zhou, who kindly helped and supported me in finding the next stage of my research career. Thanks also to the committee members for their valuable comments and supports. I have greatly profited from the wonderful environment of this department and would like to thank all the faculty and staff. Finally, I am thankful for computational support from UNC-Chapel Hill Academic Technology and Network. This work is supported by University Research Council of University of North Carolina at Chapel Hill, Office of Naval Research Grant (No. N00014-98-1-0597).

Hyoungki Park

July 2006

DEDICATION

I dedicate this dissertation to my family, especially…

to my precious Mom and Dad for all their unselfish love,
instilling the importance of hard work and higher education,
and having supported me all these years;

to my dear wife Hyunsoon for being the most understanding, loving,
caring, patient, supportive wife any man could ever want;

to the rest of my family for encouragement, support, helpfulness,
and believing in me

TABLE OF CONTENTS

Page

LIST OF FIGURES

LIST OF TABLES

Tables Page

Chapter 1

Introduction

Ever since their discovery in 1991 [1], carbon nanotubes (CNTs) have attracted considerable amount of attention. In particular, single-walled carbon nanotubes (SWNTs) have been at the forefront of novel nanoscale investigations due to their unique mechanical, electrical, and chemical properties. They have been thought to have a host of wide-ranging potential applications, for example, as field emitters, high-strength engineering fibers, chemical and electrochemical sensors, actuators, catalyst supports in heterogeneous catalysis, tips for scanning probe microscopy, gas storage media, and as molecular wires for the next generation of electronics devices [2-11]. However, several technical challenges need to be overcome before the extraordinary properties of these unique materials can be fully utilized. For example: (a) during fabrication of CNTs, unwanted byproducts such as carbon onions and turbostratic/amorphous graphite are also generally produced, and as produced SWNTs are typically bound into interwined bundles that exhibit very low solubility in either water or organic solvents; (b) the lack of control of diameter and/or chirality, the key geometrical and structural parameters which control electronic properties of these materials during fabrication; and (c) many of applications require modifications to the pristine nanotube to render it functionally active for the various applications. In this context, chemical functionalization is an especially attractive candidate to address such issues, as it can improve solubility and processibility and allows the unique properties of SWNTs to be coupled to those of other types of materials.

In general, chemical modification strategies have targeted SWNT defects, end caps, and sidewalls, as well as the hollow interior [12-14]. Representative approaches to derivatization include covalent chemistry of conjugated double bonds within the SWNT [15-17], noncovalent π-stacking [18, 19], covalent interaction at nanotube ends and defects [20], and wrapping of macromolecules [21-23]. Since the chemically functionalized nanotubes are expected to have mechanical or electrical properties that are different from those of the pristine nanotubes due to changes in electronic structure caused by tube-functional group interactions, they might be used as chemical sensors or nanometer-scale electronic devices, and the chemical modifications to the walls or ends of carbon nanotubes might be used to tailor the interaction of the nanotube with other entities, such as a solvent, a polymer matrix, or other nanotubes.

Despite the amazing progress in this field, electronic and transport properties of functionalized SWNTs are far from being fully understood. The purpose of the present work is to provide a comprehensive understanding of electronic and transport properties of covalently sidewall functionalized SWNTs. Most of the carbon nanotube chemistry arises from its inherent curvature and one can divide a nanotube into two different areas by curvature: caps and sidewalls. Caps, though more reactive, constitute a very small part of surface area for a typical nanotube with length in microns. The sidewalls are a little less strained and more inert, thus getting high degrees of functionalization has been a major issue. However, recent progress have made sidewall functionalization possible with a high ratio of the number of attached functional groups to the number of carbon atoms in the nanotube [24-

26], and opened up a new route to the development of novel materials and the critical applications of SWNTs.

I start by reviewing the basic physical and electronic properties of SWNTs. Next I survey the experimental progress achieved in nanotube sidewall functionalization toward their use as devices in biological and electronic setting in chapter three. Chapter four provides reviews of computational methods and models used in our numerical studies. In chapter five the results of our investigation on how the electronic properties of SWNTs are affected by covalent sidewall functionalizations are presented. The transport properties of functionalized metallic tube are discussed in chapter six. Chapter seven contains the summary and discussion on future research directions.

Chapter 2

Carbon Nanotubes

2.1 History and development of carbon nanotubes

In 1985, a confluence of events led to an unexpected and unplanned experiment with a new kind of microscope resulting in the discovery of a new molecule made purely of carbon. Buckyballs – sixty carbon atoms arranged in a soccer ball shape – had been discovered and the world of chemistry, not to mention the worlds of physics and material science, would never be the same. In fact, what had been discovered was not just a single new molecule but an infinite class of new molecules: the fullerenes. Each fullerene – C_{60}, C_{70}, C_{84}, etc. – possessed the essential characteristic of being a pure carbon cage, each atom bonded to three others as in graphite. Unlike graphite, every fullerene has exactly 12 pentagonal faces with a varying number of hexagonal faces (e.g., C_{60} has 20). Some fullerenes, like C_{60}, are spherical in shape, and others, like C_{70}, are oblong like a rugby ball. Dr. Richard Smalley recognized in 1990 that, in principle, a tubular fullerene should be possible, capped at each end, for example, by the two hemispheres of C_{60}, connected by a straight segment of tube, with only hexagonal units in its structure. In actuality, however, carbon nanotubes had been discovered 30 years earlier, but had not been fully appreciated at that time. In the late 1950s, Roger Bacon at Union Carbide, found a strange new carbon fiber while studying carbon

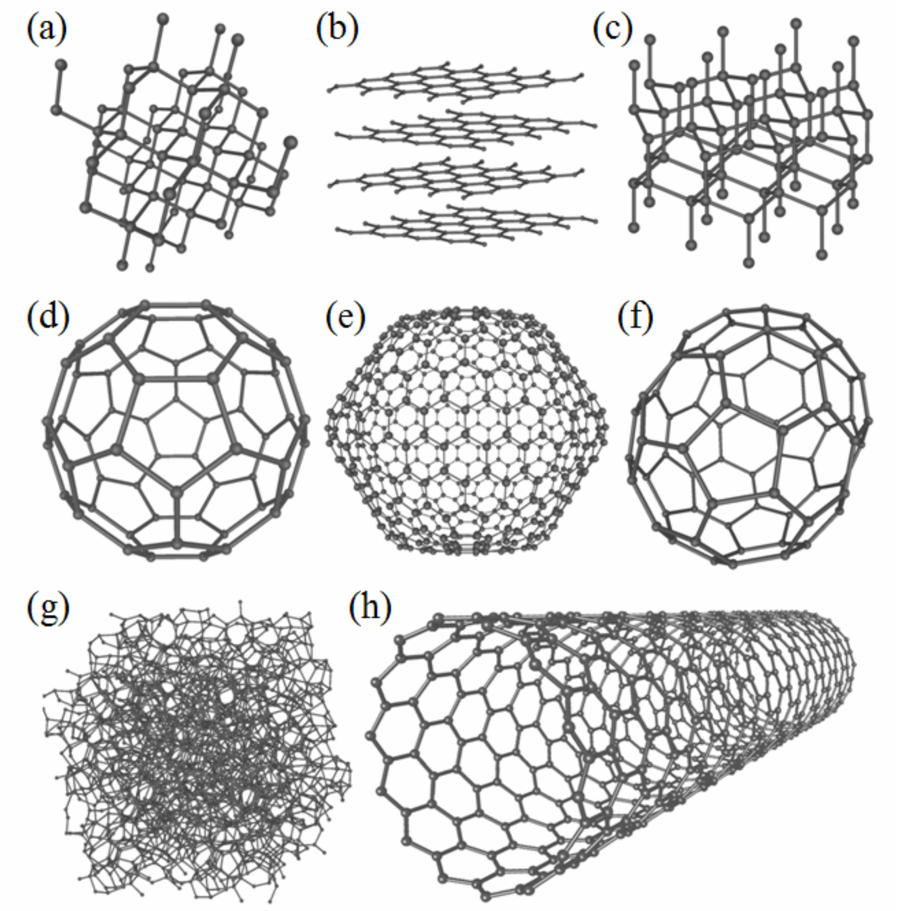

Figure 2.1: Various forms of carbon-based material: (a) Diamond, (b) Graphite, (c) Lonsdaleite, (d) Buckyball (C_{60}), (e) C_{540}, (f) C_{70}, (e) Amorphous carbon, and (h) SWNT. The picture was taken from Wikipedia, The Free Encyclopedia (accessed June 29, 2006), http://en.wikipedia.org/wiki/Carbon.

under conditions near its triple point. He observed straight, hollow tubes of carbon that appeared to consist of graphitic layers of carbon separated by the same spacing as the planar layers of graphite. In the 1970's, Morinobu Endo observed these tubes again, produced by a gas-phase process. Indeed, he even observed some tubes consisting of only a single rolled-up layer of graphite. In 1991, after the discovery and verification of the fullerenes, Sumio Iijima of NEC observed multi-wall nanotubes (MWNTs) formed in a carbon arc discharge [1], and two years later, he and Donald Bethune at IBM independently observed single-wall carbon nanotubes (SWNTs) [27, 28]. This was an important step forward, as the structure of a

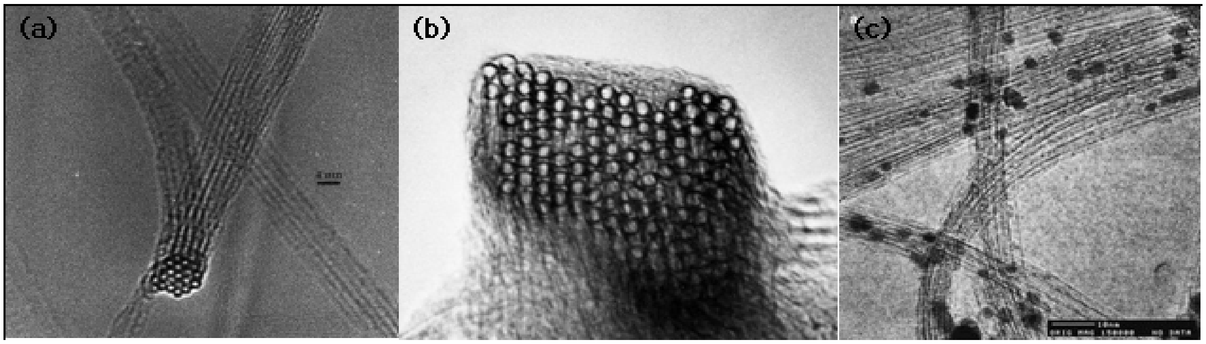

Figure 2.2: Synthetic methods for the production of single-walled carbon nanotubes: Transmission Electron Microscopy (TEM) images of (a) Electric arc discharge [29], (b) Laser ablation [30], and (c) HiPCO products [31].

SWNT is more basic than that of a MWNT and facilitates the study of its fundamental properties both theoretically and experimentally.

Today, MWNTs are prepared in large quantities by the chemical vapor deposition (CVD) process. SWNTs can be prepared in reasonably high yields by three techniques: arc-discharge of Ni-Y catalyzed graphite electrodes [29], laser ablation of Ni-Co catalyzed graphite targets [30] and vapor phase pyrolysis of CO and $Fe(CO)_5$ (HiPCO process) [31]. Carbon nanotube samples are always contaminated with impurities including amorphous carbon, residual metal catalyst and graphitic nano-particles. Thus the purification and chemical processing of carbon nanotubes remains as a key step in any application.

2.2 Geometrical structure of SWNTs

In 1992, it was theoretically predicted that the nanotubes can be metallic or semiconducting depending on the orientation of hexagons with respect to the nanotube axis (chiral angle) [32-34]. The prediction was quickly confirmed experimentally indirectly [35], and the direct confirmation came in 1998 [36, 37]. The structure of a SWNT can be conceptualized by wrapping a one-atom-thick layer of graphite (called graphene) into a

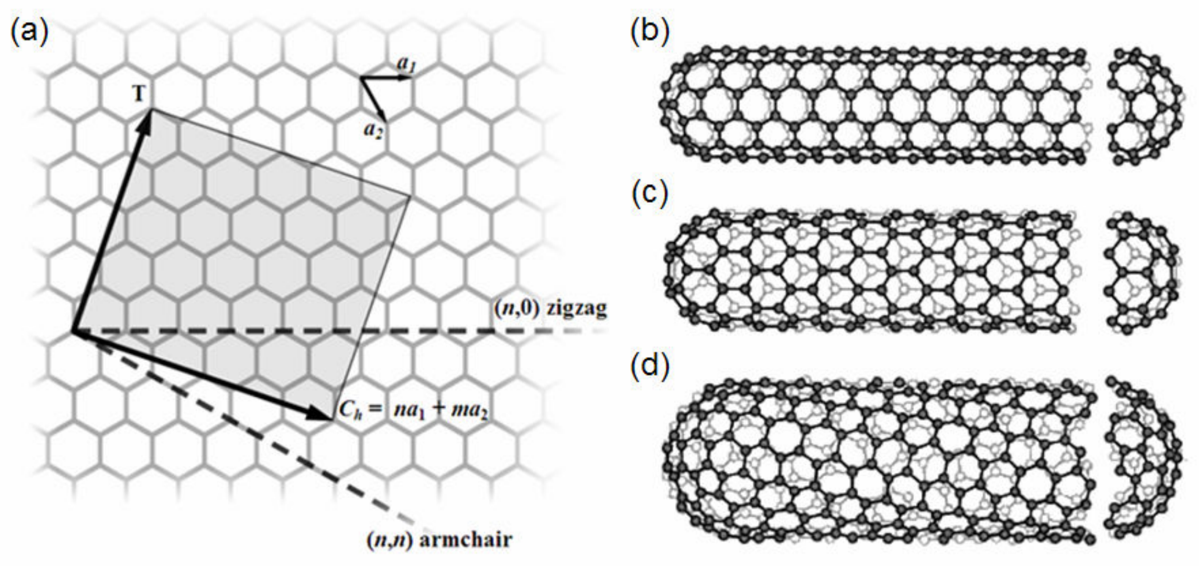

Figure 2.3: (a) Graphite sheet, the fabric of the nanotubes. Structure of a (b) armchair (c) zigzag (d) chiral SWNT.

seamless cylinder. The way the graphene sheet is wrapped is represented by the chiral vector C_h, which represents the full circumference of the tube. It is defined by

$$C_h = n\hat{a}_1 + m\hat{a}_2 \tag{2.1}$$

where $\hat{a}_1$ and $\hat{a}_2$ are the unit vectors in the hexagonal lattice, and n and m are integers (Figure 2.2 (a)). The so-called chiral angle which is the angle between C_h and $\hat{a}_1$. If $n = m$, the chiral angle is 30° and the structure is called *arm-chair* (Figure 2.2 (b)). If either n or m are zero, the chiral angle is 0° and the structure is called *zig-zag* (Figure 2.2 (c)). All other nanotubes show chiral angles between 0° and 30°. They are known as chiral nanotubes (Figure 2.2 (d)) because they produce a mirror image of their structure upon an exchange of n and m.

Experimentally, the diameter and the chiral angle of nanotubes can be determined by Transmission Electron Microscopy (TEM) (e.g. [38]), Scanning Tunneling Microscopy (STM) (e.g. [39]), or Atomic Force Microscopy (AFM) (e.g. [40]).

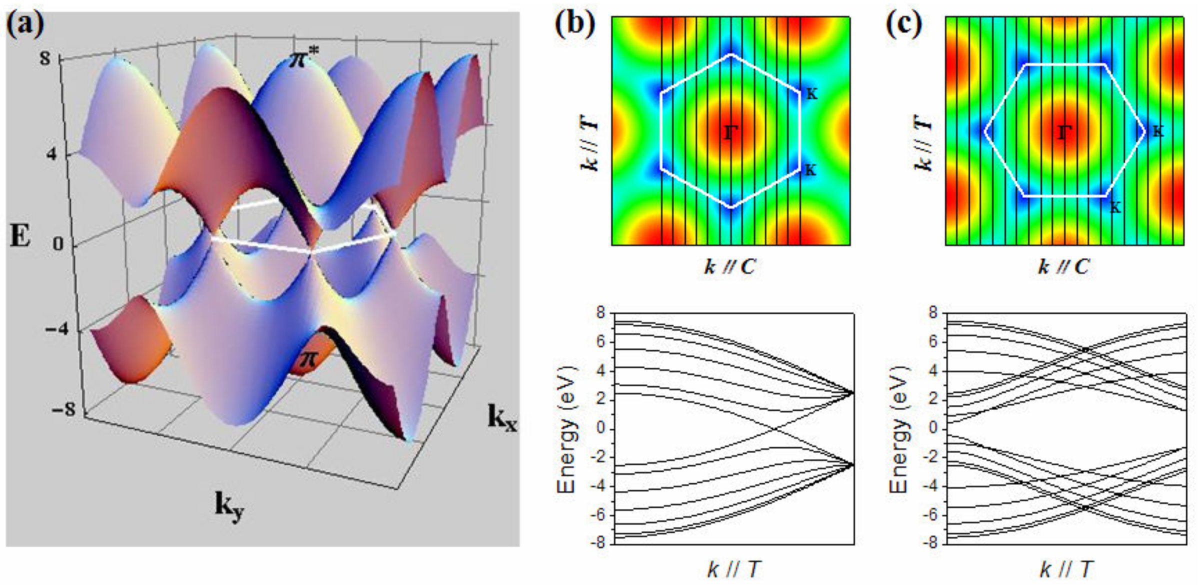

Figure 2.4: (a) Dispersion relation for graphene. Allowed k values and dispersion relations of (b) metallic (6, 6) armchair nanotube and (c) semiconducting (10, 0) zig-zag nanotube.

2.3 Electronic structure of SWNTs

Since nanotubes are just folded graphene, their electronic structure can be extracted from that of graphene. The electronic structure of graphene near the Fermi energy is given by an occupied π band and an unoccupied π* band. P. R. Wallace [41] derived an expression for the 2-D energy states of the π-electrons in the graphene plane as a function of the wave vectors k_x and k_y [42]:

$$E_{2D}(k_x,k_y)=\pm\gamma_0\sqrt{1+4\cos(\frac{\sqrt{3}k_xa}{2})\cos(\frac{k_ya}{2})+4\cos^2(\frac{k_ya}{2})} \tag{2.2}$$

where γ_0 denotes the nearest neighbor overlap integral and a = 0.246 nm is the in-plane lattice constant and two different signs represent the π and π* band. The calculations show the π and π* just touch each other at the corners of the 2-D Brillouin zone (*K* points). In the vicinity of Γ point (the center of Brillouin zone), the dispersion relation is parabolically shaped, while near the *K* points it shows a linear dependence on *k*. At T = 0 K, the π band is completely filled with electrons and the π^* band is empty. Because the bands only touch at the *K* points, integration over the Fermi surface results in a vanishing density of states (DOS). On the other hand, no energy gap exists in the graphene dispersion relation. This means we are dealing with a gapless semiconductor. (Yet real graphite is a metal since the bands overlap by approximately 40 meV due to the interaction of the graphene planes.)

For the description of the band structure of graphene, it is assumed that the graphene plane is infinite in 2-D. For carbon nanotubes, we have a structure which is macroscopic along the tube axis, but the circumference is in atomic dimensions. Hence, while the density of allowed states in axial direction will be high, the number of states in the circumferential direction will be very limited. More precisely, the roll-up by the chiral vector C_h leads to periodic boundary conditions in the circumferential direction. These boundary conditions define allowed modes along the tube axis according to:

$$C_h \cdot k = 2\pi j \quad \text{with} \quad |j| = 0, 1, 2, \ldots \quad . \tag{2.3}$$

The allowed *k* values depend on the diameter and helicity of the tube. Whenever the allowed *k* values include the point *K*, the system is a metal with a nonzero density of states at the Fermi level. When the *K* point is not included, the system is a semiconductor with different size energy gaps. It is important to note that the states near the Fermi energy in both metallic and semiconducting tubes originate in states near the *K* point, and hence their transport properties are related to the properties of the states on the allowed lines. In the case of armchair tubes, the tube axis is identical to the *y* direction and the circumference represents the *x* direction (in Figure 2.4(a) and in Equation 2.2). The periodic boundary condition allows values for the wave vector in the circumferential direction according to:

$$k_{x,j} = \frac{j}{n} \frac{2\pi}{\sqrt{3}a} \tag{2.4}$$

As an example of an armchair nanotube, Figure 2.4(b) shows the projection of the allowed 1D states onto the first Brillouin zone of the graphene and the band structure for a (6, 6) nanotube. In all armchair nanotubes the conduction band and the valence band cross at the Fermi energy for $k = 2\pi / 3a$ and show in general metallic behavior.

The periodic boundary conditions for zig-zag tubes result in allowed wave vectors according to:

$$k_{y,j} = \frac{j}{n}\frac{2\pi}{a} \tag{2.5}$$

The band structure and allowed k values for a (10, 0) zig-zag tube are shown in Figure 2.4(c). Note that for the (10, 0) tube K points are not among the allowed states and the tube is showing semiconducting behavior.

The general rules for the metallicity of the SWNT are as follows: (n, n) tubes are metals; (n, m) tubes with $n - m = 3j$, where j is a non zero integer, are very small-gap semiconductors and all others are large-gap semiconductors. Strictly within the band-folding scheme, the $n - m = 3j$ tubes would all be metals, but because of tube curvature effects, a very small gap opens near Fermi energy when $j \neq 0$ [43]. The armchair nanotubes are always metallic within the single electron picture, being independent of curvature because of their symmetry. As the tube radius R increases, the band gap of the large-gap and very small-gap tubes decreases as $1/R$ and $1/R^2$ respectively [33, 34, 44]. Thus, for most experimentally observed carbon nanotube sizes, the curvature induced energy gap of the very small-gap tubes is negligible and for most practical purposes all the larger diameter $n - m = 3j$ tubes can be considered metallic at the room temperature.

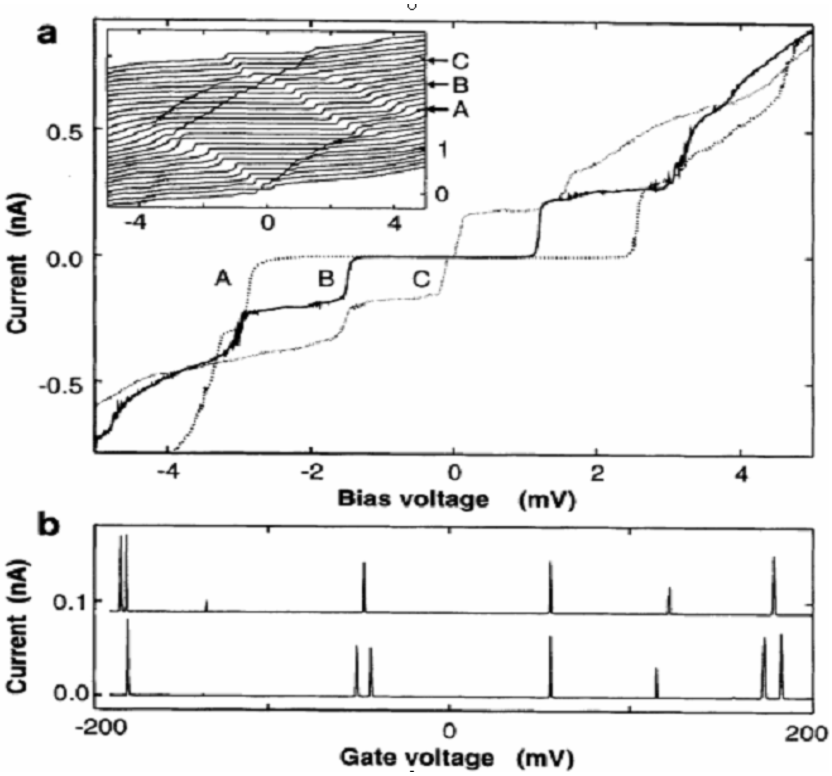

Figure 2.5: (a) $I - V_{bias}$ curve of a SWNT at a gate voltage of 88.2 mV (A) 104.1 mV (B) and 120 mV (C). In the inset more $I - V_{bias}$ curves are shown, with Vgate between 50 mV (bottom curve) and 136 mV (top curve). (b) $I - V_{gate}$ characteristic at $V_{bias} = 30\ \mu$V [45].

2.4 Transport properties of SWNTs

For metallic SWNTs, the dispersion relation around the Fermi energy is linear and the energetic separation between the modes at $\pm k_F$ is of the order of 100 meV. It is this large energetic spacing between the 1-D subbands which prevents interband scattering to a large extend even at room-temperature. Since there are subbands with positive and negative slope at both, + k_F as well as for - k_F, one expects a conductance

$$G = 2 \cdot \frac{2e^2}{h} \tag{2.6}$$

for an ideal, scattering free (ballistic) metallic nanotube. The degeneracy due to the spin is considered by a factor 2.

The experimental evidence of ballistic transport through a SWNT was first observed by Tans *et al* [45]. The experimental setup consisted in a SWNT deposited on a Si/SiO_2 substrate and atop two Pt electrodes, with an additional electrode (gate) used to change the electrostatic potential seen by the nanotube. The bias voltage V_{bias} is measured between the two leads and changes the chemical potentials of the two leads, μ_1 and μ_2. The gate potential V_{gate} changes the position of the energy levels of the nanotube relative to the chemical potentials μ_1 and μ_2. In Figure 2.5(a) the $I - V_{bias}$ curve is shown for three gate voltages. The plateaus of non-zero current clearly show ballistic transport when a conducting channel is in the range of $V_{bias} = (\mu_1 - \mu_2)/e$. The position of the steps is changed by increasing the gate voltage. However, we must consider not only the level-shift effect but also the Coulomb-charging effect of the nanotube, whereby the nanotube is considered as a capacitor with capacitance C. At very low temperature, such that the thermal energy is k_BT is smaller than the charging energy E_C of an electron $k_BT < E_C = e^2/2C$, the current flow can be blocked by this energy shift when the charge from the current flow itself shifts the levels out of the bias window between μ_1 and μ_2. Thus, current flow appears in Figure 2.5(b) only when $V_{bias} > E_C$. Since the energy of the levels in a nanotube can be modified by V_{gate}, the step positions shown in the inset of Figure 2.5(a) are smoothly changed by charging V_{gate}.

2.4.1 The elastic scattering at impurities

For 3-D metals, the probability of a scattering by impurities, i.e. the scattering rate, is described by the classical Rutherford scattering theory:

$$\tau_{imp}^{-1} \propto v_F \cdot \frac{1}{v_F^4} = v_F^{-3} \tag{2.7}$$

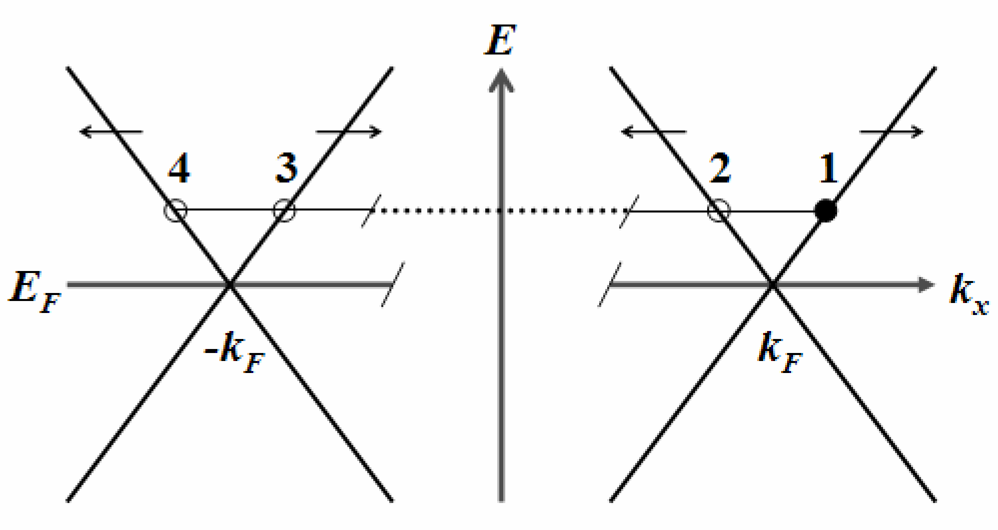

Figure 2.6: Illustration of impurity scattering processes on a metallic SWNT. Dispersion relation in the vicinity of $-k_F$ and $+k_F$. Position 1 (black circle) indicates an initial state of an electron, the position 2 to 4 are potential final states after scattering events.

where v_F denotes the Fermi velocity. In particular, τ_{imp}^{-1} is independent of temperature and proportional to the impurity concentration. This result relies on the fact that that the velocity of electrons in an interval of approx. $4k_BT$ around the Fermi energy is given by v_F in a very good approximation. This is in general a valid assumption for 3-D metals where E_F is large compared to k_BT. Eq. (2.7) holds exactly, if the dispersion relation is linear within the energy interval of approx. $4k_BT$. The condition is fulfilled for CNTs up to room temperature and above. Figure 2.6 is a magnification of the metallic SWNT dispersion relation in the vicinity of the Fermi position at $\pm k_F$. The arrows represent the Fermi velocities of the electrons. Scattering at an impurity is an elastic scattering process. Consequently, an electron can only be scattered in another state at the same energy of the nanotube dispersion relation. The allowed final states for an electron in an initial state at position 1 are indicated as 2 to 4 in Figure 2.6. The change in electron momentum is accounted for by the impurities. Due to the one-dimensionality of the system small-angle scattering as is present in 2-D or 3-D metals does not exist in SWNTs. While scattering from 1 to 3 represents a forward scattering event without effect on the conductance, scattering from 1 to 2 or 4 is a backscattering event and will increase the resistance. The two-terminal resistance of a SWNT segment of length L will be

$$R_{imp} = \frac{h}{4e^2} \cdot \frac{L}{\lambda_{imp}} \tag{2.8}$$

where λ_{imp} is the elastic mean free path which is roughly speaking the average distance between impurity centers. R_{imp} will be temperature independent in a good approximation. The typical values of λ_{imp} for CVD grown SWNTs are ~1 μm [46].

2.4.2 The electron-phonon scattering

For the discussion of the phonon scattering of electrons in SWNTs, we have to distinguish scattering by optical and acoustical phonons. The starting point for describing the latter is the linear dispersion of the acoustical phonons with $E_{ph} = \hbar c_{ph} k_{ph}$ [47]. Since the velocity of sound, c_{ph}, is approx. 10^4 m/s, i.e. about two orders of magnitude smaller than the

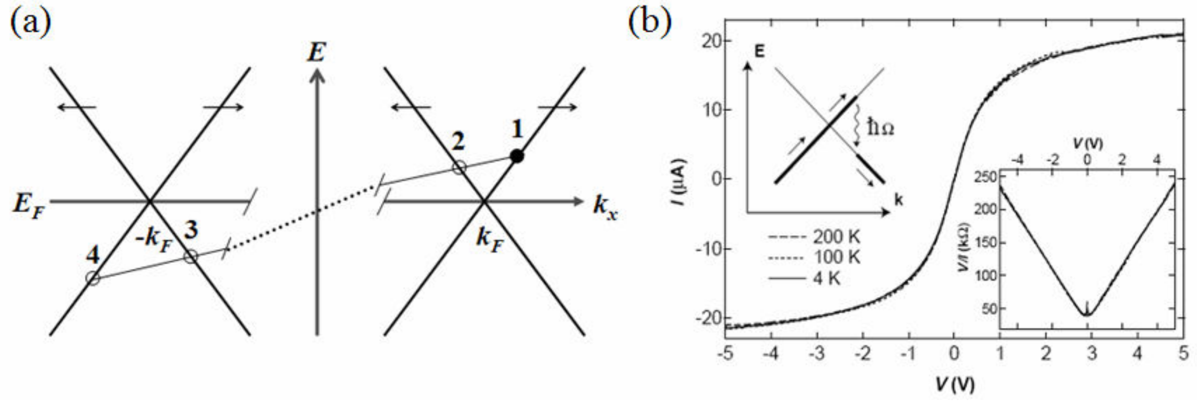

Figure 2.7: Electron-phonon scattering (a) illustration of an acoustic phonon scattering event on a metallic SWNT. Position 1 (black circle) indicates an initial state and position 2 is the final state after the scattering event. (b) High-field *I*-*V* characteristics for metallic CNTs at different temperatures. The right inset plot V/I = R vs. V. The left inset shows a section of the dispersion relation and illustrates the phonon emission [48].

Fermi velocity of the electrons ($v_F \sim 10^6$ m/s), the scattering of an electron by an acoustic phonon results in a rather small electron energy change. Figure 2.7(a) illustrates a possible final state 2 for an electron scattered by an acoustic phonon from an initial state 1. The two states are connected by a line with a slope (c_{ph}) much smaller than the one of the electron dispersion relation reflecting the aforementioned difference in velocity. Scattering from the crossed dispersion region around $+k_F$ to $-k_F$ is suppressed because there are no empty, allowed states available around $-k_F$ even at room-temperature. Approximately $2k_F$ has to be delivered by the phonon in order to have a scattering from $+k_F$ to $-k_F$. The corresponding phonon energy is ~100 meV which is much higher than k_BT even at room-temperature, and thus scattering from $+k_F$ to $-k_F$ is suppressed.

Since the Debye temperature of SWNTs is approx. 2000 K [48], the situation for $T <$ 300 K is described by the Grüneisen relation. For 3-D metals, the temperature dependence of the scattering rate is given by:

$$\tau_{ph}^{-1} \propto T^5 \tag{2.9}$$

which is composed of three factors. The first $\propto T^2$ comes from the density of phonon states in 3-D. The second $\propto T^2$ factor describes the small-angle scattering in 3-D metals. And finally, there is a $\propto T$ factor from the energy transfer between electron and phonon. For 1-D systems such as SWNTs, the first two terms can be ignored because the 1-D phonon DOS shows no temperature dependence and the small-angle scattering is not allowed in 1-D structures. Therefore the resistance contribution due to the acoustical phonon is given by:

$$R_{ph} = \frac{h}{4e^2} \cdot \frac{L}{\lambda_{ph}} \tag{2.10}$$

where $\lambda_{ph} = v_F \cdot \tau_{ph}$ and $\tau_{ph} \propto T^{-1}$. λ_{ph} is found to be ~1 μm [46, 49].

For small excess energies of the electrons (approx. $eV < 100$ meV), scattering by optical phonons can be neglected since there are no unoccupied states. For large dc biases, i.e. high fields, electrons in the SWNT are taking up energies well beyond values of k_BT, i.e. they become "hot". Interestingly, "hot" in this case does not mean that the electron velocity has increased. Because of the special situation of a linear dispersion relation, the velocity of the carriers remains constant while their energy increases. This changes the situation completely. In the case of hot electrons, scattering by optical phonons can be the main contribution to the overall resistance of CNTs. Figure 2.7(b) shows the high-field *I-V* characteristics of metallic SWNTs at different temperatures. The curves overlap almost completely, proving a temperature-independent behavior. For small voltages, approx. $V < 0.2$ V, the *I-V* characteristics exhibits a linear behavior. For larger voltages, it is strongly non-linear. For voltages approx. > 5V, the current exceeds 20 μA which corresponds to a current density of more than 10^9 A/cm^2. Furthermore, it seems that a saturation current I_0 is approached at large bias. The resistance shows a constant value R_0 at small bias and increases linearly for $V > 0.2$ V (the right inset in Figure 2.7(b)), i.e. it can be expressed by $R = R_0 + V/I_0$. This behavior can be explained by the inset in the left of Figure 2.7(b). Once an electron has gained enough energy to emit an optical phonon, it is immediately back-scattered. A steady state is approached in which the electrons moving forward direction have energies E_{opt} higher than the backward-moving ones. The saturation current can be derived as $I_0 = (4e^2/h)\cdot(E_{\text{opt}}/e)$. Using a value of approx. 160 meV [48], this leads to a saturation current of approx. 25 μA, in very good agreement with the experimental results. Accordingly, the mean free path l_{opt} for backscattering phonons is just the distance an electron needs to accumulate the threshold energy: $\lambda_{\text{opt}} = (E_{\text{opt}}/e)\cdot(L/V)$, where L denotes the electrode spacing and V the applied voltage, i.e. *V/L* is the electric field. If this is combined with a field-independent scattering term (i.e. from impurities) with a mean free path λ_{imp}, an overall empirical expression for the voltage dependent resistance can be obtained:

$$R = \frac{h}{4e^2} \cdot L\left(\frac{1}{\lambda_{imp}} + \frac{1}{\lambda_{opt}}\right) = \frac{hL}{4e^2\lambda_{imp}} + \frac{h}{4eE_{opt}} \cdot V\,. \tag{2.11}$$

Theoretical analysis and fitting of experimental data have revealed that λ_{opt} is ~ 15 nm [50].

2.4.3 The electron-electron scattering

An additional mechanism that leads to a resistance contribution is electron-electron scattering; a mechanism which may be especially pronounced in 1-D conductors. Typically, electron-electron scattering does not result in any measurable change in resistance of a normal conductor. This is true because energy and momentum conservation can only be fulfilled if as many electrons are backscattered as are scattered in the forward direction. The situation is drastically changed for a carbon nanotube. Figure 2.8 shows the dispersion

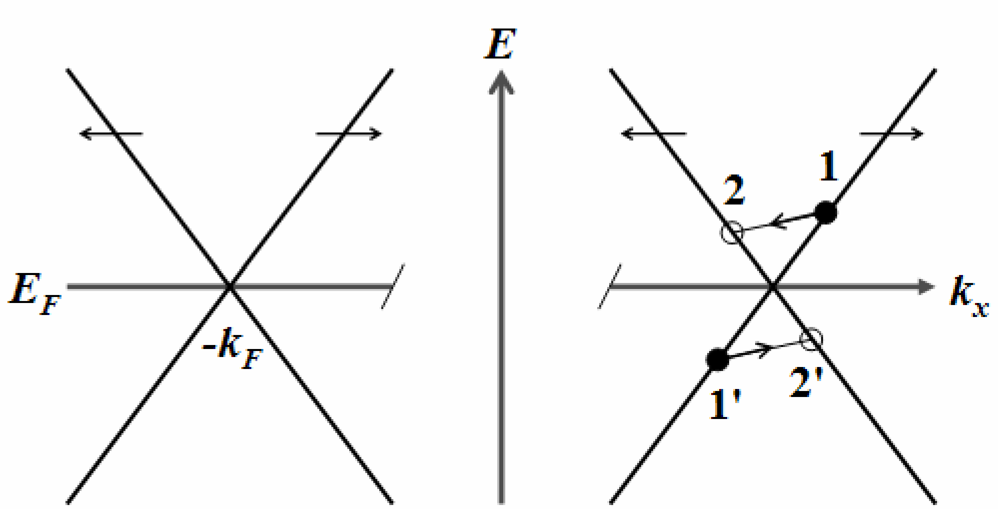

Figure 2.8: Illustration of electron-electron scattering event on a metallic SWNT. Dispersion relation is shown in the vicinity of $+k_F$. Positions 1 and 1′ (black circles) indicate initial states of two electrons, positions 2 and 2′ are final states.

relation in the vicinity of k_F. Because of the mode crossing, two electrons in positions 1 and 1′, which contribute to the forward transport, may get scattered into positions 2 and 2′, respectively. The total energy and momentum is conserved during this process. The scattered electrons in 2 and 2′ now occupy states in the negative current direction. Hence, this process leads to a resistance increase. With increasing temperature, the number of allowed initial and final states increases and so does the scattering probability. A detailed analysis [51] reveals a linear dependence of the electron-electron scattering rate on the temperature:

$$R_{e-e} = \frac{h}{4e^2} \cdot \frac{L}{\lambda_{e-e}} \text{ with } \tau_{e-e} \propto T^{-1} \tag{2.12}$$

where $\lambda_{e\text{-}e}$ is the mean free path between scattering events and $\tau_{e\text{-}e}$ is the inverse scattering rate. The scattering rate also rises with increasing electric excess energy, eV, of the electrons because the number of allowed states increases.

2.4.4 The transport in low temperature and low bias regime

In order to perform any kind of electrical measurement on a carbon nanotube it is essential to create some kind of contact between the tube and the outside world. The quality of the electrical contacts is of paramount importance for studying electric transport phenomena. With high contact resistance, individual SWNTs exhibit Coulomb blockade (CB) [45, 52, 53] and Luttinger liquid (LL) [54] behavior at various temperatures.

For metallic nanotubes exhibiting high contact resistance with the electrical leads, the low temperature transport is dominated by CB effect. CB occurs at low temperatures in systems with very small capacitance, such that adding a single electron requires an electrostatic energy $E_C = e^2/2C$, larger than the thermal energy k_BT. For an estimate, we can express the capacitance of a nanotube as $C = 2\pi\varepsilon_r \varepsilon_0 L \,/\, ln(2z/r)$ where ε_r is the average dielectric constant of the environment, z is the distance between the nanotube and the conducting substrate, L is the length of the tube and r is the radius of the tube. Assuming $\varepsilon_r \approx 2$, $z = 300$ nm and $r = 0.7$ nm for a typical nanotube, the charging energy will be $E_C \approx 5/L(\mu\text{m})$ meV. That means that for a nanotube sample of ~1 μm the Coulomb blockade will set in below 50 K.

It has been theoretically predicted that in 1-D systems such as metallic SWNTs electrons form a Luttinger liquid rather than a conventional Fermi liquid phase [55, 56]. LL behavior can be characterized by some exotic properties such as low-energy charge and spin excitations that propagate with different velocities, and a tunneling density of states that is suppressed as a power law function of energy, i.e. $\rho(E) \sim |\, E - E_F \,|^{\alpha}$. The strength of electron-electron interactions in a LL is described by Luttinger parameter g. For non-interacting electrons $g = 1$, whereas for repulsive Coulomb interactions $g < 1$. An estimate of the g parameter in nanotubes is found to be $g \approx 0.22$, which means that a carbon nanotube is a strongly correlated system. Experimental evidence for LL behavior in an individual SWNT has been reported in tunneling [54, 57, 58] and resonant tunneling measurements [59], revealing a pronounced suppression in the tunneling density of states.

It is interesting that for observing these CB or LL behaviors the poor contacts between the electrodes and the tube are needed; in fact, when highly transparent contacts were used, the conductance increased as the temperature decreased and neither CB nor LL were observed [60].

Our computational models for the study of transport properties of functionalized metallic SWNTs are connected to semi-infinite leads at both ends (described in chapter 4).

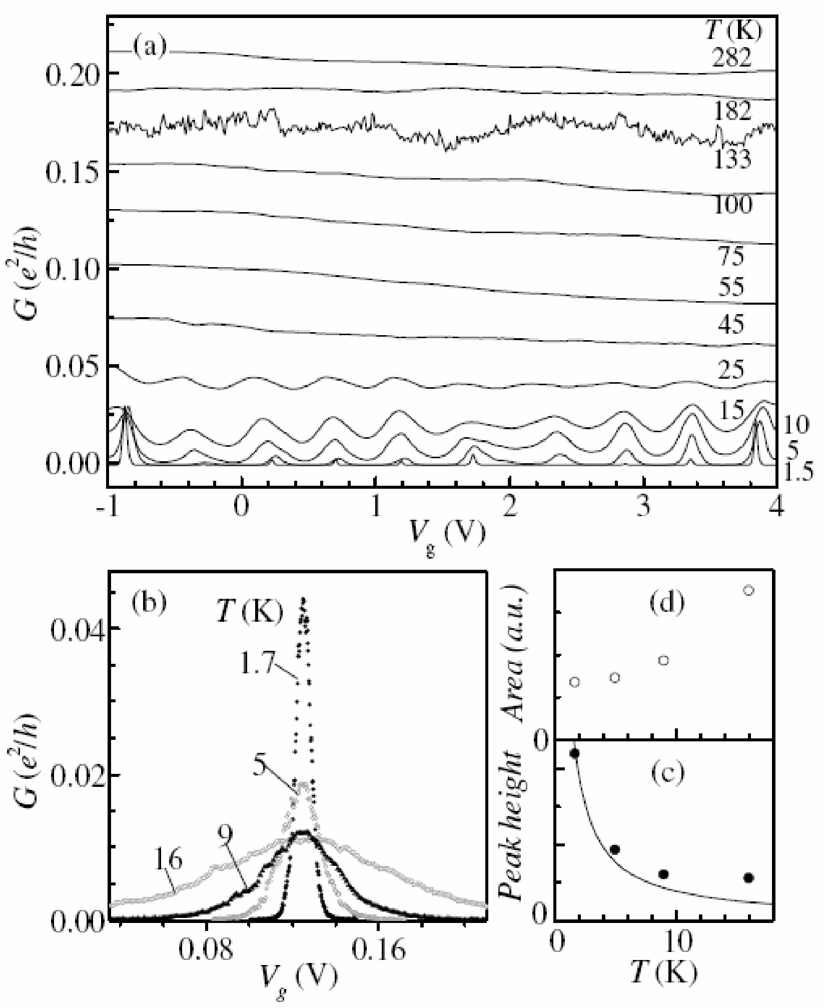

Figure 2.9: (a) Conductance *G* vs. gate voltage at temperatures from 282 K to 1.5 K for a metal-on-tube device. The device noise (conductance fluctuations in time) has been filtered from all traces except the one at 133 K where its amplitude is at a maximum. (b) Profile of a Coulomb blockade (CB) peak in another device between 16 K and 1.7 K. (c) Peak height vs. *T* for the peak in (b). The solid curve illustrates $G \approx 1/T$. (d) Peak area vs. *T* [53].

We have used the same metallic tubes for both semi-infinite leads and the functionalized section. Furthermore, our investigation of the transport properties is mainly focused on the low temperature and the low bias regime and the lengths of our computational models (< 10 nm) are much shorter than the electron-phonon scattering length scale of metallic nanotubes, which is about ~μm even at the room temperature. Therefore the electron-phonon scattering effect can be ignored. However, the electron-electron scattering effects may be important and further investigations may be required. In our calculations, the electron-electron interactions are not included so that the ballistic electron transport in SWNTs and the scattering mechanism at the functional sites are the only dominant factors that determine conducting behaviors of functionalized nanotubes in this regime.

Chapter 3

Covalent Sidewall Functionalization of SWNTs

Despite the extraordinary promise of SWNTs due to their outstanding structural and electronic properties, their realistic application in materials and devices has been hindered by processing and manipulation difficulties. Recently, various reliable methods of the chemical functionalization of the nanotubes have been developed to overcome those obstacles and extend the scope of application spectrum of SWNTs such as covalent interactions at dangling functionalities at nanotube ends and defects [20, 61], sidewall covalent modifications [15-17, 24-26, 62], and noncovalent modifications of SWNTs including polymer wrapping and adsorption [21, 23, 63], adsorption of amines [64] and molecules with large π-systems [18], forming complexes with organometallic compounds [65], and radio frequency glow-discharge plasma modification [66]. In particular, covalent modification schemes allow persistent alteration of the electronic properties of the tubes, as well as to chemical tailoring of their surface properties, whereby new functions can be implemented that cannot otherwise be acquired by pristine nanotubes. One can envision grafting of moieties that allow assembly of modified SWNTs onto surfaces for electronic applications, moieties that allow reaction with host matrices in composites, and sensing applications that may require the presence of a variety of functional groups bound to the SWNTs.

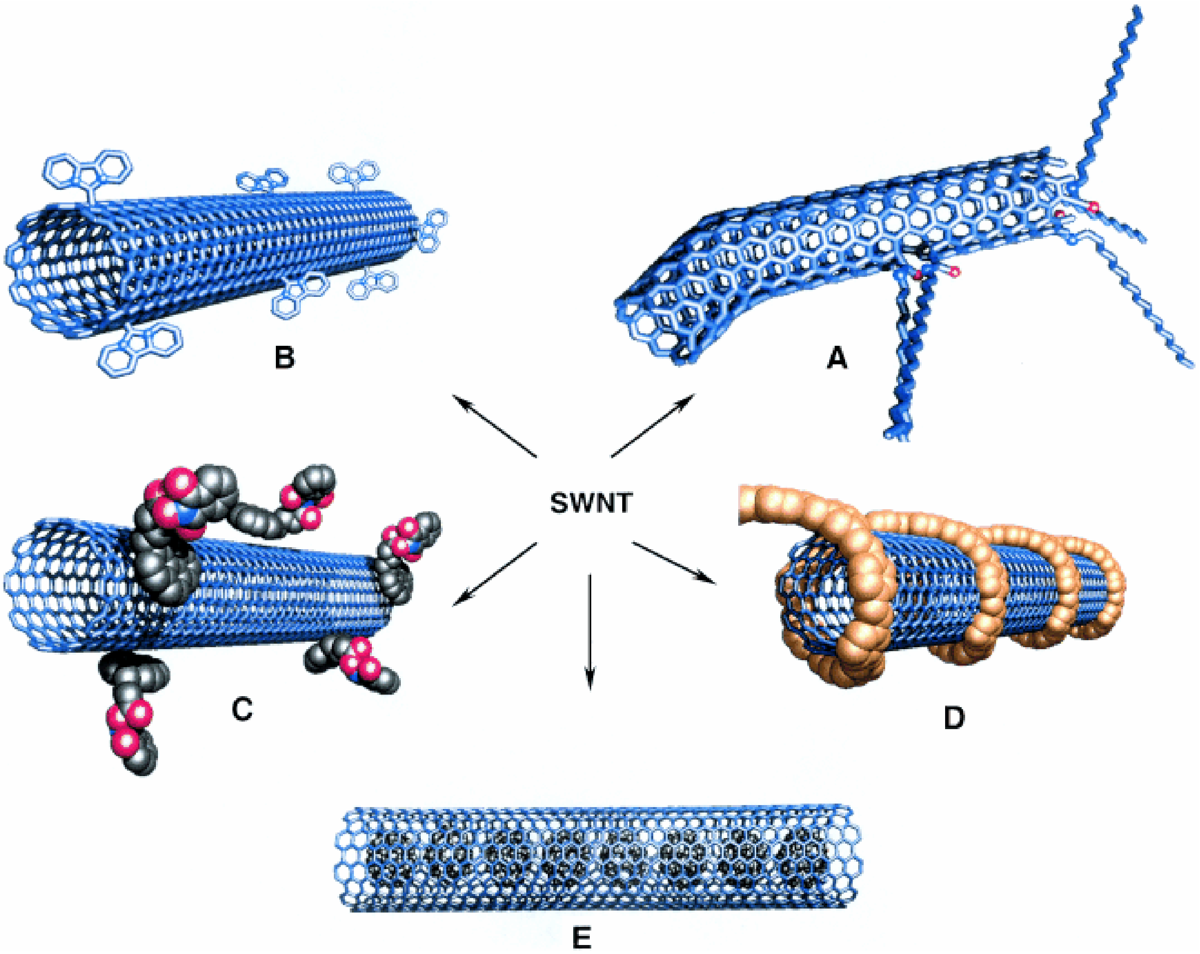

Figure 3.1: Functionalization possibilities for SWNTs: (A) defect-group functionalization, (B) covalent sidewall functionalization, (C) noncovalent exohedral functionalization with surfactants, (D) noncovalent exohedral functionalization with polymers, and (E) endohedral functionalization with, for example, C_{60} [12].

Although covalent functionalization methods have also been developed for MWNTs [67], fewer investigations have been devoted to this type of nanotube. Covalent functionalization of SWNTs has been accomplished by three different approaches, namely, thermally activated chemistry, electrochemical modification, and photochemical functionalization [68].

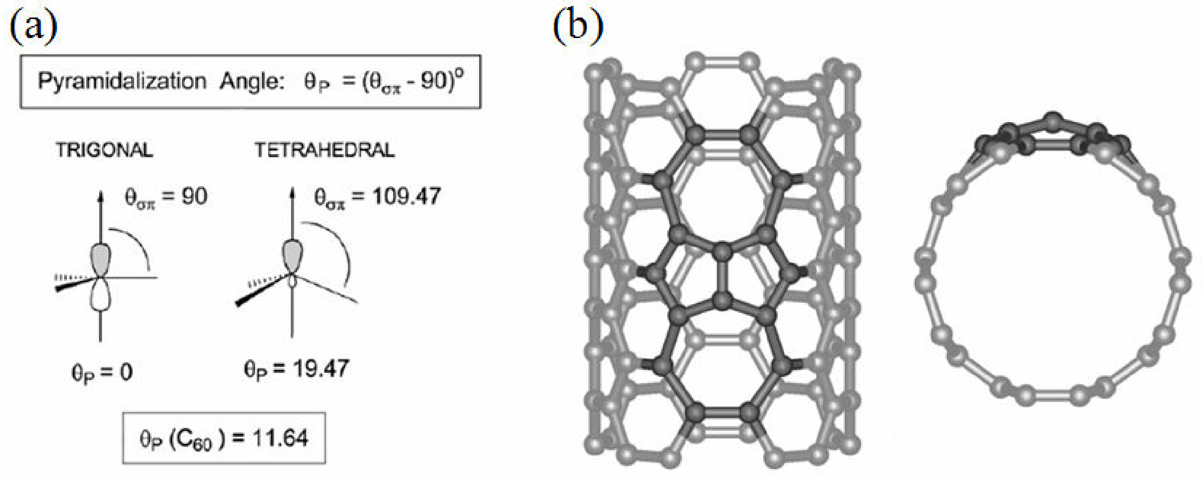

Figure 3.2: (a) Schematic diagram of pyramidalization angle θ_p [69] and (b) Stone-Wales (or 7-5-5-7) defect on the sidewall of a nanotube [68].

3.1 Origin of nanotube chemistry

Most of the carbon nanotube chemistry arises from its inherent curvature [69]. One can divide a nanotube into different areas by curvature, which reveals that nanotubes are essentially a two-component molecule with two terminal caps and a long, uniform cylinder. The caps resemble and chemically behave like fullerenes [70]. The caps are more reactive than the sidewall and prone to oxidation and addition reactions. In general, addition reactions to the partial carbon-carbon double bonds cause the transformation of sp^2 into sp^3 hybridized carbon atoms, which is associated with a change from a trigonal-planar local bonding geometry to a tetrahedral geometry. This process is energetically more favorable at the caps due to their pronounced curvature in two dimensions, in marked contrast to the sidewall with its comparatively low curvature in only one dimension. The theoretical basis for this argument is that curvature induces pyramidalization (strain) and misalignment of π orbitals [69]. As Figure 3.2(a) shows, regular sp^2-hybridized carbons have a 0° pyramidalization angle, θ_p, while regular sp^3-hybridized carbons have a θ_p of 19.47°. In, for example, the cap of a (10, 10) SWNT, the pyramidalization angle is $\theta_p = 11.64°$ (same as C_{60}), compared to $\theta_p = 3.01°$ of the sidewall. On the other hand, the non-zero curvature makes sidewall more reactive than a planar graphene sheet. Correspondingly, the binding energy of atoms or functional groups on the sidewall should increase with decreasing tube diameter. This tendency is supported by theoretical studies, as have been reported, for instance, for the bonding of radicals to the sidewall of a SWNT [71, 72]. On the contrary, the concave curvature of the inner surface of the nanotube imparts a very low reactivity towards addition reactions [73], so that carbon nanotubes have been proposed as nano-containers for reactive gas atoms, analogous to fullerenes encapsulating nitrogen atoms.

Typically, around 1~3% of the carbon atoms of a nanotube are located at defect sites [74]. A frequently-encountered type of defect is the so-called Stone-Wales defect, which is composed of two pair of five-membered and seven-membered rings, and is hence referred to as a 7-5-5-7 defect (Figure 3.2(b)). A Stone-Wales defect leads to a local deformation of the graphitic sidewall and thereby introduces an increased curvature in this region. The strongest curvature exists at the interface between the two five-membered rings; as a result of this curvature, addition reactions are most favored at these positions.

3.2 Thermally activated chemical functionalization

3.2.1 Oxidation and carboxyl-based couplings

An oxidation process for SWNTs involves extensive ultrasonic treatment in a mixture of concentrated nitric and sulfuric acid [20]. Such drastic conditions lead to the opening of the tube caps as well as the formation of holes in the sidewalls, followed by an oxidative etching along the walls with the concomitant release of carbon dioxide. The final products are

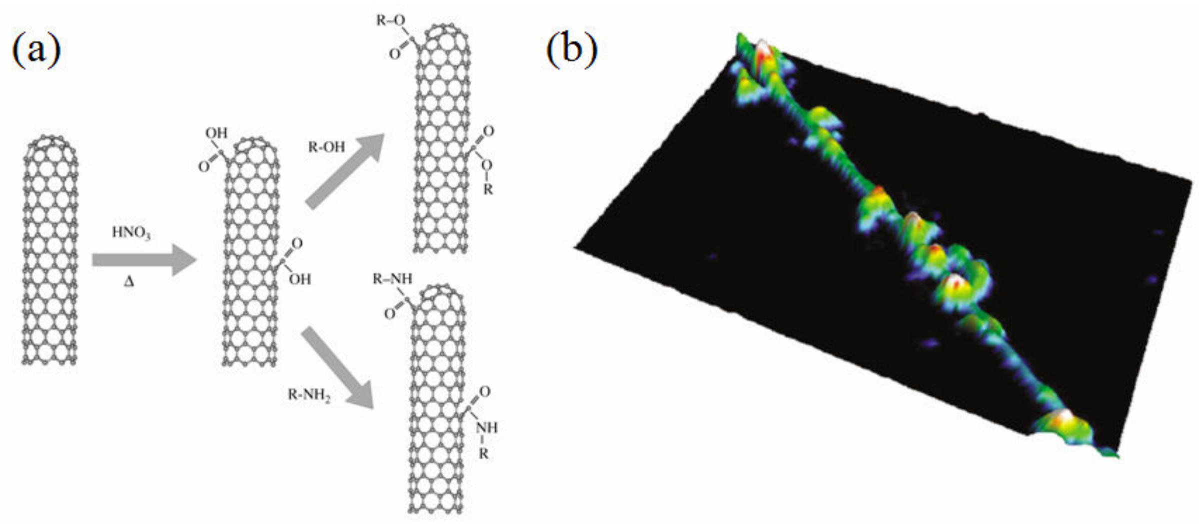

Figure 3.3: (a) Schematic diagram of chemical modification of nanotubes through thermal oxidation, followed by subsequent esterification or amidization of the carboxyl groups [68] and (b) AFM three-dimensional topographic representation of a single SWNT covalently decorated with gold nano-particles 2-3 nm in diameter [75].

nanotube fragments with lengths in the range of 100 to 300 nm, whose ends and sidewalls are decorated with a high density of various oxygen-containing groups (mainly carboxyl groups). Under less vigorous oxidation, such as refluxing in nitric acid, the shortening of the tubes can be minimized. The chemical modification is then limited mostly to the opening of the tube caps and the formation of functional groups at defect sites along the sidewalls. Nanotubes functionalized in this manner basically retain their pristine electronic and mechanical properties [61].

The oxidatively introduced carboxyl groups are useful sites for further modifications, as they enable the covalent coupling of molecules through the creation of amide and ester bonds (Figure 3.3(a)). By this method the nanotubes can be provided with a wide range of functional moieties, for which purpose bifunctional molecules (e.g., diamines) are often utilized as linkers. Illustrative examples are nanotubes equipped with dendrimers, nucleic acids, enzymes, metal complexes, or semiconductor and metal nanoparticles (Figure 3.3(b)) [75].

The presence of carboxyl groups leads to a reduction of van der Waals interactions between the CNTs. Additionally, the attachment of suitable groups renders the tubes soluble in aqueous or organic solvents, opening the possibility of further modifications through subsequent solution-based chemistry [76-78].

3.2.2 Addition reactions at the sidewall

The two-step functionalization of nanotubes through the oxidative introduction of carboxyl groups followed by the formation of amide or ester linkages does allow for a stable chemical modification, it has only a relatively weak influence on the electrical and mechanical properties of nanotubes. By comparison, addition reactions enable the direct coupling of functional groups onto the π-conjugated carbon framework of the tubes. The

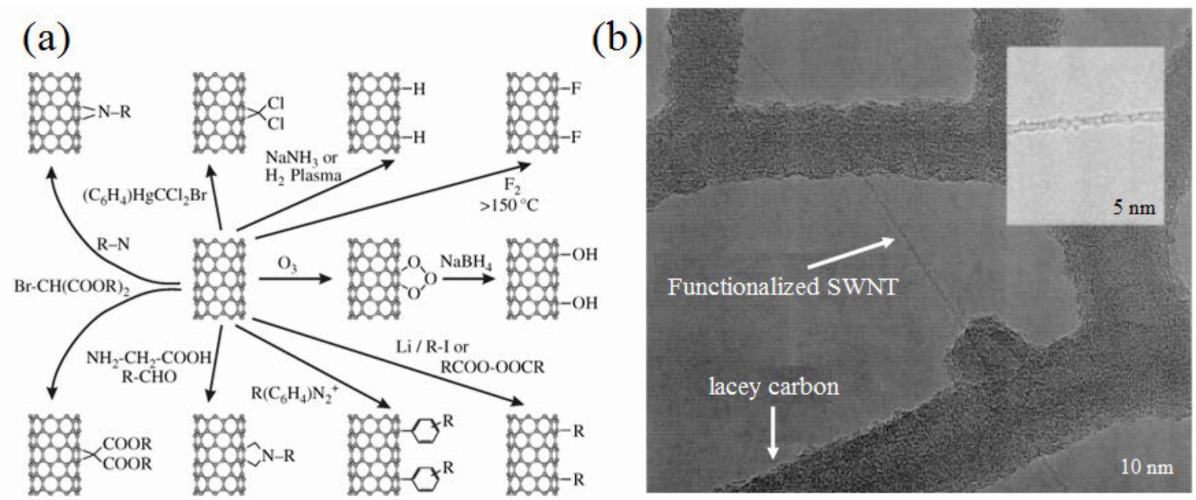

Figure 3.4: (a) Overview of possible addition reactions for the functionalization of the nanotube sidewall [68] and (b) TEM of 4-*tert*-butylphenyl-functionalized carbon nanotubes by the SDS/diazonium protocol. The insert is an expansion wherein the functional groups are clearly visible [79].

required reactive species (atoms, radicals, carbenes, or nitrenes) are in general made available through thermally activated reactions. A series of addition reactions have been well documented, the most important of which are listed in Figure 3.4(a).

While in the initial experiments aiming at addition reactions to the sidewall only one to three functional groups were found per 100 carbon atoms [12], the procedures of more recent development have reached at least a 10% degree of functionalization [79]. Analogous to nanotube functionalization with carboxyl groups, the direct covalent attachment of functional moieties to the sidewalls strongly enhances the solubility of the nanotubes. The good solubility of nanotubes modified with organic groups has been exploited for their effective purification [15]. In this procedure, small particles are first separated from the solution through chromatography or filtration, and then the covalently attached groups are removed through thermal annealing ($T > 250°C$).

3.2.3 Substitution reactions on fluorinated nanotubes

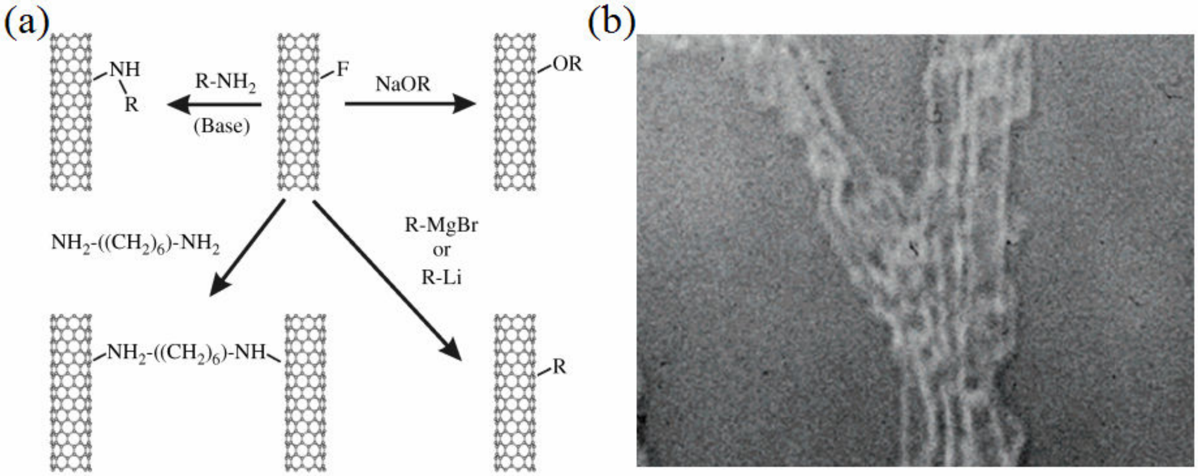

Figure 3.5: (a) Functionalization of the sidewall through nucleophilic substitution reactions in fluorinated nanotubes [68] and (b) TEM image zoomed-in on Undecyl ($C_{11}H_{23}$)-functionalized individual tubes [80].

The fluorine atoms in fluorinated carbon nanotubes can be replaced through nucleophilic substitution reactions with relative ease, thus opening a flexible approach for providing the sidewalls with various types of functional groups, as illustrated in Figure 3.5. As nucleophilic reagents, alcohols, amines, Grignard reagents, and alkyl lithium compounds have been successfully employed, which have resulted in up to a 15% degree of functionalization [80]. Moreover, by using a bifunctional reagent, such as an α, ω-diamine with a sufficiently long carbon chain, the nanotubes can be covalently cross-linked with each other [81].

3.3 Electrochemical modification of nanotubes

Interest in the study of the electrochemical properties of CNTs mainly stems from their superior electrocatalytic properties and their high surface-to-volume ratio, as compared to other carbon materials that are widely used as electrode materials. As a result of this interest, electrochemistry has been developed into an elegant tool for the functionalization of CNTs in a selective and controlled manner. To this end, a constant potential (potentiostatic) or a constant current (galvanostatic) is applied to a CNT electrode immersed in a solution that contains a suitable reagent, whereby a highly reactive (radical) species is generated through electron transfer between the CNT and the reagent. Many organic radical species have a tendency to react with the starting reagent or to self-polymerize, resulting in a polymer coating on the tubes. Depending on the reagent used, the polymeric layer may or may not be bonded in a covalent manner on the nanotube sidewall. Although the first electrochemical coupling were achieved with HIPCO-produced SWNTs, whose reactivity is enhanced by

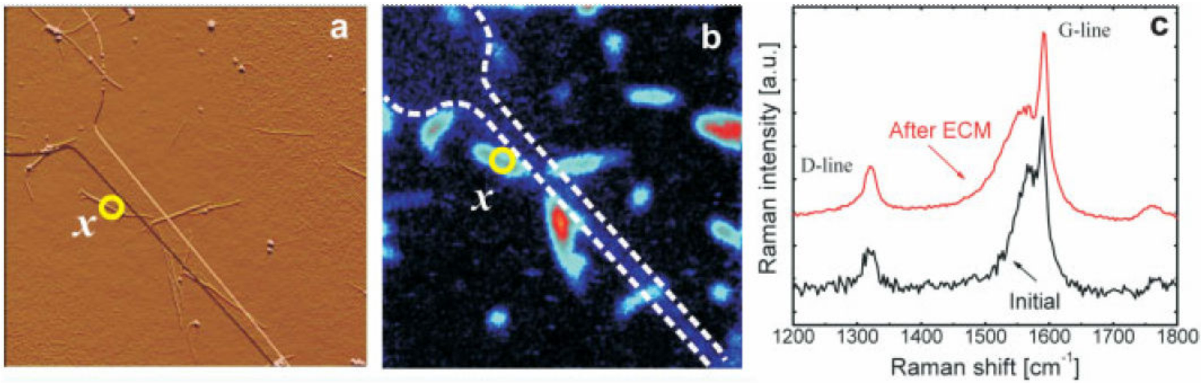

Figure 3.6: Characterization of SWNTs modified by oxidative ECM through confocal Raman spectroscopy: (a) AFM image of the sample showing an electrode and the SWNTs (8 µm × 8 µm); (b) a confocal G-line Raman image (10 µm × 10 µm) of the same sample taken with an excitation wavelength of 647.1 nm. The electrode structure is drawn in white, the background appears dark blue and the SWNTs appear as light blue to red regions; (c) Raman spectra showing the D-line and G-line of the SWNT marked ***x*** before and after ECM. The changes in the intensity and shift in the frequency of these two features are negligible in this case [82].

their small diameters of down to 0.6 nm [31], large-diameter nanotubes are also found to be amenable to covalent electrochemical modification under specific conditions [82].

In addition to being simple, clean, and efficient, electrochemical modification (ECM) schemes are quite versatile in that they allow for an accurate control over the extent of film deposition through the choice of suitable electrochemical conditions, that is, the duration and magnitude of the applied potential. Moreover, by utilizing reagents containing appropriate substituents, the surface properties of the coated tubes can be tailored, for example, from highly polar to predominantly hydrophobic. ECM has proven to be a suitable tool to modify entangled SWNTs networks as well as individual SWNTs.

3.4 Photochemical functionalization of nanotubes

Unlike the chemical functionalization routes based on thermally activated chemistry or ECM, photochemical approaches have been employed to a much less extent up to now. Only one true photochemical modification case has been reported to date, which is sidewall osmylation [83, 84]. Initially, it was observed that SWNTs exposed to osmium tetroxide (OsO_4) under UV-light irradiation show a pronounced increase in electrical resistance (Figure 3.7). This change has been ascribed to the photo-induced cycloaddition of OsO_4 to the partial carbon-carbon double bonds, as a result of which the π-electron density in the nanotubes is decreased. It is interesting to note that when humidity is carefully avoided, the OsO_4 addition is reversible, that is, the cycloadduct can be cleaved by photoirradiation, whereby the original resistance is restored.

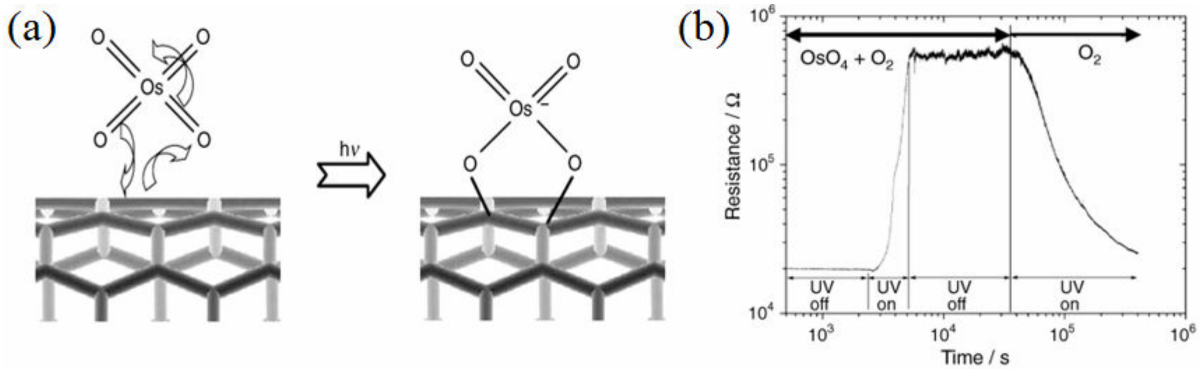

Figure 3.7: (a) Reaction scheme for sidewall osmylation of a SWNT using UV light; (b) resistance change of an individual metallic SWNT upon exposure to OsO_4 and O_2 under UV-light irradiation [84].

Chapter 4

Theoretical Approaches

In this chapter I will introduce a number of theoretical and computational techniques that are used in our studies of electronic and transport properties of covalently-sidewall-functionalized SWNTs. First, I will outline the general principles of density functional theory (DFT) and give an overview of tight-binding methods. Then a brief review of the basic concepts of Landauer-Büttiker formalism and Green's functions technique for transport property studies will be provided.

4.1 Density functional theory

Density functional theory belongs to a class of numerical methods known as *ab initio* methods. As their name implies, the only input to such methods are the fundamental constants of nature and the atomic numbers of the nuclei in the system. *ab initio* techniques aim to take into account all the interactions involving atoms and electrons of the system. Every electronic system can be described by a wavefunction according to the Schrödinger equation:

$$\hat{H}\,\Psi = E\,\Psi \tag{4.1}$$

where Ψ is the wavefunction for electrons and nuclei, E is the energy, and $\hat{H}$ is the Hamiltonian operator given by

$$H = -\sum_i \frac{\hbar^2}{2m_e}\nabla_i^2 - \sum_A \frac{\hbar^2}{2m_A}\nabla_A^2 - \sum_i\sum_A \frac{e^2 Z_A}{r_{iA}} + \sum_{i<j}\frac{e^2}{r_{ij}} + \sum_{A<B}\frac{e^2 Z_A Z_B}{r_{AB}} \qquad (4.2)$$

where i, j run over electrons, and A, B run over the nuclei. The wavefunction, Ψ, is then a function of $3N$ coordinates, where N is the total number of particles, electrons and nuclei. Unless otherwise stated, we shall henceforth use atomic units ($\hbar = e^2 = m_e = 1$), so that all energies are in Hartrees (27.2 eV) and all lengths in Bohr radii (0.53 Å).

As is evident, the motions of particles are coupled and none moves independently of the other. This presents a very complicated problem, making it impossible to solve exactly. For most systems, the problem can be simplified somewhat by making the Born-Oppenheimer approximation [85]. Since the nuclei move on a much longer time scale then the electrons, one can ignore the kinetic energy of the nuclei when solving for the electrons, and treat an electronic Hamiltonian (the inter-nuclear repulsion also becomes a constant) for each point on a potential energy surface.

4.1.1 The Hohenberg-Kohn theorems

As a result of the Born-Oppenheimer approximation, the Coulomb potential arising from nuclei is treated as a static external potential $V_{\text{ext}}(\mathbf{r})$:

$$V_{ext}(\mathbf{r}) = -\sum_A \frac{Z_A}{|\mathbf{r}-\mathbf{r}_A|}. \qquad (4.13)$$

We define the remainder of the electronic Hamiltonian given in (4.2) as $\hat{F}$:

$$\hat{F} = -\frac{1}{2}\sum_i \nabla_i^2 + \frac{1}{2}\sum_i\sum_{j\neq i}\frac{1}{|\mathbf{r}_i-\mathbf{r}_j|} \qquad (4.14)$$

such that $\hat{H} = \hat{F} + \hat{V}_{ext}$ where

$$\hat{V}_{ext} = \sum_i V_{ext}(\mathbf{r}_i) . \tag{4.15}$$

$\hat{F}$ is the same for all N-electron systems, so that the Hamiltonian, and hence the ground state $|\Psi_0\rangle$, are completely determined by N and $V_{\text{ext}}(\mathbf{r})$. The ground state $|\Psi_0\rangle$ for this Hamiltonian gives rise to a ground state electronic density $n_0(\mathbf{r})$

$$n_0(\mathbf{r}) = \langle \Psi_0 | \hat{n} | \Psi_0 \rangle = \int \prod_{i=2}^{N} \mathrm{d}\mathbf{r}_i | \Psi_0(\mathbf{r}, \mathbf{r}_2, \mathbf{r}_3 \cdots \mathbf{r}_N) |^2 . \tag{4.16}$$

Thus the ground state $|\Psi_0\rangle$ and density $n_0(\mathbf{r})$ are both functional of the number of electrons N and the external potential $V_{\text{ext}}(\mathbf{r})$. Density functional theory, introduced in 1964 by Hohenberg and Kohn [86], makes two remarkable statements.

The first Hohenberg-Kohn theorem states that the external potential $V_{\text{ext}}(\mathbf{r})$ is uniquely determined by the corresponding ground state electronic density, to within an additive constant. Thus, at least in principle, the ground state density determines (to within a constant) the external potential of the Schrödinger equation of which it is a solution. The external potential and number of electrons $N = \int \mathrm{d}\mathbf{r}\; n_0(\mathbf{r})$ determine all the ground state properties of the system since the Hamiltonian and ground state wavefunction are determined by them. So for all densities $n(\mathbf{r})$ which are ground state densities for some external potential (v-representable) the functional $F[n] = \langle \Psi | \hat{F} | \Psi \rangle$ is unique and well-defined, since $n(\mathbf{r})$ determines the external potential and N (and therefore $\hat{F}$) and hence $|\Psi\rangle$. Now a functional for an arbitrary external potential $V(\mathbf{r})$ unrelated to the $V_{\text{ext}}(\mathbf{r})$ determined by $n(\mathbf{r})$ can be defined:

$$E_V[n] = F[n] + \int \mathrm{d}\mathbf{r}\, V(\mathbf{r}) n(\mathbf{r}) . \tag{4.17}$$

The second, equally powerful theorem by Hohenberg and Kohn, is that for all *v*-representable densities $n(\mathbf{r})$, $E_V[n] \geq E_0$ where E_0 is now the ground state energy for *N* electrons in the external potential $V(\mathbf{r})$. Thus the problem of solving the Schrödinger equation for non-degenerate ground states can be recast into a variational problem of minimizing the functional $E_V[n]$ with respect to *v*-representable densities. It should be noted that simple counter-examples of *v*-representable densities have been found [87-89], but this restriction and the non-degeneracy requirement are overcome by the constrained search formulation.

4.1.2 The constrained search formulation

Following Levy [90] we define a functional of the density $n(\mathbf{r})$ for the operator $\hat{F}$ as:

$$F[n] = \min_{|\Psi\rangle \to n} \langle \Psi | F | \Psi \rangle \tag{4.18}$$

i.e. the functional takes the minimum value of the expectation value with respect to all states $|\Psi\rangle$ which give the density $n(\mathbf{r})$. For a system with external potential $V(\mathbf{r})$ and ground state $|\Psi_0\rangle$ with energy E_0, consider a state $|\Psi_{[n]}\rangle$, an *N*-electron state which yields density $n(\mathbf{r})$ and minimizes $F[n]$. Define $E_V[n]$ as:

$$E_V[n] = F[n] + \int \mathrm{d}\mathbf{r}\, n(\mathbf{r}) V(\mathbf{r}) = \langle \Psi_{[n]} | (\hat{F} + \hat{V}) | \Psi_{[n]} \rangle \tag{4.19}$$

but since $\hat{H} = \hat{F} + \hat{V}$, by the variational principle we obtain

$$E_V[n] \geq E_0 \tag{4.20}$$

with equality only if $\left|\Psi_{[n]}\right\rangle = \left|\Psi_0\right\rangle$. This holds for all densities which can be obtained from *N*-electron wavefunction (*N*-representable). But from the definition of $F[n]$ (4.8) we must also have

$$F[n_0] \leq \left\langle\Psi_0\middle|\hat{F}\middle|\Psi_0\right\rangle \tag{4.21}$$

since $\left|\Psi_0\right\rangle$ must be one of states which yields $n_0(\mathbf{r})$. Adding $\int \mathrm{d}\mathbf{r}\; n_0(\mathbf{r})V(\mathbf{r})$ gives

$$E_V[n_0] \leq E_0 \tag{4.22}$$

Which when combined with (4.10) gives the desired result that $E_V[n] \geq E_V[n_0] = E_0$.

Thus the ground state density $n_0(\mathbf{r})$ minimizes the functional $E_V[n]$ and the minimum value is the ground state electronic energy. Note that the requirement for non-degeneracy of the ground state has disappeared, and further that instead of considering only *v*-representable densities, we can now consider *N*-representable densities. The requirements of *N*-representability are much weaker and satisfied by any well-behaved density, indeed the only condition [91] is proper differentiability i.e. that the quantity $\int \mathrm{d}\mathbf{r}\, |\nabla n^{1/2}(\mathbf{r})|^2$ is real and finite.

4.1.3 Exchange and correlation

The remarkable results of density functional theory are the existence of the universal functional $F[n]$, which is independent of the external potential, and that instead of dealing with a function of 3*N* variables (the many-electron wavefunction) we can deal with a function of only three variables (the density). The complexity of the problem has thus been much reduced. The exact from of the universal functional $F[n]$ is unknown. The Thomas-Fermi functional [92-94]

$$F_{TF}[n] = \frac{3}{10}(3\pi^2)^{2/3}\int d\mathbf{r}\; n^{5/3}(\mathbf{r}) + \frac{1}{2}\int d\mathbf{r}\, d\mathbf{r}'\, \frac{n(\mathbf{r})n(\mathbf{r}')}{|\mathbf{r}-\mathbf{r}'|} \tag{4.23}$$

can be viewed as a tentative approximation to this universal functional, but fails to provide even qualitatively correct predictions for systems other than isolated atoms [95, 96] although recent, more accurate developments [97-101] have led to the implementation of linear-scaling orbital-free methods for nearly-free electron metals.

The failure to find accurate expression for the density functional is a result of the complexity of the many-body problem that is at the heart of the definition of the universal functional. For the electron gas, a system of many interacting particles, the effects of exchange and correlation are crucial to an accurate description of its behavior. In a non-interacting system, the anti-symmetry of the wavefunction requires that particles with the same spin occupy distinct orthogonal orbitals, and results in the particles becoming spatially separated. In an interacting system such as the electron gas in which all the particles repel each other, exchange will thus lead to a lowering of the energy. Moreover, the interactions cause the motion of the particles to become correlated to further reduce the energy of interaction. Thus it is impossible to treat the electrons as independent particles. These effects are completely neglected by the Thomas-Fermi model, and must in part account for its failure, the other source of error being the local approximation for the kinetic energy.

4.1.4 The Kohn-Sham equations

In order to take advantage of the power of DFT without sacrificing accuracy (i.e. including exchange and correlation effects), we follow the method of Kohn and Sham [102] to map the problem of the system of interacting electrons onto a fictitious system of non-interacting “electrons”. We write the variational problem for the Hohenberg-Kohn density functional, introducing a Lagrange multiplier μ to constrain the number of electrons to be N:

$$\delta\left[F[n] + \int \mathrm{d}\mathbf{r}\, V_{ext}(\mathbf{r})n(\mathbf{r}) - \mu\left(\int \mathrm{d}\mathbf{r}\, n(\mathbf{r}) - N\right)\right] = 0\,. \tag{4.24}$$

Kohn and Sham separated $F[n]$ into three parts

$$F[n] = T_S[n] + \frac{1}{2}\int \mathrm{d}\mathbf{r}\,\mathrm{d}\mathbf{r}'\,\frac{n(\mathbf{r})n(\mathbf{r}')}{|\mathbf{r}-\mathbf{r}'|} + E_{XC}[n] \tag{4.25}$$

in which $T_S[n]$ is defined as the kinetic energy of a non-interacting gas with density $n(\mathbf{r})$ (not the same as that of the interacting system, although we might hope that the two quantities were of the same order of magnitude), the second term is the classical electrostatic (Hartree) energy and the final term is an implicit definition of the exchange-correlation energy which contains the non-classical electrostatic interaction energy and the difference between the kinetic energies of the interacting and non-interacting systems. The aim of this separation is that the first two terms can be dealt with simply, and the last term, which contains the effects of the complex behavior, is a small fraction of the total energy and can be approximated surprisingly well.

Using this separation, equation 4.14 can be rewritten:

$$\frac{\delta T_S[n]}{\delta n(\mathbf{r})} + V_{KS}(\mathbf{r}) = \mu \tag{4.26}$$

in which the Kohn-Sham potential $V_{KS}(\mathbf{r})$ is given by

$$V_{KS}(\mathbf{r}) = \int \mathrm{d}\mathbf{r}'\,\frac{n(\mathbf{r}')}{|\mathbf{r}-\mathbf{r}'|} + V_{XC}(\mathbf{r}) + V_{ext}(\mathbf{r}) \tag{4.27}$$

and the exchange-correlation potential $V_{XC}(\mathbf{r})$ is

$$V_{XC}(\mathbf{r}) = \frac{\delta E_{XC}[n]}{\delta n(\mathbf{r})}\,. \tag{4.28}$$

The crucial point to note here is that equation 4.16 is precisely the same equation which would be obtained for a non-interacting system of particles moving in an external potential $V_{KS}(\mathbf{r})$. To find the ground state density $n_0(\mathbf{r})$ for this non-interacting system we simply solve the one-electron Schrödinger equation:

$$\left[-\frac{1}{2}\nabla^2 + V_{KS}(\mathbf{r})\right]\phi_i(\mathbf{r}) = \varepsilon_i\ \phi_i(\mathbf{r}) \tag{4.29}$$

for (1/2)N single particle states $\left|\phi_i\right\rangle$ with energies ε_i, constructing the density from

$$n(\mathbf{r}) = 2\sum_{i=1}^{N/2}\left|\phi_i(\mathbf{r})\right|^2 \tag{4.30}$$

(the factor 2 is for spin degeneracy – we assume the orbitals are single-occupied) and the non-interacting kinetic energy $T_S[n]$ from

$$T_S[n] = -\sum_{i=1}^{N/2}\int \mathrm{d}\mathbf{r}\ \phi_i^*(\mathbf{r})\nabla^2\phi_i(\mathbf{r})\,. \tag{4.31}$$

Since the Kohn-Sham potential $V_{KS}(\mathbf{r})$ depends on the density $n(\mathbf{r})$, it is necessary to solve these equations self-consistently i.e. having made a guess for the form of the density, the Schrödinger equation is solved to obtain a set of orbitals $\{\,\phi_i(\mathbf{r})\,\}$ from which a new density is constructed, and the process repeated until the input and output densities are the same. After self-consistency is achieved, the total energy can be found by

$$E = 2\sum_{i=1}^{N/2}\varepsilon_i - \frac{1}{2}\int \mathrm{d}\mathbf{r}\ \mathrm{d}\mathbf{r}'\ \frac{n(\mathbf{r})n(\mathbf{r}')}{\left|\mathbf{r}-\mathbf{r}'\right|} - \int \mathrm{d}\mathbf{r}\ n(\mathbf{r})V_{XC}(\mathbf{r}) + E_{XC}[n]\,. \tag{4.32}$$

4.1.5 Approximations of exchange-correlation functionals

Up to this point, we have given an exact recipe for calculation for the total energy of a system of electrons with the exception of the approximation of the exchange-correlation energy. There are different approximations for the exchange-correlation energy functional, $E_{XC}[n]$. Typical approximation functionals can be local, semi-local, non-local, or hybrid.

A local density functional depends only on the density at a particular point in space and contains no information about neighboring points. This is the simplest approximation that can be made. An example is the well-known and oft-used local density approximation [102] (LDA). This local approximation is exact for a uniform electron gas. The LDA functional works remarkably well despite its simplicity and is extensively used in solid state physics.

Semi-local functionals contain information, not only about the density at a certain point, but also about how the density varies near that point. Semi- and non-local approximations give better descriptions and, consequently, better energies for systems that are more rapidly varying. Generalized gradient approximations (GGA) are semi-local. Examples of popular GGAs are the PW91 [103] and PBE [104, 105] functionals which are also often used in solid state physics. Because they are non-empirical, they perform reliably and robustly for a wide variety of systems.

Hybrid functionals represent the exchange energy by a mix of DFT and exact exchange (Hartree Fock exchange). These are often empirical, but not always so. The very popular B3LYP functional [106, 107] is one such example.

4.1.6 Practical implementations of DFT calculations

The Kohn-Sham orbitals, ϕ_i, are usually expanded in terms of a convenient basis set as,

$$\phi_i(\mathbf{r}) = \sum_{\alpha} b_{\alpha}(\mathbf{r}) C_{\alpha i} \tag{4.33}$$

where $b_\alpha(\mathbf{r})$ are the basis functions and $C_{\alpha i}$ are the expansion coefficients. Among the bases usually chosen in calculations are plane-waves [108], Gaussian orbitals [109], wavelets [110],

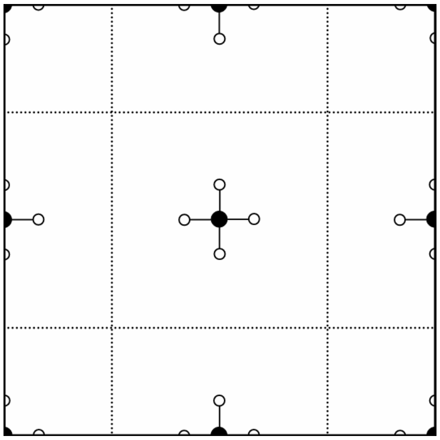

Figure 4.1: Schematic diagram of supercell approximation. Using the supercell, an isolated molecule can be studied using the same techniques which are usually applied to crystals.

and numerical bases [111, 112]. The choice of the particular basis depends on the system being studied. In our studies, we employed both plane-wave basis and numerical basis calculations. In the case of the plane-wave basis, an infinite number of plane-waves will be required to construct the exact wavefunctions of the system. To make computations possible, we truncate the above sum over basis functions and only work with those plane-waves whose energies are below a certain cutoff, on the premise that the wavefunctions are sufficiently smooth to be represented accurately by low-frequency plane-waves.

In the study of bulk crystals, the system is infinite but periodic, and so it is necessary to be able to reduce this problem to the study of a finite system. This approach turns out to have several advantages so that it is often easiest to study even aperiodic systems by imposing some false periodicity. The system is contained within a *supercell* which is then replicated periodically throughout space (see Figure 4.1). The supercell must be large enough so that the systems contained within each one, which in reality are isolated, do not interact significantly.

In most systems, especially in covalently bonded solids, most properties can be explained in terms of valence states, with the effect of the core states being small. This physical fact provides a motivation for yet another approximation that decreases the computational effort needed to compute system properties, namely the *pseudopotential approximation* [108]. Due to the strong interaction around atomic cores, wavefunctions exhibit high-frequency spatial oscillations in these regions that require the inclusion of high-frequency plane-waves in the basis set. To circumvent the problem of such a large basis set, the pseudopotential approximation replaces the ionic potential within a cutoff radius around the ions by a smoother potential. The oscillatory behavior of the valence wavefunctions near cores are also smoothed out at the end of this procedure. The new potential is generated to mimic exactly the scattering properties of the true potential outside of the cutoff. Pseudopotential theory is a broad area of research in itself. Examples of the most commonly used pseudopotentials are Kleinman-Bylander [113] and ultrasoft potentials [114].

4.2 Tight-binding total energy models

Empirical classical potential models have been applied extensively to model systems containing thousands to millions of atoms with great success. However, in situations where quantum mechanical effects are important, classical potentials often fail to produce meaningful results. For example, pair potentials fail to stabilize tetrahedral structures such as diamond and zincblende, since the directional covalent bonding in these systems is primarily determined by quantum mechanical effects. On the other hand, DFT-based *ab initio* techniques are very accurate and take the quantum mechanical effects into full consideration. However, *ab initio* methods are very computationally demanding. Consequently, even with the most powerful supercomputers available today, the largest system one can handle using *ab initio* methods is limited to the order of 1,000 atoms. The tight-binding (TB) method [115] takes an intermediate step towards modeling materials that takes into account quantum mechanical effects without too much computational effort.

4.2.1 Orthogonal tight-binding formalism

The idea of using a linear combination of atomic orbitals (LCAO) to represent the wavefunctions of aggregated of atoms (e.g. solids) was due to Bloch [116]. However, the success of modern orthogonal TB schemes should be credited to Slater and Koster [115], who presented the first detailed TB formalism for band structure calculations. In the following, we shall assume periodic boundary conditions (PBC). Extension to finite systems is straightforward.

Denoting an atomic orbital $n = (\tau, \alpha)$ at unit cell i as $\phi_n(\mathbf{r} - \mathbf{r}_\tau - \mathbf{R}_i)$, we have the Bloch sum

$$\Phi_{n\mathbf{k}} = \frac{1}{\sqrt{N}} \sum_{i=1}^{N} e^{i\mathbf{k}\cdot(\mathbf{r}_\tau + \mathbf{R}_i)} \phi_n(\mathbf{r} - \mathbf{r}_\tau - \mathbf{R}_i) \tag{4.34}$$

where the sum is over the atoms in equivalent positions in all unit cells in the crystal. τ is the atomic index in the cell and α specifies the atomic orbitals of atom τ. For example, in the diamond structure, $\tau = 1, 2$ and $\alpha = s, p_x, p_y, p_z$. We may express the wavefunctions of the system as linear combinations of Bloch sums. However, the Bloch sum formed from atomic orbitals is not an ideal basis, since atomic orbitals at different sites may not be orthogonal to each other. It is more convenient to work in a orthogonal basis, the so called Löwdin orbitals

$\psi_n(\mathbf{r})$, which are formed by reorthogonalization of atomic orbitals $\phi_n(\mathbf{r})$ [117]. We shall assume that such a reorthogonalization is done and rewrite the Bloch sum as

$$\Psi_{n\mathbf{k}} = \frac{1}{\sqrt{N}}\sum_{i=1}^{N} e^{i\mathbf{k}\cdot(\mathbf{r}_\tau + \mathbf{R}_i)}\psi_n(\mathbf{r} - \mathbf{r}_\tau - \mathbf{R}_i)\,. \tag{4.35}$$

The Hamiltonian matrix element between two Bloch sums with the same **k** is

$$\mathbf{H}_{n,n'}(\mathbf{k}) = \sum_{i=1}^{N} e^{i\mathbf{k}\cdot(\mathbf{r}_\tau + \mathbf{R}_i - \mathbf{r}_{\tau'})}\left\langle \psi_n(\mathbf{r} - \mathbf{r}_\tau)\middle| H \middle| \psi_{n'}(\mathbf{r} - \mathbf{r}_{\tau'})\right\rangle . \tag{4.36}$$

In the above equation, the sum has to be carried out over all unit cells in principle. In practice, one always assumes that the matrix element $\langle \psi_n | H | \psi_{n'} \rangle$ is short-ranged and decays to zero beyond some cut-off distance [118-120]. The matrix elements $\langle \psi_n | H | \psi_{n'} \rangle$ in the TB formalism are modeled by some empirical parameters which are either obtained by fitting experimental data or from more accurate *ab initio* calculations. Eigenvalues and corresponding wavefunctions are then calculated by diagonalizing the Hamiltonian matrix **H**. This is the original Slater-Koster TB model [115].

The Slater-Koster TB formalism computes only the band energies. For atomistic simulations, the total energy of the system must also be derived. Chadi [118] proposed that the total energy of a system in the TB framework can be written as a band structure energy plus a sum of pair-wise repulsive potentials. This is consistent with the LDA expression of the total energy, which is a sum of the band energy and some potential contributions. The idea that the terms in the total energy which are not included in the single-electron band energy can be approximated by a sum of pair terms is of great importance and is almost universally applied. The force acting on an atom in the TB formalism contains two terms, one arising from the band structure energy and the other from the repulsive potential energy.

4.2.2 Nonorthogonal tight-binding models

The orthogonal TB model is conceptually simple and computationally efficient. However, it shares with other empirical potential methods a serious drawback, the lack of transferability. The assumption that an orthogonal set of orbitals can be constructed from the nonorthogonal atomic orbitals by the Löwdin procedure is not universally valid, i.e., an orthogonal transformation is valid only for a single configuration of the system. Furthermore, the Löwdin orbitals are usually more extended than the nonorthogonal atomic orbitals, which require that the Hamiltonian matrix element $\langle \psi_n | H | \psi_{n'} \rangle$ be longer-ranged. The usual short-ranged TB parameterization is therefore not expected to work well across different environments. Failure to properly account for the overlap effects is probably the main reason for the lack of transferability of orthogonal TB models, although other issues such as the two-center approximation of the Hamiltonian matrix element, the pair-wise repulsive potentials, and lack of self-consistency are also important factors. The transferability can be improved somewhat by including a wider range of empirical data; however the improvement is limited and not systematic. Dorantes-Dávila *et al.* [121, 122] have proposed an iterative scheme to incorporate in an orthogonal TB framework the effects of the overlaps of atomic orbitals. A different approach is the so-called nonorthogonal TB model. As its name tells, this approach eliminates the assumption of orthogonality so that most of the drawbacks associated with this assumption can be overcome. The effect of neglecting the nonorthogonality of the basis has been investigated by Mirabella *et al.* [123] and Mckinnon and Choy [124].

In the nonorthogonal TB model, one has to solve the generalized eigenvalue problem

$$(\mathbf{H} - E_i \mathbf{S})\Psi_i = 0 \qquad (4.37)$$

where **S** is the overlap matrix between TB orbitals,

$$S_{i,j} = \int \mathrm{d}\mathbf{r}\ \phi_i(\mathbf{r})\phi_j(\mathbf{r}) \tag{4.38}$$

and ϕ are nonorthogonal atomic TB orbitals as opposed to the orthogonalized Löwdin orbitals ψ. The repulsive part of the total energy is usually assumed to be pair-wise as in the orthogonal TB models.

In our calculations, the on-site (diagonal) Hamiltonian matrix elements are taken as the atomic ionization potentials of the corresponding orbitals as usual, i.e. $H_{i,i} = \varepsilon_i$ and the off-diagonal elements are calculated from overlap matrix elements $S_{i,j}$ using extended Hückel approximation [125]:

$$H_{i,j} = \frac{1}{2} K S_{i,j}(H_{i,i} + H_{j,j}) \tag{4.39}$$

An exponential distance-dependent Wolfsberg-Helmholz parameter *K* proposed by Anderson is used in our model [126],

$$K = K_0 e^{-\delta(r-r_0)} \tag{4.40}$$

where $\delta = 0.13$ Å^{-1}, r is the interatomic distance, r_0 is the equilibrium bond length. K_0 is set to be 1.75 which is the typical value used in most extended Hückel calculations. The overlap matrix elements $S_{i,j}$ are evaluated based on the two-center overlap integrals over Slater-type orbitals (STOs) defined as:

$$\phi = N r^{n-1} e^{-\zeta r} Y_l^m(\theta,\varphi) \tag{4.41}$$

where *N* is the normalization constant, n is the principal quantum number of the orbital, ζ is called the orbital exponent, and $Y_l^m(\theta,\varphi)$ is the angular part of the orbital. These atomic orbitals are approximate solutions to the eigenvalue equation and they have no radial nodes unlike the hydrogen like orbitals.

4.3 Landauer-Büttiker formalism

When electrons move in a material they scatter from impurities, other lattice defects and from phonons. The scattering causes the electrical resistance. In normal-size electronic components this resistance follows Ohm's law, so that the conductance G is inversely proportional to the length L of the device.

$$G = \sigma \frac{A}{L} \tag{4.42}$$

where the conductivity σ is a material parameter independent of the sample dimensions and L and A are the length and the cross-sectional area of the conductor respectively. Ohm's law is understandable, because typically the scatterers are uniformly distributed into the material. A longer device has also more scatterers to destroy the collective electron drift movement. If we make the device smaller the number of scatterers diminishes. In this work, we consider very small-scale systems. In this regime it is not surprising that the statistical Ohm's law is not valid and other theories have to be used.

4.3.1 Landauer formula

If the ohmic scale relation were to hold as the length is reduced, we would expect the conductance to grow indefinitely. Experimentally, however, it is found that the measured conductance approaches a limiting value G_C, when the length of the conductor becomes much shorter than the mean free path $L << L_m$. Since a ballistic conductor (a conductor with

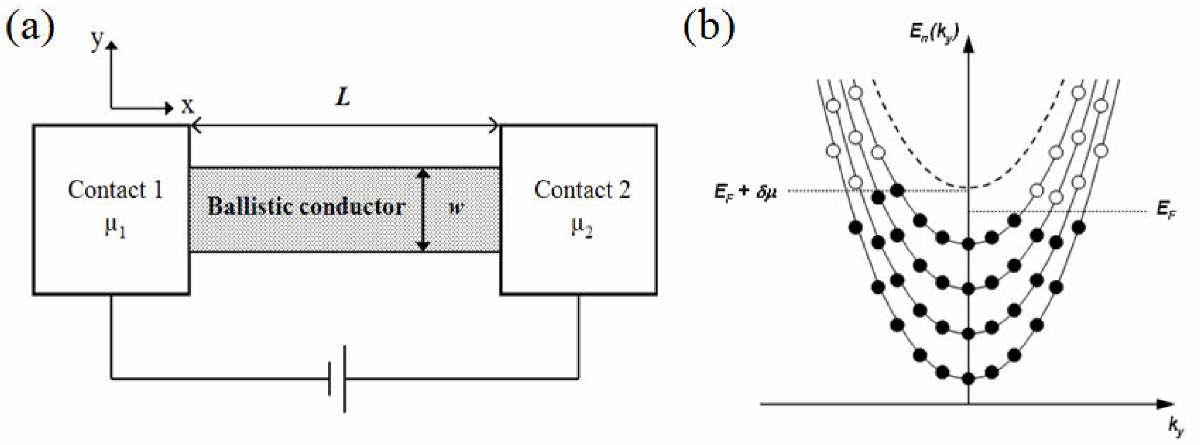

Figure 4.2: Schematic diagrams of (a) a ballistic conductor connected to two contacts across which an external bias applied. The contacts are assumed to be reflectionless. (b) Dispersion relation for different transverse modes in the narrow conductor.

no scattering) should have zero resistance, this resistance arises from the interface between the conductor and contact pads (Figure 4.2(a)), which are dissimilar materials in terms of their electronic structures. This causes a redistribution of the current at the interfaces leading to the interface resistance (contact resistance $R_C = G_C^{-1}$).

Based on the assumptions of reflectionless contacts and small bias voltages, we can calculate the contact resistance. The states in the narrow conductor belong to different transverse modes. Each mode has a dispersion relation $E(N, k)$, Figure 4.2(b), with a cut-off energy $\varepsilon_N = E(N, k = 0)$ below which it cannot propagate (N is the index of the subband). At a given energy E only the modes with a cut-off energy $\varepsilon_N < E$ participate in conduction. The number of conducting mode will be $M(E)$. We can evaluate the current carried by each transverse mode separately and add them up.

Consider a single transverse mode whose $+k$ states are occupied according to some function $f^{+}(E)$. A uniform electron gas with n electrons per unit length moving with a velocity v carries a current env. The linear electron density associated with a single k state in a conductor of length L is $1/L$, therefore we can write the current I^{+} carried by the $+k$ states as

$$I^{+} = e\sum_{k}\frac{1}{L}vf^{+}(E) = \frac{e}{L}\sum_{k}\frac{1}{\hbar}\frac{\partial E}{\partial k}f^{+}(E). \tag{4.41}$$

Assuming periodic boundary conditions and converting the sum over k into an integral

$$I^{+} = \frac{2e}{h}\int_{\varepsilon}^{\infty} f^{+}(E)\,\mathrm{d}E \tag{4.42}$$

where ε is the cut-off energy of the waveguide mode. For a multimode waveguide this becomes

$$I^{+} = \frac{2e}{h}\int_{\varepsilon}^{\infty} f^{+}(E)M(E)\,\mathrm{d}E. \tag{4.43}$$

Assuming that $M(E)$ is constant over the energy range $\mu_1 > E > \mu_2$, we can write

$$I = \frac{2e^{2}}{h}M\frac{\mu_1 - \mu_2}{e}. \tag{4.44}$$

From where

$$G_C = \frac{2e^{2}}{h}M \tag{4.45}$$

and the contact resistance will be

$$R_C = \frac{h}{2e^{2}M} \approx \frac{12.9\ \mathrm{k\Omega}}{M}.$$

The resistance of a single-mode conductor is ~ 12.9 kΩ. In the case in which scattering may occur, there will be an average probability T that an electron injected in lead 1 transmits to lead 2. Hence the conductance is equal to:

$$G = \frac{2e^{2}}{h}MT. \tag{4.46}$$

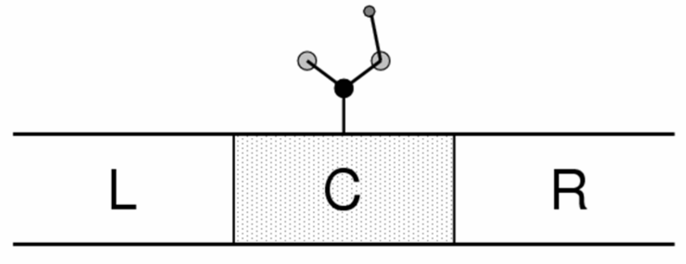

Figure 4.3: Schematic diagram of the structure across which the conductance is calculated: two semi-infinite leads, the left (L) and the right (R), are connected to the central region. In our calculations of conductance, two semi-infinite leads are pristine metallic nanotubes and the central part is the functionalized section.

This is the so-called Landauer formula for the conductance [127]. Büttiker [128] developed the multi-probe generalization of the theory:

$$I_p = \sum_q G_{pq}[V_p - V_q] \tag{4.47}$$

where p and q index the terminals, $V = \mu/e$, and $G_{pq} = (2e^2/h)T_{p\leftarrow q}$.

4.3.2 Green's function method

Practically, the transmission coefficients can be evaluated efficiently using Green's functions and transfer-matrix approach for computing transport in extended systems, which can be generalized for multi-terminal transport. This method is applicable to any Hamiltonian that can be described with a localized-orbital basis.

In the Green's function method, the system is divided into three parts [129]. These are the left (L), right (R), and central (C) regions (Figure 4.3); the left and right regions are coupled to two semi-infinite leads. The central region is the computationally-important part which may include functional sites, defects, or vacancies. Partitioning the Green's function into submatrices due to the left, right, and central regions, one can obtain the Green's function for the central region as

$$G_C^r = (\varepsilon - H_C - \Sigma_L - \Sigma_R)^{-1}. \tag{4.48}$$

The self-energy terms, Σ_L and Σ_R, describe the effect of semi-infinite leads on the central region. The functions for the coupling can be obtained as $\Gamma_{L,R} = i[\Sigma_{L,R}^r - \Sigma_{L,R}^a]$ in terms of the retarded (*r*) and advanced (*a*) self-energies. An important part of the problem is calculating the self-energy terms. The surface Green's function matching method [129-131] or computational algorithms [132] are used to calculate the Green's functions of semi-infinite leads and the self-energy terms. These terms can be obtained by using wavefunctions of ideal leads also [127]. The transmission function *T* that represents the probability of transmitting an electron from the end of the conductor to the other end, can be calculated using Green's functions of the central region and couplings to the leads:

$$T = \mathrm{Tr}(\Gamma_L G_C^r \Gamma_R G_C^a) \tag{4.49}$$

where $G_C^{r,a}$ are the retarded and advanced Green's functions of the center, and $\Gamma_{L,R}$ are functions of couplings to the leads. Knowing G_C allows us to calculate also the spectral density of states as

$$DOS(E) = -\frac{1}{\pi}\mathrm{Im}[\mathrm{Tr}G_C^r(E)] \tag{4.50}$$

4.4 Models and computational details

In our computation studies on the electronic and transport properties of covalently functionalized SWNTs, we consider two different types of covalent functional groups based on their local bonding structures with the nanotubes at the functional sites. The first type is the monovalent functional groups. These functional groups form a single covalent bond to the nanotube ("on-top", Figure 4.4(a)). Hence, the local *sp*^{2} carbon bonding structure of the nanotube will be changed to *sp*^{3} at the functional sites. In other words, the π-bonding system of the tube will be disturbed by the local *sp*^{3} rehybridization. Along with atomic fluorine (-F) and hydrogen (-H), radicals such as carboxyl group (-COOH), hydroxyl group (-OH), methyl group (-CH_3), and amino group (-NH_2) were used to systematically study this type of functionalization of SWNTs.

The second type of functional groups is divalent. As name implies, two neighboring covalent bonds are formed between the functional group and the nanotube ("bridge", Figure 4.4(b) and (c)), i.e. this type of functional group will create two adjacent functional sites on the sidewall of the tube. Additions like nitrene (>NH), carbene (>CH_2), dichlorocarbene

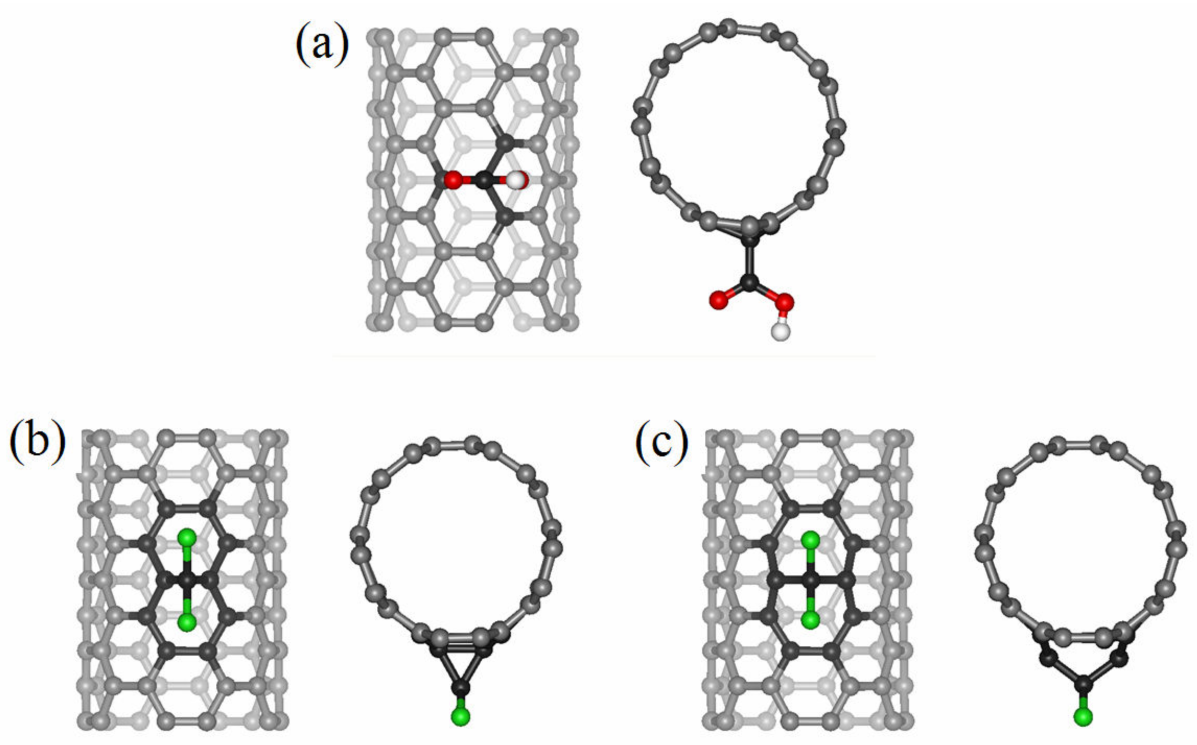

Figure 4.4: Models of covalently functionalized SWNTs; (a) monovalent functionalization, (b) divalent functionalization without the sidewall opening, and (c) divalent functionalization with sidewall opening.

(>CCl_2), oxygen (>O), and (R-)oxycarbonyl nitrene (>$NCOOC_2H_5$, R=C_2H_5) were experimentally explored [20, 62, 133-135] and simulated in our study. A previous *ab initio* study [136] based on the finite tube model indicated that there might be a carbon-carbon bond opening (sidewall opening) at the divalently functionalized site on the tube. Thus we studied both cases; without (Figure 4.4(b)) and with (Figure 4.4(c)) the sidewall opening.

In all our DFT calculations, we employed the generalized gradient approximation (GGA) level exchange-correlation energy functional (PW91) [103] for electronic structure calculations. The one-dimensional periodic boundary condition was applied along the tube axis to simulate infinitely long (rather than truncated) SWNT systems. Interactions between the functional groups and their one-dimensional periodic images are avoided in our computational supercell models, which typically include two unit cells of the zig-zag tube (supercell length c = 8.52 Å), or four unit cells of the armchair tube (c = 9.84 Å). Four to six ***k***-points [137] for sampling the one-dimensional Brillouin zone were used for the geometry optimizations at the LDA level with a convergence criterion of 10^{-4} a.u. on the gradient and displacement and 10^{-6} a.u. on the total energy and electron density.

To obtain binding energies and band structures of the functionalized nanotubes, we performed both the plane-wave based (CASTEP) [138] and numerical atomic basis (DMol3) [139] DFT calculations. In the former ultrasoft pseudopotential [114] was used with a 300 eV cutoff energy and in the latter the double numerical plus d basis set [111] was used. 30 ***k***-points were used to perform the self-consistent total energy and band structure calculations in both cases.

We followed the Landauer-Büttiker formalism [127] with the nonorthogonal localized-orbital Hamiltonian based Green's functions method [129]. A four-orbital (one 2*s* and three

$2p$) nonorthogonal tight-binding Hamiltonian was used for the carbon-carbon interactions within the SWNT, and the extended Hückel approximation [125] was employed for the tube-functional group interactions. Table 1 lists the transfer integrals of the π and σ bonds between $2p$ orbitals and the transfer between $2s$ and $2p$, and $2s$ and $2s$ orbitals of carbon atoms of SWNTs, respectively. The corresponding overlap integrals are denoted by $S_{pp\pi}$, $S_{pp\sigma}$, S_{sp}, and S_{ss}. These parameters are determined by fitting the energy dispersion relations of 2D graphite at the K and Γ points in the graphite Brillouin zone.

Table 1: Tight-binding parameters for carbon atoms of 2D graphite (eV). The definition of each parameters is taken such that the overlap integrals are positive [44].

Transfer integral	(eV)	Overlap integral	(eV)
H_{ss}	-6.769	S_{ss}	0.212
H_{sp}	-5.580	S_{sp}	0.102
$H_{pp\sigma}$	-5.037	$S_{pp\sigma}$	0.146
$H_{pp\pi}$	-3.033	$S_{pp\pi}$	0.129

The Extended Hückel parameters for H, N, O, F, and Cl atoms used in this work to describe the tube-(functional group) interactions are listed in Table 2. The atomic Slater orbital coefficients for s orbital (ζ_s), p orbital (ζ_p), and atomic orbital energies (H_{ss} and H_{pp}) are taken from Ref. [140]. n is the principal quantum number. The subroutines for calculating overlap integrals of Slater type orbitals are taken from Ref. [141] and the tight-binding Hamiltonian is constructed via Slater-Koster table [115].

This type of tight-binding Hamiltonian keeps our computational time and memory requirement small, allows calculations of relatively large systems (>1000 atoms), and yet ensures adequate quality of results to capture the physics near the Fermi energy of the systems we studied. As a result, certain phenomena involving large number of atoms, such as the delocalization of the functional-group-induced impurity states in functionalized metallic tubes (Chapter 5) or the quantum interference effects manifested in two-monovalent-functional-group configurations (Chapter 6) could be investigated.

Table 2: Extended Hückel parameters for H, N, O, F, Cl atoms used in this work. ζ_s and ζ_p are Slater orbital coefficients for *s* and *p* orbitals respectively; H_{ss} and H_{pp} are atomic orbital energies; and *n* is the principal quantum numbers [140].

Element	n	ζ_s	H_{ss} (eV)	ζ_p	H_{pp} (eV)
H	1	1.300	-13.6		
N	2	1.950	-26.0	1.950	-13.4
O	2	2.275	-32.3	2.275	-14.8
F	2	2.425	-40.0	2.425	-18.1
Cl	2	2.183	-26.3	1.733	-14.2

As a test of our tight-binding Hamiltonian, I present the band structure results obtained for metallic (8,8) tubes monovalently functionalized with several functional groups (-H, -OH, and -F). Figure 4.5 shows calculated band structures from (a) *ab initio* DFT calculations at the GGA level, and (b) our tight-binding Hamiltonian based on the extended Hückel approximations. In both cases, the one dimensional periodic boundary condition is applied in the direction of the tube axis and one functional group is included in every three unit cells (c = 8.52 Å) of (8,8) tubes. It is clear that the electronic structure near the Fermi level, such as the disturbance of the metallic band crossing by the functional-group-induced impurity state (a detailed discussion is in chapter 5), is well reproduced by our tight-binding Hamiltonian. This justifies the use of the tight-binding Hamiltonian in our qualitative analyses of the impurity state wavefunctions and transport properties of functionalized nanotubes.

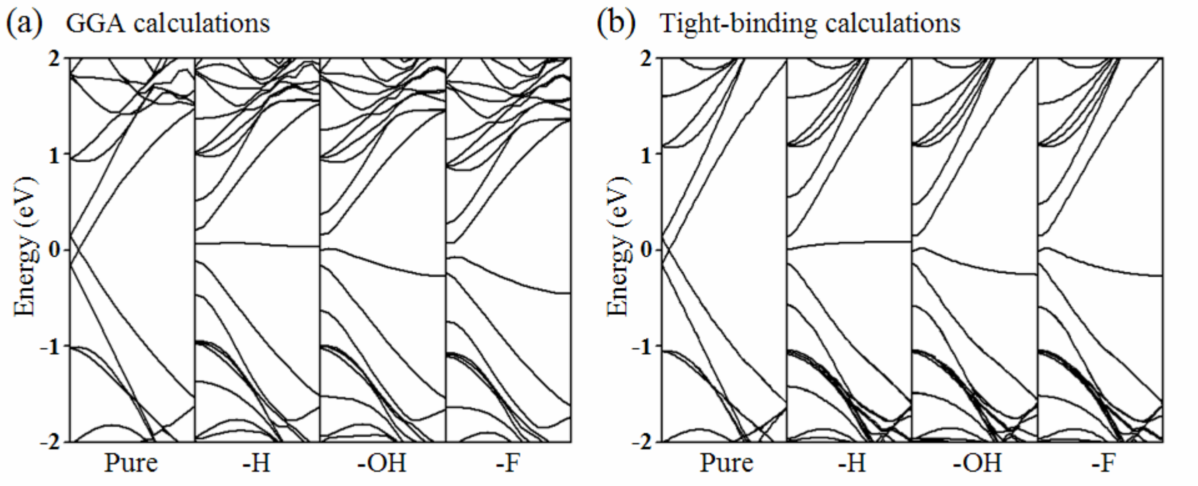

Figure 4.5: Band structures of (8,8) tubes functionalized with H, OH, and F from (a) *ab initio* DFT calculations at GGA level and (b) tight-binding calculations. The electronic structure near the Fermi level, such as the disturbance of metallic band crossing by the functional group induced impurity state, is well reproduced by our tight-binding Hamiltonian

Chapter 5

Electronic Properties of Functionalized SWNTs

Experiments on nanotube functionalization start from the fluorination of SWNTs [17] and the substitution reaction of fluorinated SWNTs in solutions [80, 142, 143]. Direct functionalization to the sidewall of SWNTs by various chemical groups such as atomic hydrogen [144-147], carbine [20, 62, 133], nitrene [134, 135], alkyl group [148], *N*-alkylidene amino group [81], and aniline [149] has also been reported. In general, changes in physical properties of carbon nanotubes upon functionalization are found. For instance, the band-to-band transition feature of π-electrons in the UV-vis spectra of pristine SWNTs is disrupted by covalent functionalization [81, 143, 148-150]. The resistance of functionalized SWNTs dramatically changes with respect to the pristine samples [17, 143, 147, 151].

Theoretically, little is known about the effect of covalent sidewall functionalization on electronic structures of carbon nanotubes. From previous works, it was shown that the electronic and transport properties of SWNTs can be significantly modified upon adsorption of selective gas molecules (NO_2, O_2) [9, 152-155] or noncovalent functionalization of aromatic organic molecules [19, 156]. The effect of substitutionally doped impurities on the conductance of SWNTs was studied by Choi et al. [157] and Guo's group [158]. Andriotis et al. studied the conductance and HOMO-LUMO gap for nanotubes with atomic hydrogen

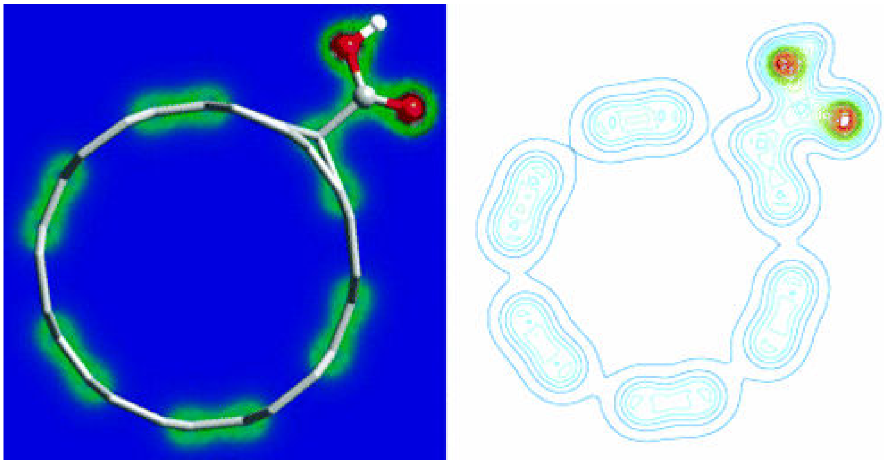

Figure 5.1: Atomic structure (left) of COOH-attached (6,6) SWNT and contour plot of electron density (right) on the slice passing through the COOH group. Red, yellow, green, and blue colors on the contour plot indicate electron density from higher density to lower density. The structural distortion on the nanotube is found to be confined to the nearest neighbors of the bonding site.

adsorption [159]. In this chapter, I present our *ab initio* results on the electronic properties of covalent sidewall functionalized SWNTs.

5.1 Monovalently functionalized SWNTs

5.1.1 Local geometric structure at the functional site

As shown in Figure 5.1, the COOH group induces a local distortion along the radial direction on the sidewall upon functionalization, which can be understood by the local sp^3 rehybridization of carbon-carbon bonding. The overlap of valence election density, shown in Figure 5.1 as a contour plot, indicates the formation of a covalent bond between the functional group and the nanotube. From the relaxed structures of our computational models, we found that the calculated bond length between the C atom on the nanotubes at the functional site and its nearest neighboring C atoms is about 1.52 Å (d (Å) in Table 3) across all functional groups (-F, -H, -COOH, -OH, -NH_2, and -CH_3), which is close to the C-C bond length in the sp^3-hybridized diamond phase and significantly larger than the C-C bonding length of 1.42 Å in the perfect nanotube with sp^2-hybridization. This again confirms the dominance of the covalent sp^3 bonding at the functional site. The same behaviors are found for all the SWNTs (zig-zag: (8,0), (9,0), (10,0), (11,0), (12,0) and armchair: (5,5), (6,6), (7,7), (8,8) nanotubes) and can be considered as the common features of the covalent sidewall functionalization of carbon nanotubes.

Table 3: The binding energy (E_b) and bond lengths for various functional groups on a (5,5) tube. D is the molecule-tube covalent bond length; d is the C-C bond length between the sp^3 C atom on the tube and its nearest neighbor C atoms.

Additions	E_b (eV)	D (Å)	d (Å)
-F	3.192	1.423	1.503
-OH	2.297	1.428	1.514
-H	2.854	1.113	1.519
$-NH_2$	1.937	1.460	1.522
$-CH_3$	1.861	1.533	1.525
-COOH	1.721	1.534	1.519

5.1.2 Tube-(functional group) interactions

In this work, the bonding energy E_b of the functional group is defined by the total energy gained by the functionalization at the equilibrium geometry (see Figure 5.2): $E_b = E_{tot}$ (tube) + E_{tot} (group) – E_{tot} (tube + group). Table 3 lists the binding energies and the characteristic bond lengths for all functional groups examined for the (5,5) tube. We can see differences among different functional groups in their strength of interaction with the tube (E_b in Table 3) and their covalent bond lengths (D (Å) in Table 3).

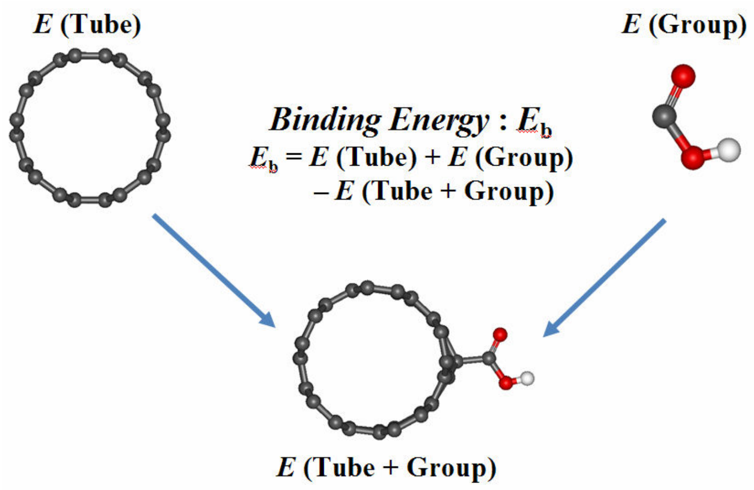

Figure 5.2: Schematic diagram of the binding energy calculation. Calculate the total energy of the completely separated system of a SWNT and a functional group. Then bring them together, relax the structure, and get the total energy of the hybrid system. The energetic difference is the binding energy E_b in our calculations.

In Figure 5.3 we have a graph of binding energy E_b versus curvature $1/R$ of nanotubes with three different monovalent groups (-F, -OH, and -COOH). This graph is a summary of our binding energy study. For each functional group, there are two different energetic trends based on the types of nanotubes (metallic and semiconducting). The differences in binding energy among different groups are insensitive to the size and the type of tubes. For example, between -COOH and -OH, there is about 0.57 eV difference in the binding energy across all tubes examined. This constant difference reflects the localized feature of the covalent interactions between sp^3 rehybridized carbon atoms on the nanotube and the functional group and such interaction is molecule specific.

On top of these functional-group-specific features, some intrinsic nanotube properties are revealed as well. Our systematic study (Figure 5.3) shows the strong dependence of binding energy on the size (curvature) and the electronic structure (metallic or

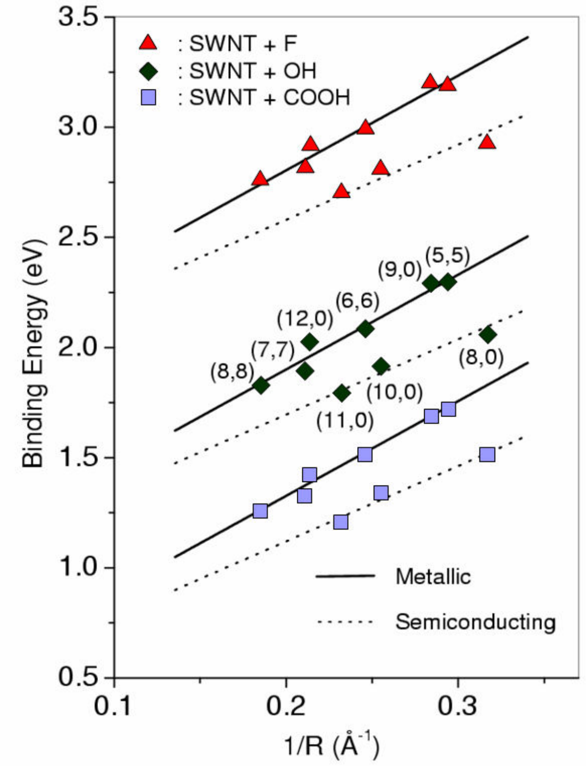

Figure 5.3: Binding energies of -F, -OH, and -COOH additions to SWNTs as functions of the curvature 1/*R*. The differences among different functional groups are insensitive to the size and the chirality. The binding to metallic tubes is systematically stronger than to semiconducting ones. The binding energy increases linearly with the curvature of tubes.

semiconducting) of the tube. For all cases investigated the strength of binding is inversely proportional to the tube radius. It was expected that smaller tubes would have a higher tendency for sp^3 hybridization due to the curvature effect [69]. As we increase the curvature of the tubes, the strain on the sp^2 carbon-carbon bonding structure is increased. This build-up of strain makes the tube more reactive to covalent functionalization. Simple linear fits (Figure 5.3) lead to a slope of 4.3 eV·Å for metallic tubes and 3.2 eV·Å for semiconducting ones. These slopes are found to be insensitive to the type of functional groups, revealing that the curvature dependence is truly controlled by the local sp^3 hybridization.

Furthermore, two different energetic trends in each functional group (Figure 5.3) are showing that metallic tubes are more reactive to the functionalization at a given size of tubes.

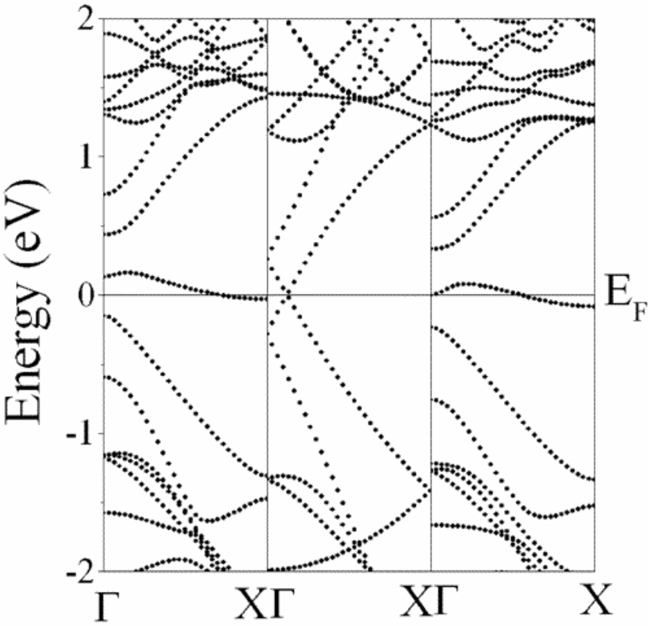

Figure 5.4: Band structure of pristine (middle), COOH-attached (left), and NH_2-attached (right) armchair (6,6) SWNT from GGA calculations. One functional group is included per three unit cells of the tube. The sp^3 defect-induced impurity state at the Fermi level is clearly seen in both cases.

Because of the availability of delocalized electronic states near the Fermi level, which enables a stronger hybridization between functional groups and nanotubes, the binding of groups to metallic tubes is stronger. This is supported by recent experiments [26, 62, 135] and would provide a novel way to manipulate CNTs according to their electronic structure.

5.1.3 Functional-group-induced impurity states

To further study differences in their electronic structures, we examined in detail band structures of both metallic and semiconducting SWNTs functionalized with different groups (-F, -H, -COOH, -OH, $-NH_2$, and $-CH_3$) on the basis of their optimized structures. As representatives, the band structures of the armchair metallic (6,6) tube functionalized by COOH and NH_2 groups are shown in Figure 5.4. For all the monovalent functional groups

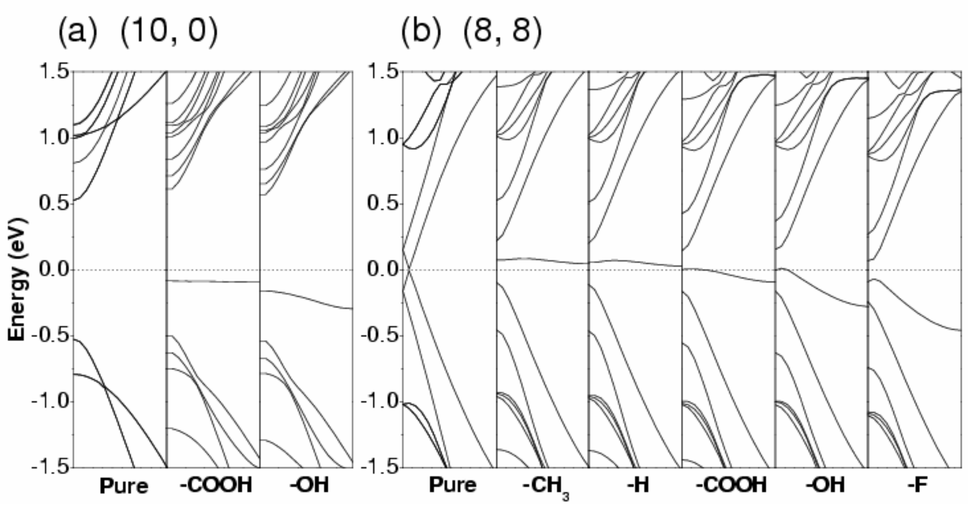

Figure 5.5: Band structures near the Fermi level (From Γ to Z) of functionalized SWNTs with various monovalent-functional groups from GGA calculations. Dotted lines indicate the Fermi level of pristine nanotubes (set as zero in all plots). (a) Semiconducting (10,0) tubes and (b) metallic (8,8) tubes.

considered, an individual functionalization-induced sp^3 defect on the tube sidewall induces a half-occupied impurity state around the Fermi level. Including more functional groups in the computational supercell will lead to multiple impurity states around the Fermi level. The appearance of a half-filled level in the gap was also found in a recent *ab initio* study of silicon-doped SWNTs with chemical binding of atoms (F, Cl, H) and molecules (CH_3, SiH_3) at silicon substitutional sites [160].

Intuitively, one can consider this impurity state as a combined state of the nanotube bands and the molecular states of the functional group near the Fermi level. In the case of the semiconducting tubes, we found that the band structure near the Fermi level is almost unaffected by the functionalization except for the presence of the impurity state in the gap and the lifting of band degeneracy due to the breaking of nanotube mirror symmetry [161, 162] (Figure 5.5(a)). This indicates that the impurity state mainly comes from the molecular states of the functional group. Thus one can expect the state to be localized around the

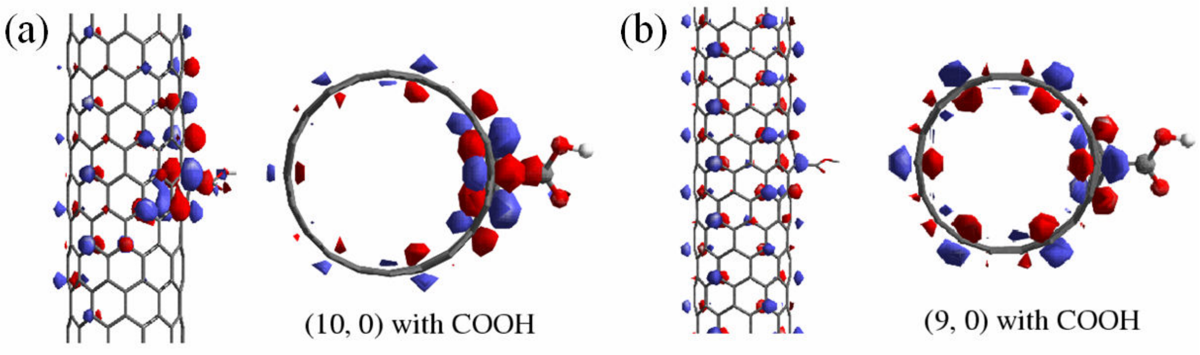

Figure 5.6: Iso-surfaces of the impurity state wavefunction from GGA calculations for COOH-attached (a) semiconducting (10,0) tube and (b) metallic (9,0) tube. Two different colors represent +/- polarity of the wavefunction. The impurity state is mostly localized near the functional site for the semiconducting tube and delocalized for the metallic tube.

functional site. In contrast, for metallic tubes the electronic structure near the Fermi level undergoes significant changes and the state has a large spectrum weight contributed from the nanotube. Therefore, the state is expected to be more delocalized.

Shown in Figure 5.6 are the wavefunctions of the impurity states from GGA calculations for functionalized semiconducting (10,0) and metallic (9,0) nanotubes with COOH groups. Unlike the localized impurity state wavefunction for the semiconducting nanotubes, the wavefunction for the metallic tube appears to be delocalized. This delocalization might explain the reason why metallic tubes are more reactive to the covalent functionalization. Due to the limit on the supercell size in our *ab initio* calculations, it is not possible to extract the localization length of the impurity state. One may also question whether the appearance of the delocalization in the metallic case is due to the finite supercell size in our model computations. To further confirm our conclusion we performed large-scale calculations using a tight-binding Hamiltonian in the extended Hückel approximation [125]. The tight-binding Hamiltonian has been shown to reproduce well the band structures of nanotubes near the Fermi level (see Figure 4.5) [163].

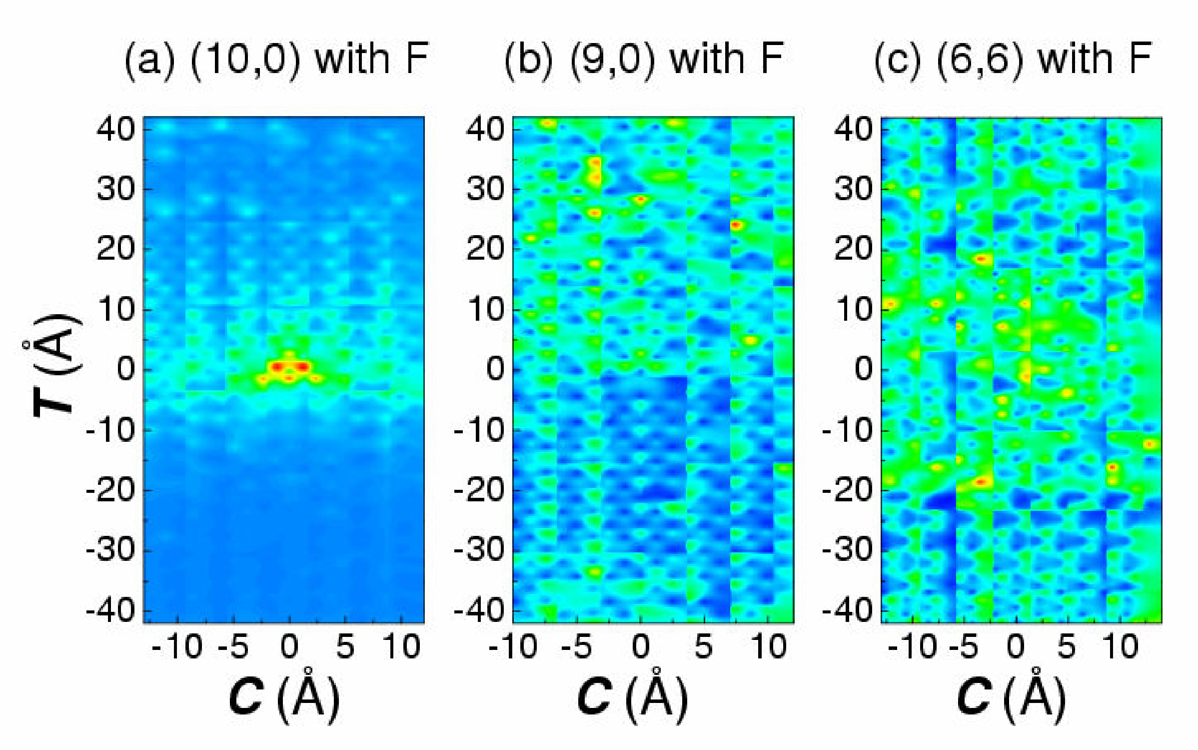

Figure 5.7: Impurity state wavefunction calculated in tight-binding approximation for large supercell sizes. Wavefunctions are projected onto the unfolded nanotube coordinates for easy visualization: the vertical axis (*T*) is the tube axis and the horizontal axis (*C*) is the chiral vector axis (folding direction of the nanotube). The F addition is located at the origin in all plots. The impurity state wavefunction is clearly seen localized in the (10,0) semiconducting tube, while it is extended for both (9,0) and (6,6) metallic tubes.

Figure 5.7 shows wavefunctions of impurity states for large supercells (supercell length a ~ 85 Å for zig-zag tubes; a ~ 98 Å for armchair tubes). Now it can be clearly seen that the impurity state is localized in the semiconducting zig-zag tube (Figure 5.7(a)), whereas for both zig-zag (Figure 5.7(b)) and armchair (Figure 5.7(c)) metallic tubes the states are delocalized over the large supercells. Quantitative analysis reveals that the length scale associated with the localized impurity state is around 15 Å, and insensitive to the choice of the functional group and the nanotube size. A similar length scale was found in the case of chemical substitution dopings [164] and in a recent experimental study of topological defects [165].

5.2 Divalently functionalized SWNTs

5.2.1 Geometric structures

Divalent functional groups (>$NCOOC_2H_5$, >CCl_2) form bridge-like covalent bonds with two carbon atoms in the sidewall of nanotubes. They create two adjacent covalent functional sites. This vicinity of the functional sites causes a strong interaction between two sites. Therefore, the local electronic structure is expected to be somewhat different from that with the monovalent functional group. Figure 5.8 shows the local structure of the (6,6) SWNT with an attached $NCOOC_2H_5$ group. The computed characteristic bond lengths, d_1 and d_2 (as defined in Figure 5.8) for the CCl_2 and $NCOOC_2H_5$ adducts as well as the other SWNTs studied (see Figure 5.9(a)-(c)) are listed in Table 4. All the chemical modifications result in a d_2 separation of over 2 Å, hence our computations with periodic boundary conditions (PBC)

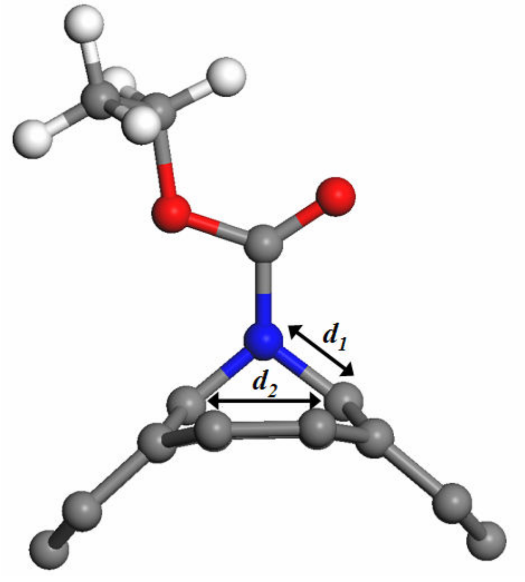

Figure 5.8: Local structure of a $NCOOC_2H_5$ group attached to a (6,6) SWNT (carbon: gray, hydrogen: white, nitrogen: blue, oxygen: red). Only a small fragment is shown for clarity. Note the opening of the nanotube sidewall. d_1 is the bond length between the N (or C if the functional group is CCl_2) atom of the functional group and C atoms on tube sidewall. d_2 is the distance between the two C atoms to which functional groups are attached.

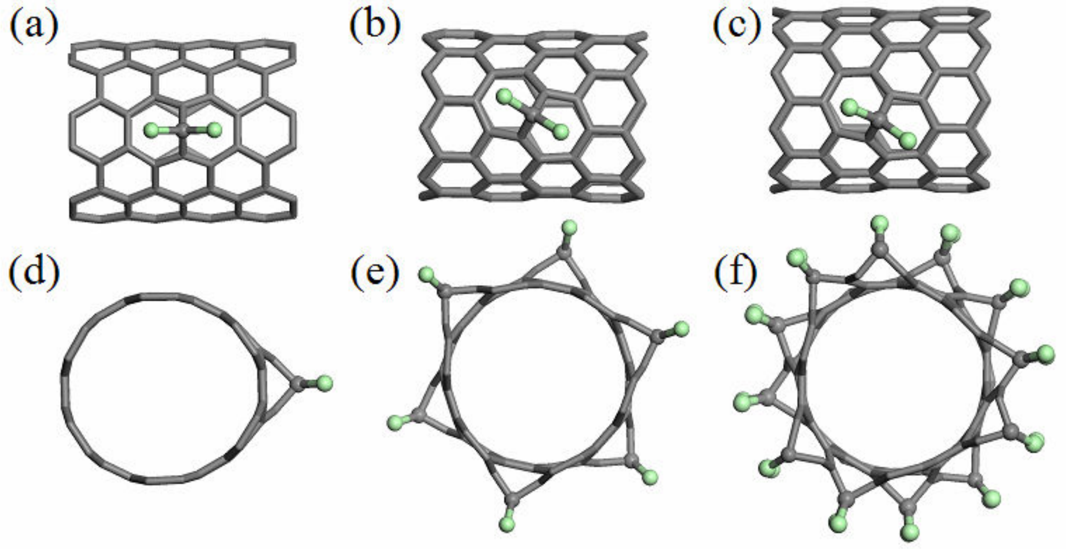

Figure 5.9: Side view of optimized structures of CCl_2 modified SWNTs (carbon: gray, chlorine: light green): (a) (6,6) tube; (b) (9,0) tube; (c) (10,0) tube. Top view of optimized structures of CCl_2 modified (6,6) SWNTs with different Cl:C ratios: (d) Cl:C = 2%; (e) Cl:C = 12.5%; (f) Cl:C = 25%.

support earlier theoretical predictions based on finite tube models [136]: both CCl_2 and $NCOOC_2H_5$ additions open the SWNT sidewalls.

For each type of SWNT, there are two sets of C-C bonds on tube sidewalls that can undergo functionalization. We considered all those possibilities for CCl_2 and $NCOOC_2H_5$ additions and found that in armchair the functional groups tubes prefer to be attached to the C-C bond perpendicular to the tube axis, whereas zigzag SWNTs favor functionalization with the C-C bond slanted to the tube axis. Theses conclusions agree with previous finite tube calculations [136]. The folding direction of SWNTs is the direction where the strain on the C-C bonding is the greatest and along the tube axis the strain is least, divalent covalent bonds along the tube axis are energetically unfavored.

Table 4: The characteristic bond lengths, d_1 and d_2, of the local geometry and binding energies E_b (kcal mol^{-1}) for the functionalized SWNTs. d_1 is the bond length between the C or N atoms of the functional group and the C atom on the sidewall; d_2 is the bond length between the two C atoms to which the functional groups are attached.

CCl_2	(6,6)	(9,0)	(10,0)
d_1 (Å)	1.51	1.50	1.49
d_2 (Å)	2.18	2.16	2.19
E_b (eV)	1.436	1.068	0.751

$NCOOC_2H_5$	(6,6)	(9,0)	(10,0)
d_1 (Å)	1.41	1.40	1.40
d_2 (Å)	2.20	2.20	2.19
E_b (eV)	2.813	2.345	2.204

The functionalization of carbon nanotubes at higher functional-group concentration has been investigated by including a greater number of CCl_2 groups in the computational supercell (see Figure 5.9(d)-(f)). As in the experimental article [133], the Cl:C modification ratio is based on the number of Cl atoms on CCl_2 groups and the number of C atoms on the tube sidewall. Our DFT geometry optimizations show that sidewall opening persists even at higher concentrations (Cl:C ratios up to 25%).

5.2.2 Tube-(functional group) interactions

The tube-(functional group) interactions can be assessed by computing the binding energies of addition of CCl_2 and $NCOOC_2H_5$ to the nanotubes. In agreement with recent experimental observations [26, 83, 135, 166], these binding energies are larger when they involve metallic (6,6) or (9,0) rather than semiconducting (10,0) tubes (Table 4). The functionalization of SWNTs with diazonium reagents shows high selectivity on the tube

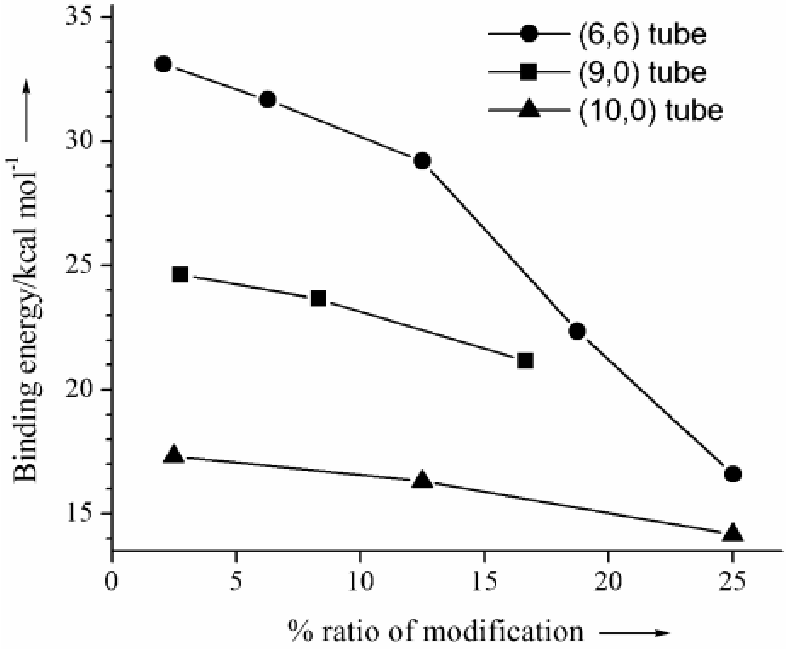

Figure 5.10: Average binding energies of CCl_2 additions to SWNTs at different ratio of modification, C:Cl.

electronic structures; metallic nanotubes are preferred [26, 83]. The Raman spectra of (R)-oxycarbonyl nitrene-functionalized SWNTs also show preferential interaction with the metallic tubes [135]. The higher reactivity of the metallic nanotubes can be related not only to higher reaction exothermicity, but also to the available electron density near the Fermi level; this supports the stabilization of transition states by charge transfer during bond formation [26, 83, 167].

Figure 5.10 plots the binding energies of CCl_2 to different SWNTs as a function of the modification ratio Cl:C. In general, the binding energy between the group and nanotubes decreases with increasing modification ratio for all SWNTs. However, the binding energies for both (6,6) and (10,0) tubes are still significant (over 14 kcal mol^{-1}) up to a 25% modification ratio, suggesting the possibility of further functionalization. Note that recent experiments by Haddon and co-workers achieved CCl_2 functionalization up to 23% [133].

5.2.3 Electronic band structures

The tube-(functional group) interaction in the covalent sidewall functionalization has direct consequences on the electronic properties of carbon nanotubes. As previously pointed out, monovalent functional groups (-F, -H, -COOH, -OH, -NH_2, -CH_3) disrupt the geometries and electronic structures of the perfect nanotube dramatically by introducing local sp^3 hybridization defects, which induce a half-filled impurity state near the Fermi level. What occurs when carbenes and nitrenes are added to nanotubes? Such divalent reactive intermediates bind to two neighboring carbon atoms on the tube sidewall and alter their character from sp^2 to sp^3 hybridization. Moreover, strained three membered rings evidently do not exist, as the tube sidewall where they are attached can open, such structural uniqueness no doubt will lead to quite different electronic properties.

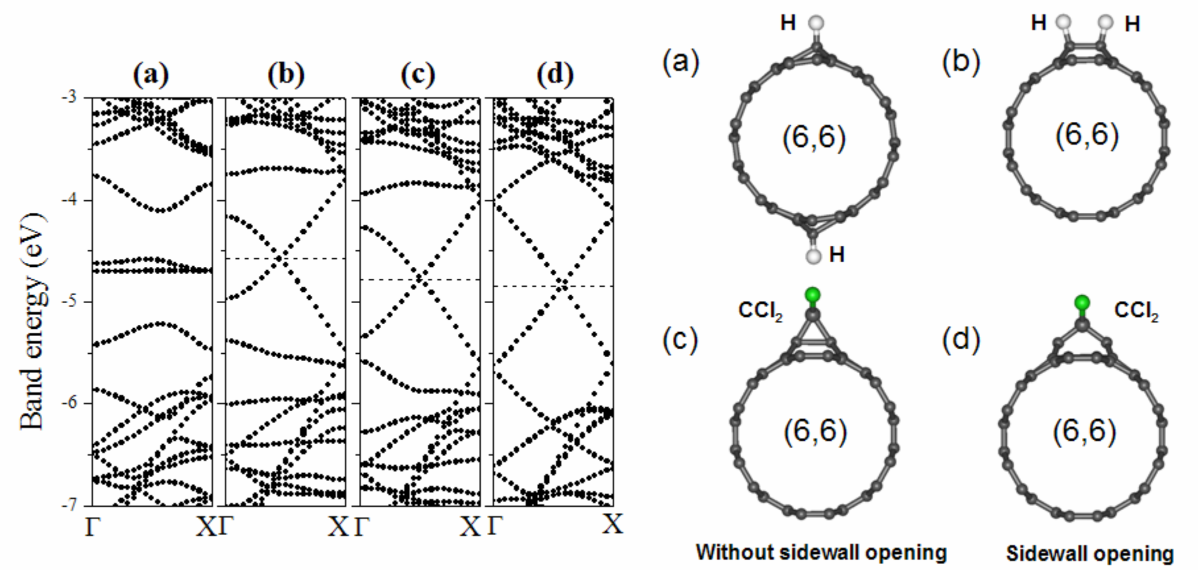

Figure 5.11: Band structures and computational models of functionalized (6,6) SWNTs: (a) with two separated hydrogen atoms attached as far as possible in one supercell; (b) with two hydrogen atoms attached in the neighboring sites; (c) with attached CCl_2 group but without sidewall opening; (d) with attached CCl_2 group with sidewall opening. Dashed lines denote the Fermi level. The line in (a) is not seen because of overlap with the impurity bands.

To understand these complexities, we considered computationally different models of nanotube functionalization at low concentration (two hydrogen atoms or one CCl_2 group per (6,6) tube supercell with 96 carbon atoms): (a) two hydrogens are attached to nanotubes at independent (remote) positions; (b) two hydrogens are attached to two vicinal carbons on the tube sidewall; (c) a CCl_2 group is attached to the nanotube as a three-membered ring without allowing the sidewall to open; (d) a CCl_2 is attached to the nanotube with sidewall opening. Model (a) represents the typical monovalent functionalization studied earlier. Model (b) is like the hydrogenation of a double bond and imitates, for example, the formation of a five-membered ring on the tube sidewall [15, 166]. Model (c) is similar, but a strained three membered ring is involved, which will open to give model (d) upon optimization. Comparisons between models (c) and (d) reveal differences in the electronic structures of models (a)-(d) for (6,6) SWNTs are presented in Figure 5.11.

The two local sp^3 defects resulting from the addition of two separated hydrogen atoms result in two impurity bands close to the Fermi level of the nanotube and significantly disturb the metallic band structure of the parent nanotubes (Figure 5.11(a)). However, if the two hydrogen atoms are attached to neighboring carbons on the nanotube, the two resulting local defects interact strongly. As a consequence, the two impurity states seem to be rehybridized into *bonding* and *anti-bonding states*. Those two states are shifted away from the Fermi level (Figure 5.11(b)), and the band crossing at the Fermi level of the parent armchair tube is recovered. In other words, the metallic behavior of the parent nanotube will be retained by functionalizations that form two single bonds at vicinal sidewall carbons, despite the introduction of two local sp^3 defects into the conjugated π-electron system. This conclusion is rather general, and is applicable to all functionalizations, for example, those with closed three- or five-membered ring subunits on the tube sidewalls. Thus there are interesting similarities in the band structures of SWNTs functionalized by two hydrogen atoms on adjacent carbons (Figure 5.11(b)) and by a CCl_2 group forced to form a closed three-membered ring on tube sidewall (Figure 5.11(c)). A recent experiment on pyrrolidine ring functionalized SWNTs (at low modification ratio of one pyrrolidine ring to about 95 carbon atoms on the nanotube) showed that the metallic character of the pristine nanotube was retained and the overall electronic structures was not affected strongly [166].

I would like to stress that our computational model with two vicinal monovalent functional groups (Figure 5.11(a)) is not the energetically favorable configuration in normal monovalent functionalization processes due to the strong repulsion between two functional sites. In addition, the full DFT geometry optimizations transform (c)-type to (d)-type structures (Figure 5.11); the latter corresponds to CCl_2 adducts with opened sidewalls. Since the sidewall C-C bonds are broken, the carbon atoms attached to the functional groups retain their sp^2 hybridization. Hence, the π-electron delocalization of the parent SWNTs is only perturbed modestly. Therefore, the band structures of the pristine SWNTs are only slightly disturbed at low concentrations of carbene- and nitrene-like groups. This theoretical conclusion is consistent with experimental findings on nanotube functionalization at low modification ratios: SWNTs functionalized by (R-)oxycarbonyl nitrene at a low N:C ratio of about 1-2% only showed minor changes in the optical absorption [135].

5.3 Summary of electronic properties

In conclusion, we have performed a systematic study of electronic properties of covalent sidewall functionalized SWNTs. We found that the existence of available electrons near the

Fermi level allows metallic tubes to make a stronger bond to the functional group than semiconducting ones, and smaller tubes are more reactive due to the intrinsic cylindrical curvature effect. Monovalent functional groups induce impurity states near the Fermi level and the impurity states significantly disturb the electronic structure of the parent SWNTs. The impurity states are found to be tightly localized around the functional site for semiconducting SWNTs and more delocalized for metallic ones. Divalent-type covalent functionalization creates two adjacent functional sites. Due to the strong interaction between them, they rehybridize into bonding and anti-bonding states and those states are located relatively far away from the Fermi level. Hence, the electronic structure of the parent SWNTs near the Fermi level is not substantially modified by divalent-type functional groups.

Chapter 6

Transport Properties of Functionalized SWNTs

Sidewall functionalizations disrupt the π-bonding system and break the translational symmetry of SWNTs by introducing saturated sp^3 carbon atoms. As a result, the electronic and transport properties of SWNTs are significantly altered. There have been many experimental and theoretical studies of the transport properties of carbon nanotubes. The ballistic transport has been reported in defect-free multi-walled [168-170] and single-walled [171-173] nanotubes. Individual SWNTs have been recognized as coherent electron waveguides and electron resonators [60, 174-176]. These behaviors, however, will be significantly changed when there are scattering centers such as covalent additions and local structural defects [157, 177, 178].

In this chapter, our numerical studies of the conducting properties of covalently functionalized metallic SWNTs will be presented. Systematic dependence on the functional-group concentration is investigated for both monovalent and divalent sidewall additions. The geometrical structure for the conductance study is composed of two leads (left (L) and right (R), both are pristine SWNTs) separated by the central section where the covalent functionalization groups are added (Figure 6.1(a)). Only metallic armchair SWNTs are studied. Figure 6.1(b) shows an example of the computational models with a single

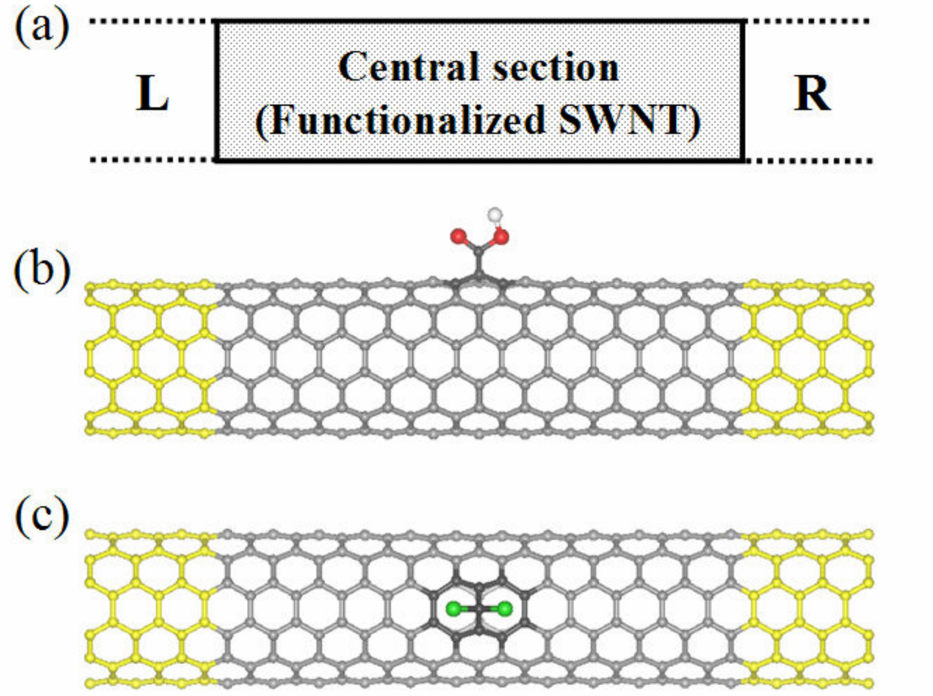

Figure 6.1: Schematic representations of (a) the structure across which the conductance is calculated: two semi-infinite leads (left (L) and right (R), both are pristine tubes) are connected to the functionalized region. Computational models with (b) a single monovalent functional group (-COOH); (c) a divalent functional group (>CCl_2) for the conductance calculation.

functional group; Figure 6.1(c) is the case with a divalent functional group. The Landauer-Büttiker formalism [127] was used to calculate the conductance based on Green's functions method [129, 179-181] with the nonorthogonal tight-binding Hamiltonian [182, 183].

6.1 Monovalently functionalized SWNTs

Our studies of electronic properties of monovalently functionalized SWNTs have shown that monovalent functional groups universally induce impurity states. The states strongly disturb the local electronic structure of the parent nanotubes near the Fermi level. Thus, one can easily imagine that those impurity states will be centers of scattering for conducting electrons of nanotubes.

6.1.1 Electron scattering at impurity states

Figure 6.2 shows the calculated conductance and the density of states (LDOS) of the pristine metallic (6,6) SWNT (Figure 6.2(a)) and the functionalized (6,6) with a single COOH group attached (Figure 6.2(b)). It is clear that the covalently functionalized site acts as a strong scattering center for the conducting carriers. The ballistic conductance of nanotube is disturbed and there is a significant dip near the Fermi level. This demonstrates that the local sp^3 rehybridization of the carbon atom at the functional site and the induced impurity state strongly disrupt the conducting π and π* bands near the Fermi level.

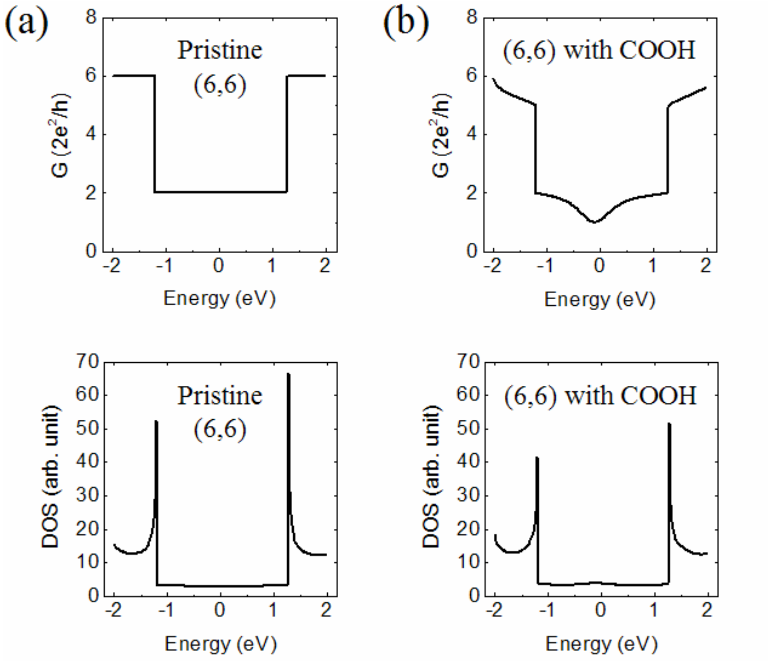

Figure 6.2: The calculated conductance and density of state (DOS) of center portion in Figure 6.1 of (a) pristine metallic (6,6) tube and (b) functionalized (6,6) tube with a single COOH group. Ballistic conductance of the tube (a) is disturbed by functionalization and a significant dip appears in the conductance plot of (b).

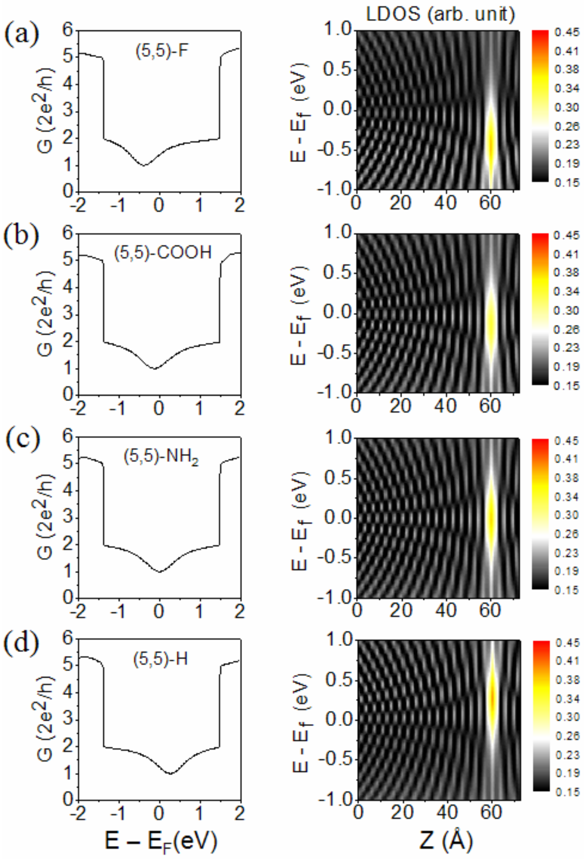

Figure 6.3: The calculated conductance and local density of states (LDOS) near the Fermi level as a function of energy for monovalently functionalized (5,5) tube with (a) -F, (b) -COOH, (c) -NH_2, and (d) -H. Each group exhibits a conductance minimum at a specific energy which correlates well with the energetic position of the functional-group-induced impurity state. Z is the coordinate along the tube axis and groups are attached at Z = 60.27 Å in all LDOS plots.

Our systematic study with different types of functional groups (-F, -H, -COOH, -OH, -NH_2, and -CH_2) shows that each group exhibits a different energetic position for the scattering as can be seen in the plots of conductance and local density of states (LDOS) (Figure 6.3). The energetic position of scattering is where the conductance reaches its minimum, and this turns out to be well correlated with the position of the functional-group-induced impurity state relative to the pure nanotube Fermi energy in the band structure calculation of the previous study. Thus, we can attribute this scattering effect to the impurity state induced by the functionalization near the Fermi energy.

6.1.2 Quantum interference effects

With the ballistic electron conduction and a long electron phase relaxation length (which is about a few hundred nano-meters at low temperature and much longer than the length of our computational models) of nanotubes, we will be able to observe some quantum interference effects if we have electron scattering centers near the Fermi level. Figure 6.4(a) shows the basic computational model used in our conductance calculations to explore those electron wave interference effects. Two identical monovalent functional groups are attached on a (5,5) metallic tube and the electron conducting behavior is studied as we gradually increase the separation between them (*L*).

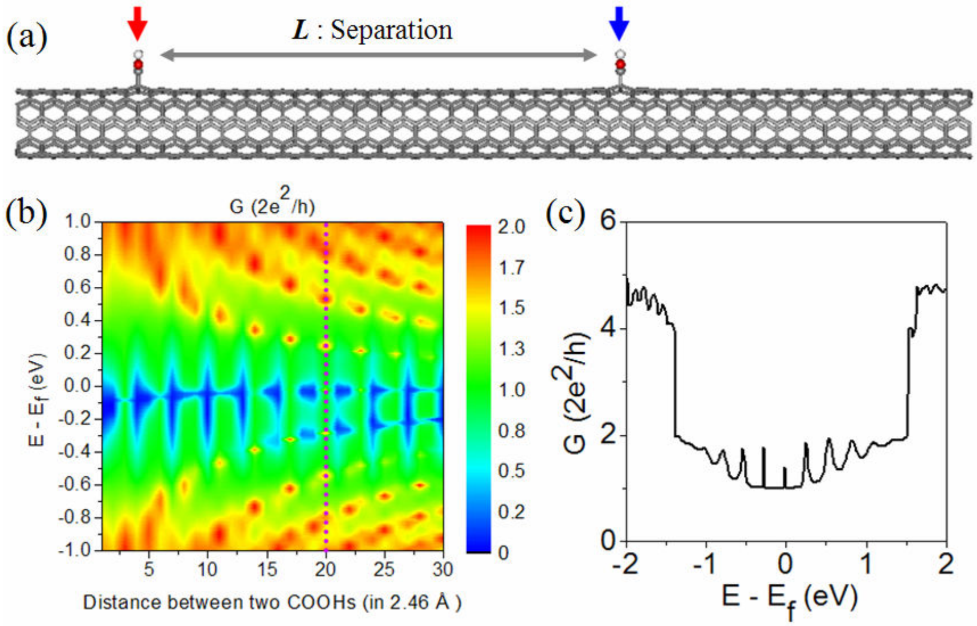

Figure 6.4: The computational models with two identical monovalent functional groups (a); the calculated conductance contour plot of (5,5) tubes functionalized with two COOH groups as a function of separation between groups and energy relative to the Fermi level of the pristine nanotube (b); an example of the conductance calculation evaluated when the separation between two COOH groupss is 20 unit cells apart ($L = 20 \times 2.46 = 49.2$ Å) (c).

Figure 6.4(b) is a contour plot summarizing the calculated conductance of monovalently functionalized (5,5) SWNTs with -COOH functional groups as a function of energy ($E - E_F$ (eV)) and separation (L in the unit of 2.46 Å, which is the length of a armchair unit cell along the tube axis). Figure 6.4(C) is an example of the conductance calculation evaluated when the separation between two COOH groups is 20 unit cells ($L = 20 \times 2.46 = 49.2$ Å) as indicated by a dotted vertical line in Figure 6.4(b).

The first feature of immediate interest in the conductance contour plot (Figure 6.4(b)) is the periodic appearance of “blue areas” along the separation axis. Those represent

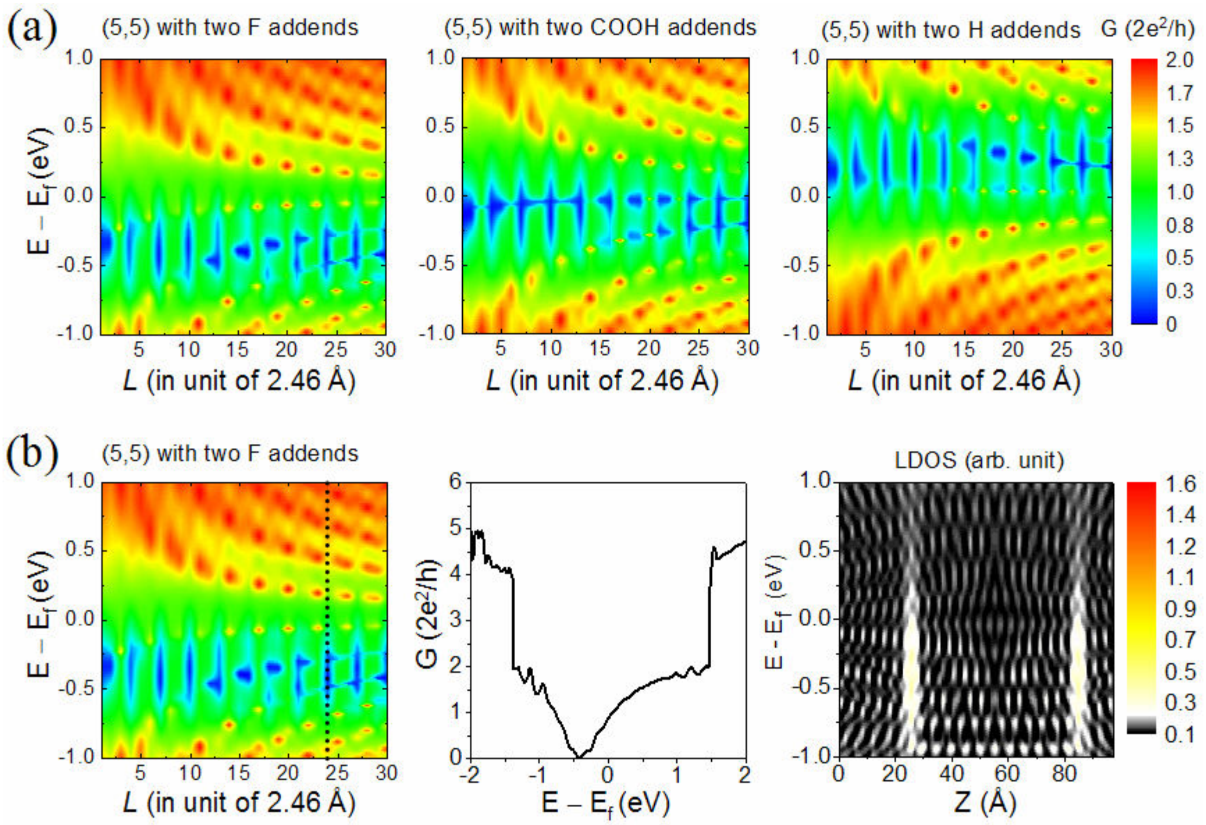

Figure 6.5: Contour plots of calculated conductance (a) with two monovalent functional groups of F, COOH, and H respectively (from left to right) showing functional-group-specific energetic positions for conduction dips; (b) with two F groups. Conductance and LDOS plots are evaluated when the separation $L = 24$ (59.04 Å), indicated as a vertical dotted line in the first plot. They show the strong resonant scattering effect at those two impurity sites (two Fs are attached at $Z = 25.83$ Å and $Z = 84.87$ Å respectively).

conductance dips where the conductance is reduced to zero. Using different types of monovalent groups (Figure 6.5(a)), we found that the energetic position of those dips corresponds to the functional-group-induced impurity state energy levels (~ -0.40 eV for F and -0.14 eV for COOH) for each type of functional groups. Moreover, the period of conductance dips along the separation axis is found to be well matched with the Fermi wavelength of armchair nanotubes; $\lambda_F = 3a_0 = 0.738\,\text{nm}$. These indicate that the conductance fluctuation is mainly due to the resonant reflections of conducting carriers between two impurity sites. The LDOS contour plot in Figure 6.5(b) shows the strong

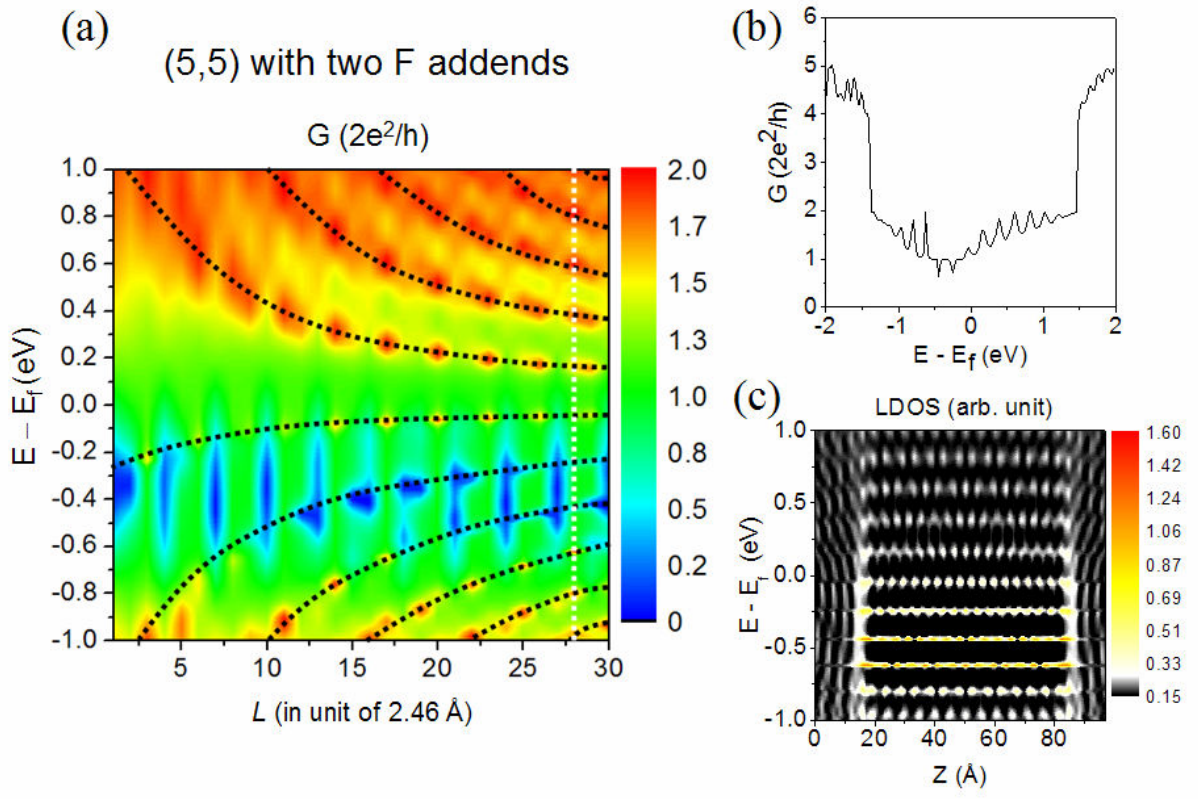

Figure 6.6: Increasing number of particle-in-box type resonant states (red peaks in (a)) are building up with increasing separation between two functional groups. Black trends lines are superimposed to indicate the $\Delta E \sim L^{-1}$ relation in (a). (b) Calculated conductance and (c) LDOS plots are showing energetically equally spaced resonant states. (b) and (c) are evaluated at L = 28 (68.88 Å) as indicated by a white vertical line in (a). Two Fs are monovalently attached at Z = 15.99 Å and Z = 84.87 Å respectively.

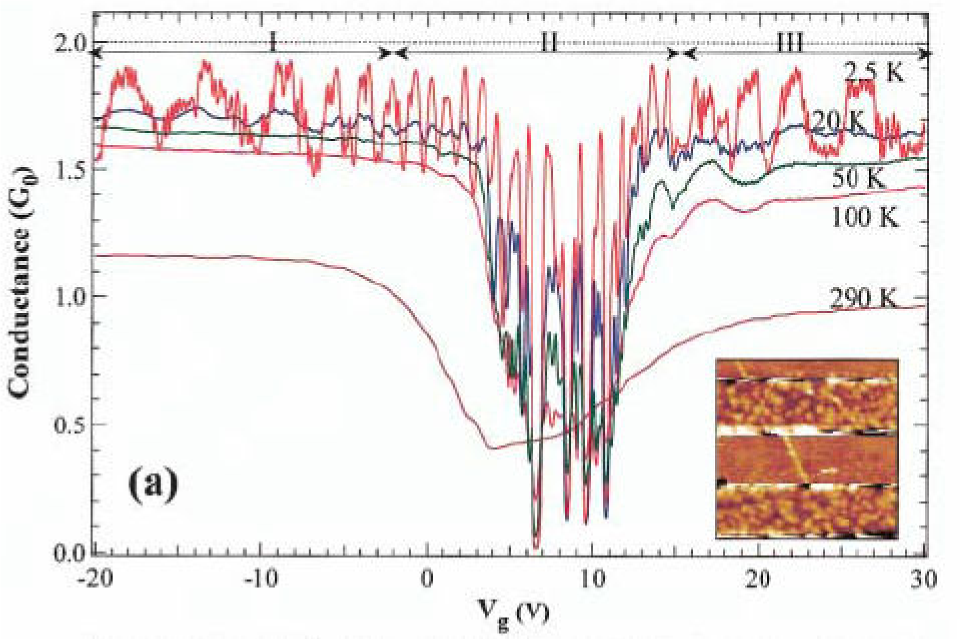

Figure 6.7: Experimental observation of quantum interference effect. The sample consists of a SWNT with diameter ~1.5 nm and length ~200 ± 10 nm. At room temperature, it shows a conductance of 1.1 G_0 in regimes **I** and **III** of the conductance (G) vs gate voltage (V_g) spectrum. A conductance dip is seen in regime **II**. The overall conductance of the sample increases as temperature decreases. At low temperature, conductance fluctuations vs V_g appear and the conductance peak approaches the quantum limit $2G_0$. In regime **I** and **III**, the rapid conductance oscillations are quasiperiodic and are attributed to resonance with standing waves in the 200 nm long tube. The slower fluctuations become dramatic in regime **II**. The origin of the slow fluctuations is attributed to resonance scattering by localized states in the nanotube [60].

resonant scattering effect at those two impurity sites (two Fs are monovalently attached at Z = 25.83 Å and Z = 84.87 Å respectively).

In addition, we also observed the increasing number of discrete "particle-in-box" type resonant states superimposed on the fluctuation as we increased the separation between two impurity sites (Figure 6.6(a)). This type of conductance oscillations has been observed in recent experimental and theoretical studies [60, 174-176] with two contacts of armchair nanotubes, and proven to be an intrinsic quantum interference phenomenon. Since two impurity sites, in our study, will act as two boundaries, the quantum confinement of reflected electron waves induces discrete resonant states, which cause oscillations as we can see in both the conductance and LDOS plots (Figure 6.6(b) and (c)). The energy spacing between adjacent resonant states in Figure 6.6(c) (two Fs are monovalently attached at Z = 15.99 Å and Z = 84.87 Å respectively) is found to be $\Delta E \approx 0.24$ eV, coinciding very well with the experimental data and the previous theoretical prediction $\Delta E = hv_F/2L \approx (1.68 \text{ eV nm})/L$ [60, 174-176, 184], where L = 68.88 Å is the separation of two impurity sites.

6.1.3 The concentration dependence

Recent experimental results [24-26, 62] show that the high degree of sidewall functionalization is possible. Thus, it is very desirable to systematically investigate the dependence of the conducting properties on the functional-group concentration. For such studies, we gradually increase the number of groups in a fixed-size section of the nanotube (Figure 6.8(a) and (b)). There are many possible ways of arranging the functionalization sites for a given concentration and the conducting behavior near the Fermi level is found to be very sensitive to the group configurations (Figure 6.8(C)). A small change in functional-group configuration results in a quite different conductance spectrum. However, energetically we did not find any significant differences among different configurations. Thus, to insure that our results are qualitatively relevant we performed calculations for 30 random configurations at each concentration. The results are shown in Figure 6.9 with the solid line representing the average and the gray area indicating the spread of conductance values over 30 randomly generated configurations.

In the case of monovalent-functional groups, the conductance spectrum near the Fermi level carries the molecular signature of the impurity state at low concentrations of groups.

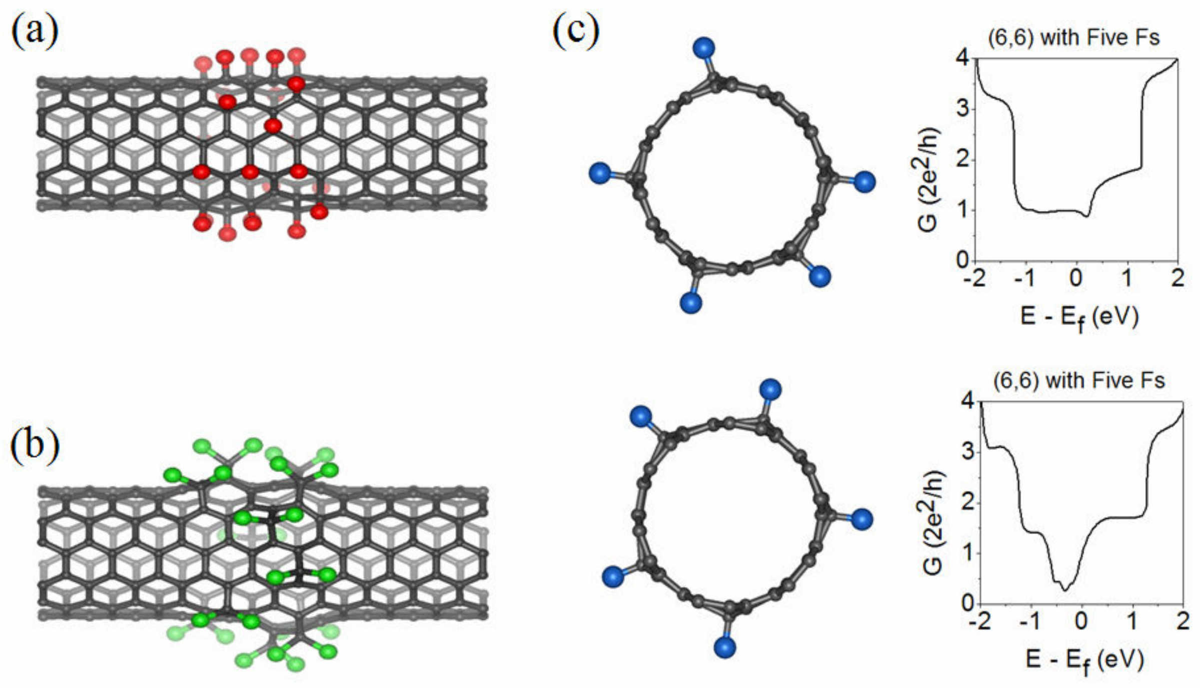

Figure 6.8: Computational models to study the conductance dependence on functional-group concentrations and configurations: (a) monovalently functionalized tube; (b) divalently functionalized tube; (c) calculated conductance plots show strong dependence on group configurations (five Fs attached).

As the concentration increases, this signature is washed away and the conductance decreases rapidly for a wide range of energy, independent of the functionalization group. Figure 6.9 shows results of monovalently functionalized (5,5) tube with F additions (Figure 6.9(a)) and NH_2 additions (Figure 6.9(b)) at different modification ratios (F:C = 5 %, 10 %, and 25%, respectively). The conductance minimum, at the energy of the molecule-specific-impurity state level (~ -0.4 eV for -F and ~0.0 eV for -NH_2), is clearly seen at the low modification ratio of 5 %. This feature is no longer there in the case of 10 % concentration, and the average conductance near the Fermi level is substantially reduced. At 25% concentration, the conductance approaches zero. This feature is generally observed for the other monovalent groups studied. Thus, we conclude that monovalent-functionalized CNTs lose their metallic character at high concentrations of additions.

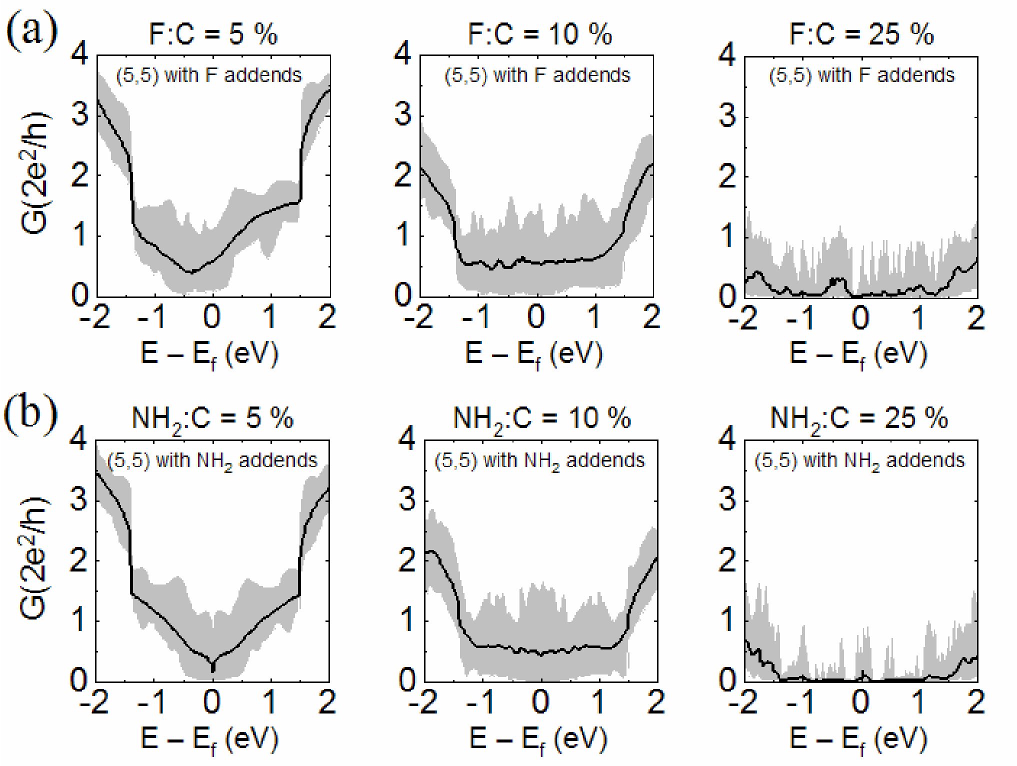

Figure 6.9: Conductance calculations (on 30 different configurations of functional groups for each modification ratio in all graphs) of monovalently functionalized (5,5) with (a) Fs and (b) NH_2 groups. Three different modification ratios (5%, 10%, and 25% respectively) are shown for each case. Solid lines and shaded areas represent the average conductance and max-min ranges of the conductance fluctuations respectively. At low concentrations (5%), the conductance spectrum near the Fermi level carries the molecular signature of the impurity state. At about 25%, SWNTs lose their metallic character.

6.2 Divalently functionalized SWNTs

6.2.1 Conducting behavior at low functional-group concentrations

As the previous study pointed out, in the cases of divalent functionalization, two impurity states induced by two neighboring functional sites are shifted away from the Fermi level due to the rehybridization into bonding and anti-bonding states. As a consequence, the overall electronic structures of metallic nanotubes near the Fermi level are not strongly affected by the divalent sidewall functionalizations at low concentrations of groups.

(a) (6, 6) with -COOH

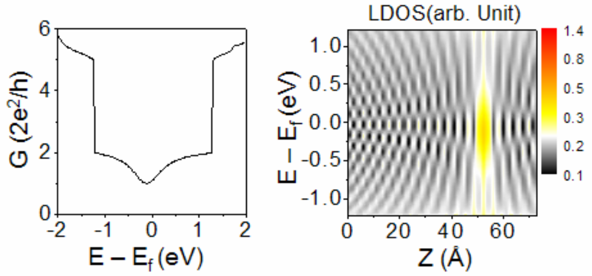

(b) (6, 6) with >NH with sidewall opening

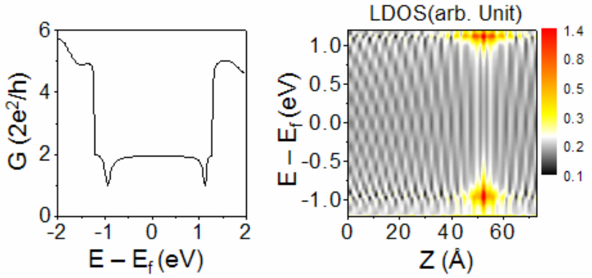

(c) (6, 6) with >NH without sidewall opening

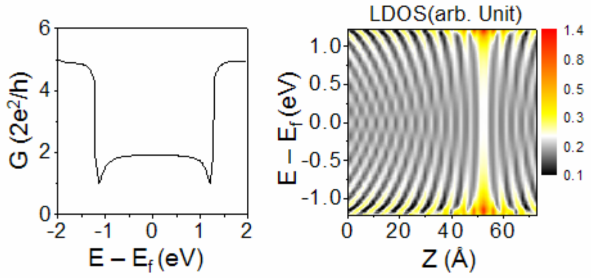

Figure 6.10: The calculated conductance and LDOS near the Fermi level as a function of energy for a (6, 6) tube. The functional-group is located $Z = 51.66$ Å in all three cases. (a) monovalent -COOH addition. The functional-group-induced localized impurity state can be seen to be near the Fermi level in the LDOS plot. There is a corresponding conductance dip. (b) Divalent >NH addition with sidewall opening, and (c) divalent >NH addition without sidewall opening. In both cases the rehybridized impurity states can be seen to be located far away from the Fermi level in the LDOS plots. The corresponding conductances show little change near the Fermi level.

Our calculations show that the conductance near the Fermi level is almost unaffected by the divalent functionalization with a single functional group (>NH, >CCl_2, >CH_2, and >O were considered in our study). Regardless whether the side wall is open (C-C bond on the CNT is broken, Figure 6.10(b)) or closed (the C-C bond is not broken, Figure 6.10(c)) the same conclusion is found, even though there are structural differences between two cases.

This result can be understood by examining the electronic states created by the functional group. The rehybridization of the two neighboring impurity states creates strong localized bonding and anti-bonding states which are located far away from the Fermi level. This can be clearly seen in Figure 6.10(b) and Figure 6.10(c), where significant changes in conductance are showing up 1eV above/below the Fermi level. This suggests that the C-C bond, even when it is not broken, is significantly weakened due to the interaction with the divalent functional group.

6.2.2 Conducting behavior at high functional-group concentrations

Even at relatively high concentrations of divalent functional groups, this rehybridization effect is found to remain strong. Examples of our calculation for CCl_2 functionalized (6,6) tube are also shown in Figure 6.11(b) for the case of no side-wall opening (no broken C-C bond), and in Figure 6.11(c) for the case with side-wall opening (broken C-C bond). In all three concentration ratios (12.5%, 18.8%, and 25%) studied, the metallic behavior is found to be robust near the Fermi level. Even at 25%, the average conductance near the Fermi level is still above 50% of that of a perfect tube. Qualitatively we found the same results whether the side-wall is open or not. This suggests that the bonding-antibonding rehybridization effect of the functional-group-induced impurity states still prevails even at high concentration ratios of divalent groups.

The dramatic difference between the monovalent and the divalent cases can be more clearly seen in Figure 6.12, where we plotted the conductance at the Fermi level vs. the functional-group concentration. The conductance of the monovalently functionalized tube decreases rapidly with the increasing concentration, and the nanotube loses its metallicity around 25% modification, while for the divalent cases the CNTs remain substantially conductive.

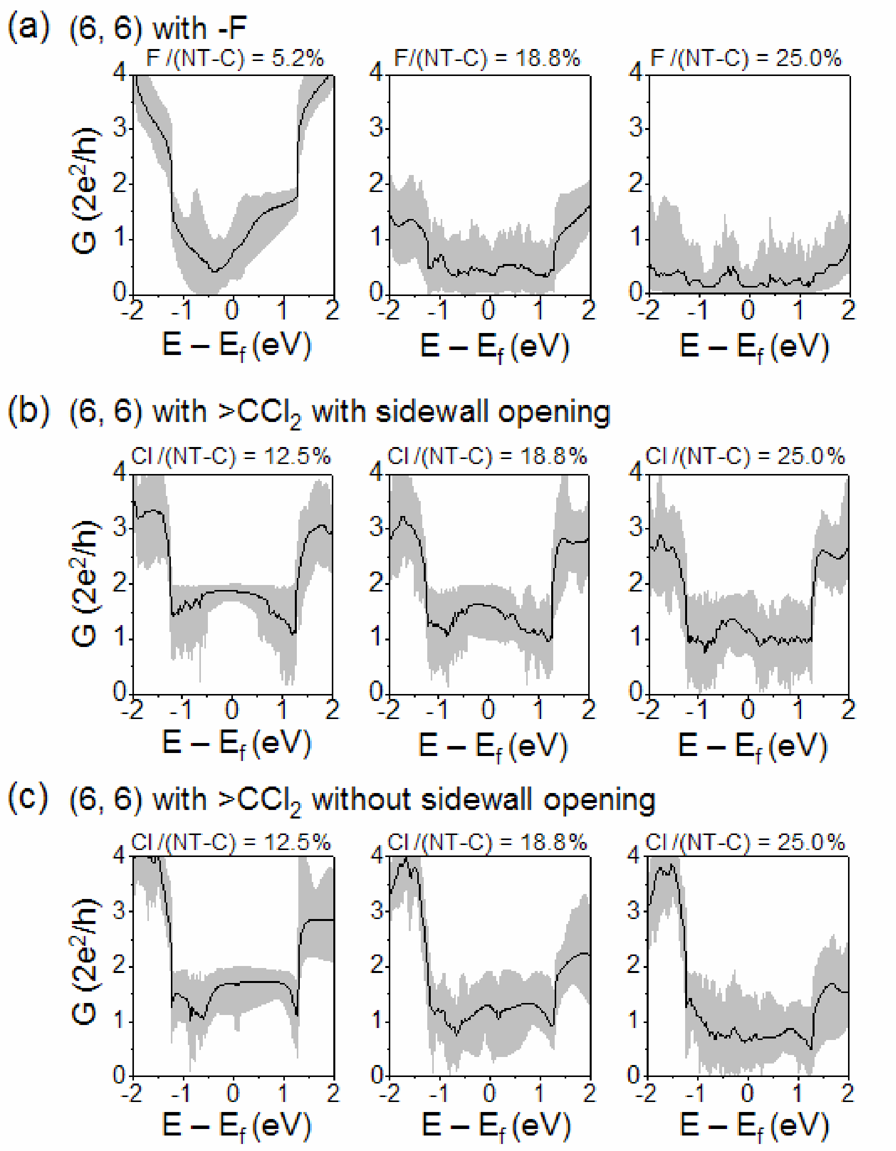

Figure 6.11: Conductance calculations (on 30 different configurations of functional groups for each modification ratio in all graphs) of (a) monovalently functionalized (6, 6) with Fs, (b) divalently functionalized (6, 6) with >CCl2 with sidewall opening, and (c) divalently functionalized (6, 6) with >CCl2 without sidewall opening. Three different modification ratios are shown for each case. Solid lines and shaded areas represent the average conductance and max-min ranges of the conductance fluctuations respectively.

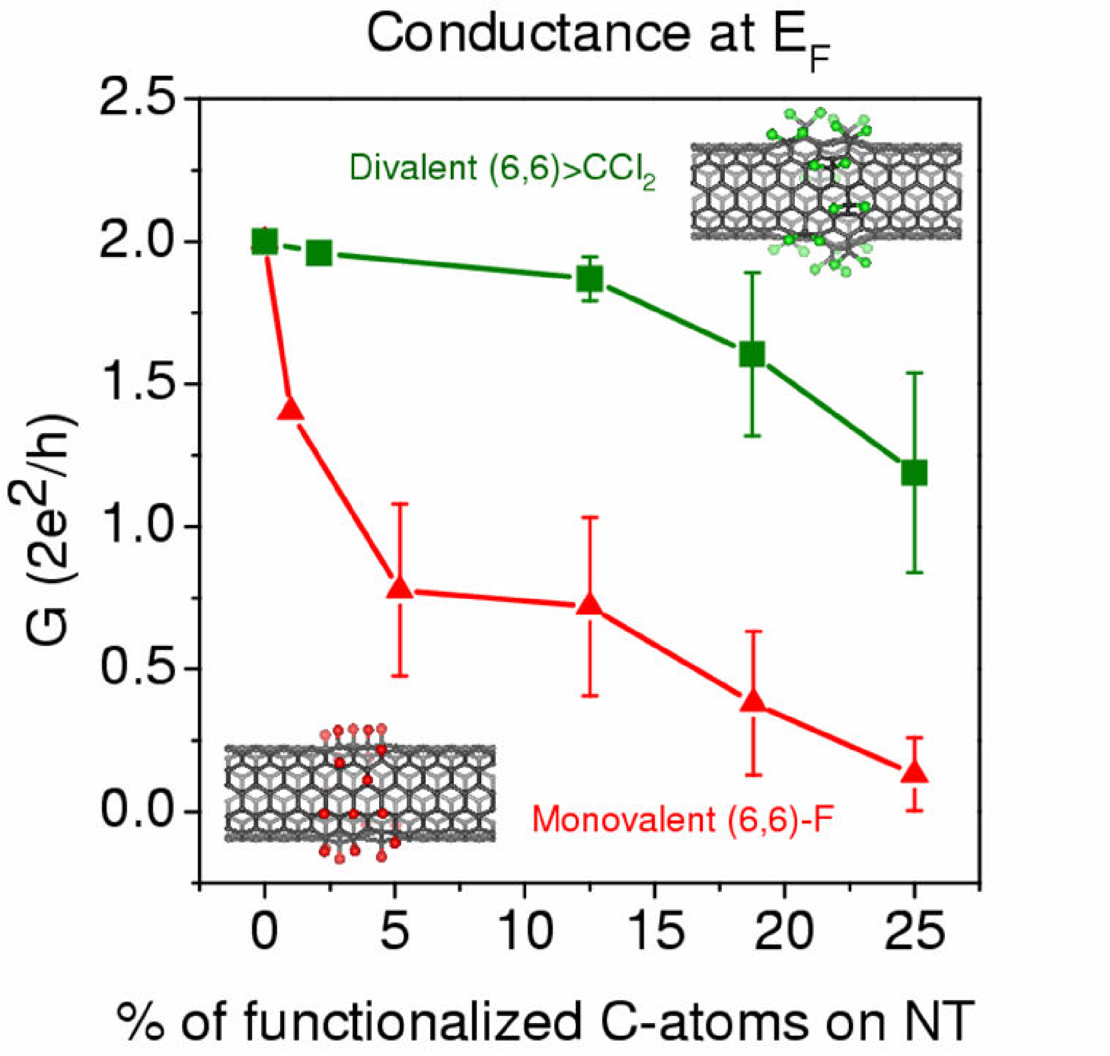

Figure 6.12: The conductance at the Fermi level vs. the functional-group concentration for monovalent ((6, 6) with F additions) and divalent ((6, 6) with >CCl2, with sidewall opening) functionalization. Error bars represent the standard deviation range from the average value. The graph shows that monovalent functionalizations decrease the conductance rapidly, and the CNTs lose metallicity around 25% modification ratio, while for divalent additions the conductive properties of CNTs remain robust.

6.3 Summary of transport properties

Systematic dependence on the functional-group concentration is investigated for both monovalent and divalent sidewall additions. We found that for monovalent bonding the functional-group-induced impurity state resides near the Fermi level, thus it acts as a strong scattering center and the ballistic conducting properties can be significantly affected. At low concentrations of monovalent additions quantum interference effects of electron waves are observed, such as resonant scattering and particle-in-box type resonant states. The conductance is found to decreases rapidly with the functional-group concentration and approaches zero at around 25% group to C ratio. In contrast, the divalent functionalization has a very small effect on the conductance near the Fermi level due to the rehybridization of two adjacent impurity states into bonding and anti-bonding states located far away from the Fermi level. With increasing functional-group concentration, the conductance is reduced gradually. Evan at 25% concentration, the conductance still remains more than 50% of that of a perfect nanotube.

Chapter 7

Conclusion

In the preceding chapters we have investigated electronic and transport properties of covalent sidewall functionalized SWNTs with either monovalent or divalent functional groups. We found that covalent functionalizations not only introduce local structural defects but also significantly disturb the delocalized π-electron system of the nanotubes by changing the local carbon bonding structure from sp^2 to sp^3 at the functional sites. Our careful computational analysis revealed several novel physical effects involving these intriguing micro-chemical processes of SWNTS.

The tube-(functional group) interaction was found to be determined by several factors. First, we showed that the electronic structure of nanotubes plays a crucial role in determining the strength of the interaction. The existence of available electrons near the Fermi level allows metallic tubes to make a stronger bonding to the functional group than semiconducting ones. The curvature of the tubes is also important factor which has been recognized since the early stages of nanotube research. The intrinsic cylindrical curvature of the nanotube sidewalls induces strain predominantly in the circumferential direction of the tube. The strained sp^2 carbon bonding structure makes the nanotube reactive to the functionalization. Thus, tubes with higher curvature (smaller diameter) are expected to be more reactive. Our binding energy studies showed consistent results. We found that the binding energy between the functional-group and the nanotube generally decreases with increasing modification ratio of SWNTs.

Covalent functionalizations universally induce local impurity states. This impurity state turns out to control the electronic and transport properties of chemically modified SWNTs. In the case of monovalent functionalization, the energetic position of the functional-group-induced impurity state is found to be functional group specific. However, in all cases studied, it is close to the Fermi level. At a low degree of functionalization, we found that the impurity state of functionalized semiconducting tubes is located within the band gap, and its effect on the electronic structure of the parent tube is mild and tightly localized around the functional sites. On the other hand, the metallic π and π^* band crossing in metallic nanotubes is strongly affected by covalent functionalization near the Fermi level and the effect is extended over a large area of the nanotube. These aspects of functional-group-induced impurity states are confirmed by our band structure and wavefunction studies.

Since the local electronic structure at the functional site is different from that of the parent nanotube, one can expect to see scatterings of conducting electrons in metallic nanotubes. Based on our conductance and LDOS calculations, we showed that the impurity state induced by monovalent-functional groups is indeed a strong scattering center of the electron conduction near the Fermi level. Drastic disturbance on the conducting behavior of metallic tube was observed. Each functional group exhibits its own energetic position for the center of the electron scattering which correlates well with the position of the impurity state, and creates significant dips in the ballistic conductance of metallic nanotubes.

Quantum interference effects were studied with two identical monovalent functional groups on metallic nanotubes. As the separation between two functional groups gradually increases, a severe conductance reduction appears periodically at the functional-group-specific impurity state energy level. The spatial periodicity is found to be the same as the Fermi wavelength of armchair nanotubes. Therefore, this feature can be attributed to the electron resonant scattering at two local impurity states. In addition, the increasing number of particle-in-box type resonant states was observed with increasing separation due to the buildup of standing waves between the two functional-group boundaries. Energetically equally spaced resonant states have been manifested in our calculated conductance and LDOS plots.

All monovalent functional groups studied cause a substantial disturbance in the ballistic electron conduction of metallic nanotubes near the Fermi level. Since the conducting behavior of functionalized tubes shows strong dependence upon the configurations of functional groups, the statistical average over different configurations were employed at each functional-group concentration to get qualitatively relevant results on the concentration dependence. At low concentrations, the conductance spectrum carries the molecular signature, i.e. the greatest conductance reduction happens at the functional-group-specific energy level of the impurity state. As the concentration increases, this signature is washed away and the conductance decreases rapidly for a wide range of energies and the nanotube loses its metallicity at high concentrations of functional groups.

Divalent functional groups form bridge-like covalent bonds with two carbon atoms in the sidewalls of nanotubes. Two impurity states at two vicinal sites overlap significantly and rehybridize into bonding and antibonding states located relatively far away from the Fermi level. Consequently, at low concentration of functional groups, the electronic and the transport properties of the parent nanotubes near the Fermi level are only mildly affected by the functionalization. Even at high concentrations, nanotubes are found to remain substantially conductive, suggesting that the bonding-antibonding rehybridization effect of impurity states still prevails.

With improvement in the accuracy of our transport calculations, which can be achieved by the implementation of an *ab initio* type Hamiltonian with self-consistent charge density, our computational methods and analysis techniques may be further extended to investigate more complicated systems such as (transition-metal)-CNT hybrid systems or (bio-molecule)-CNT hybrid systems.

In this work, some of novel physical effects of the chemical functionalization of carbon nanotubes have been revealed. I believe that this will provide a solid foundation for the successful future development of this research area and open up a way to practical applications of functionalized SWNTs, such as micro-electrical, band structure engineering, bio and chemical sensor, and in many more areas.

APPENDIX

List of publications

1. Jijun Zhao, Hyoungki Park, Jie Han, Jian Ping Lu, "Electronic properties of carbon nanotubes with covalent sidewall functionalization", *J. Phys. Chem.* B. 108, 4227(2004).

2. L.E. McNeil, H. Park, J.P. Lu and M.J. Peters, "Effect of residual catalyst on the vibrational modes of single-walled carbon nanotubes", *J. Appl. Phys.* 96, 5158(2004).

3. Jijun Zhao, Zhongfang Chen, Hyoungki Park, Paul von Ragué Schleyer, Jian Ping Lu, "Engineering the electronic structures of single-walled carbon nanotubes by chemical functionalizations", *ChemPhysChem.* 6, 598(2005).

4. Hyoungki Park, Jijun Zhao, Jian Ping. Lu, "Distinct properties of SWNTs with monovalent side-wall additions", *Nanotechnology.* 16, 635(2005).

5. Hyoungki Park, Jijun Zhao, Jian Ping Lu, "Effects of sidewall functionalization on conducting properties of SWNTs", *Nano Letters*, 6, 916(2006).

REFERENCES

[1] S. Iijima, Helical Microtubules of Graphitic Carbon, *Nature* 354, 56 (1991).

[2] A. Bachtold, P. Hadley, T. Nakanishi, and C. Dekker, Logic circuits with carbon nanotube transistors, *Science* 294, 1317 (2001).

[3] V. Lordi, N. Yao, and J. Wei, Method for supporting platinum on single-walled carbon nanotubes for a selective hydrogenation catalyst, *Chem. Mater.* 13, 733 (2001).

[4] J. M. Planeix, N. Coustel, B. Coq, V. Brotons, P. S. Kumbhar, R. Dutartre, P. Geneste, P. Bernier, and P. M. Ajayan, Application of Carbon Nanotubes as Supports in Heterogeneous Catalysis, *J. Am. Chem. Soc.* 116, 7935 (1994).

[5] R. H. Baughman, C. X. Cui, A. A. Zakhidov, Z. Iqbal, J. N. Barisci, G. M. Spinks, G. G. Wallace, A. Mazzoldi, D. De Rossi, A. G. Rinzler, O. Jaschinski, S. Roth, and M. Kertesz, Carbon nanotube actuators, *Science* 284, 1340 (1999).

[6] R. H. Baughman, A. A. Zakhidov, and W. A. de Heer, Carbon nanotubes - the route toward applications, *Science* 297, 787 (2002).

[7] S. S. Fan, M. G. Chapline, N. R. Franklin, T. W. Tombler, A. M. Cassell, and H. J. Dai, Self-oriented regular arrays of carbon nanotubes and their field emission properties, *Science* 283, 512 (1999).

[8] W. Zhao, C. H. Song, and P. E. Pehrsson, Water-soluble and optically pH-sensitive single-walled carbon nanotubes from surface modification, *J. Am. Chem. Soc.* 124, 12418 (2002).

[9] J. Kong, N. R. Franklin, C. W. Zhou, M. G. Chapline, S. Peng, K. J. Cho, and H. J. Dai, Nanotube molecular wires as chemical sensors, *Science* 287, 622 (2000).

[10] C. M. Yang, K. Kaneko, M. Yudasaka, and S. Iijima, Effect of purification on pore structure of HiPco single-walled carbon nanotube aggregates, *Nano Lett.* 2, 385 (2002).

[11] S. S. Wong, J. D. Harper, P. T. Lansbury, and C. M. Lieber, Carbon nanotube tips: High-resolution probes for imaging biological systems, *J. Am. Chem. Soc.* 120, 603 (1998).

[12] A. Hirsch, Functionalization of single-walled carbon nanotubes, *Angew. Chem., Int. Ed.* 41, 1853 (2002).

[13] S. B. Sinnott, Chemical functionalization of carbon nanotubes, *Journal of Nanoscience and Nanotechnology* 2, 113 (2002).

[14] J. L. Bahr, and J. M. Tour, Covalent chemistry of single-wall carbon nanotubes, *J. Mater. Chem.* 12, 1952 (2002).

[15] V. Georgakilas, K. Kordatos, M. Prato, D. M. Guldi, M. Holzinger, and A. Hirsch, Organic functionalization of carbon nanotubes, *J. Am. Chem. Soc.* 124, 760 (2002).

[16] J. L. Bahr, J. P. Yang, D. V. Kosynkin, M. J. Bronikowski, R. E. Smalley, and J. M. Tour, Functionalization of carbon nanotubes by electrochemical reduction of aryl diazonium salts: A bucky paper electrode, *J. Am. Chem. Soc.* 123, 6536 (2001).

[17] E. T. Mickelson, C. B. Huffman, A. G. Rinzler, R. E. Smalley, R. H. Hauge, and J. L. Margrave, Fluorination of single-wall carbon nanotubes, *Chem. Phys. Lett.* 296, 188 (1998).

[18] R. J. Chen, Y. G. Zhan, D. W. Wang, and H. J. Dai, Noncovalent sidewall functionalization of single-walled carbon nanotubes for protein immobilization, *J. Am. Chem. Soc.* 123, 3838 (2001).

[19] J. J. Zhao, J. P. Lu, J. Han, and C. K. Yang, Noncovalent functionalization of carbon nanotubes by aromatic organic molecules, *Appl. Phys. Lett.* 82, 3746 (2003).

[20] J. Chen, M. A. Hamon, H. Hu, Y. S. Chen, A. M. Rao, P. C. Eklund, and R. C. Haddon, Solution properties of single-walled carbon nanotubes, *Science* 282, 95 (1998).

[21] M. J. O'Connell, P. Boul, L. M. Ericson, C. Huffman, Y. H. Wang, E. Haroz, C. Kuper, J. Tour, K. D. Ausman, and R. E. Smalley, Reversible water-solubilization of single-walled carbon nanotubes by polymer wrapping, *Chem. Phys. Lett.* 342, 265 (2001).

[22] J. E. Riggs, Z. X. Guo, D. L. Carroll, and Y. P. Sun, Strong luminescence of solubilized carbon nanotubes, *J. Am. Chem. Soc.* 122, 5879 (2000).

[23] A. Star, J. F. Stoddart, D. Steuerman, M. Diehl, A. Boukai, E. W. Wong, X. Yang, S. W. Chung, H. Choi, and J. R. Heath, Preparation and properties of polymer-wrapped single-walled carbon nanotubes, *Angew. Chem., Int. Ed.* 40, 1721 (2001).

[24] F. Pompeo, and D. E. Resasco, Water solubilization of single-walled carbon nanotubes by functionalization with glucosarnine, *Nano Lett.* 2, 369 (2002).

[25] C. A. Dyke, and J. M. Tour, Unbundled and highly functionalized carbon nanotubes from aqueous reactions, *Nano Lett.* 3, 1215 (2003).

[26] M. S. Strano, C. A. Dyke, M. L. Usrey, P. W. Barone, M. J. Allen, H. W. Shan, C. Kittrell, R. H. Hauge, J. M. Tour, and R. E. Smalley, Electronic structure control of single-walled carbon nanotube functionalization, *Science* 301, 1519 (2003).

[27] S. Iijima, and T. Ichihashi, Single-Shell Carbon Nanotubes of 1-Nm Diameter, *Nature* 363, 603 (1993).

[28] D. S. Bethune, C. H. Kiang, M. S. Devries, G. Gorman, R. Savoy, J. Vazquez, and R. Beyers, Cobalt-Catalyzed Growth of Carbon Nanotubes with Single-Atomic-Layerwalls, *Nature* 363, 605 (1993).

[29] C. Journet, W. K. Maser, P. Bernier, A. Loiseau, M. L. delaChapelle, S. Lefrant, P. Deniard, R. Lee, and J. E. Fischer, Large-scale production of single-walled carbon nanotubes by the electric-arc technique, *Nature* 388, 756 (1997).

[30] A. Thess, R. Lee, P. Nikolaev, H. J. Dai, P. Petit, J. Robert, C. H. Xu, Y. H. Lee, S. G. Kim, A. G. Rinzler, D. T. Colbert, G. E. Scuseria, D. Tomanek, J. E. Fischer, and R. E. Smalley, Crystalline ropes of metallic carbon nanotubes, *Science* 273, 483 (1996).

[31] P. Nikolaev, M. J. Bronikowski, R. K. Bradley, F. Rohmund, D. T. Colbert, K. A. Smith, and R. E. Smalley, Gas-phase catalytic growth of single-walled carbon nanotubes from carbon monoxide, *Chem. Phys. Lett.* 313, 91 (1999).

[32] M. S. Dresselhaus, G. Dresselhaus, and R. Saito, Carbon-Fibers Based on C-60 and Their Symmetry, *Phys. Rev. B* 45, 6234 (1992).

[33] N. Hamada, S. Sawada, and A. Oshiyama, New One-Dimensional Conductors - Graphitic Microtubules, *Phys. Rev. Lett.* 68, 1579 (1992).

[34] J. W. Mintmire, B. I. Dunlap, and C. T. White, Are Fullerene Tubules Metallic, *Phys. Rev. Lett.* 68, 631 (1992).

[35] M. H. Ge, and K. Sattler, Scanning-Tunneling-Microscopy of Single-Shell Nanotubes of Carbon, *Appl. Phys. Lett.* 65, 2284 (1994).

[36] J. W. G. Wildoer, L. C. Venema, A. G. Rinzler, R. E. Smalley, and C. Dekker, Electronic structure of atomically resolved carbon nanotubes, *Nature* 391, 59 (1998).

[37] T. W. Odom, J. L. Huang, P. Kim, and C. M. Lieber, Atomic structure and electronic properties of single-walled carbon nanotubes, *Nature* 391, 62 (1998).

[38] Z. J. Liu, Q. Zhang, and L. C. Qin, Determination and mapping of diameter and helicity for single-walled carbon nanotubes using nanobeam electron diffraction, *Phys. Rev. B* 71 (2005).

[39] C. H. Olk, and J. P. Heremans, Scanning Tunneling Spectroscopy of Carbon Nanotubes, *J. Mater. Res.* 9, 259 (1994).

[40] R. Hoper, R. K. Workman, D. Chen, D. Sarid, T. Yadav, J. C. Withers, and R. O. Loutfy, Single-Shell Carbon Nanotubes Imaged by Atomic-Force Microscopy, *Surf. Sci.* 311, L731 (1994).

[41] P. R. Wallace, The band theory of graphite, *Phys. Rev.* 71, 622 (1947).

[42] R. Saito, G. Dresselhaus, and M. S. Dresselhaus, *Physical properties of carbon nanotubes* (Imperial College Press, London, 1998).

[43] M. Ouyang, J. L. Huang, C. L. Cheung, and C. M. Lieber, Energy gaps in "metallic" single-walled carbon nanotubes, *Science* 292, 702 (2001).

[44] R. Saito, M. Fujita, G. Dresselhaus, and M. S. Dresselhaus, Electronic-Structure of Chiral Graphene Tubules, *Appl. Phys. Lett.* 60, 2204 (1992).

[45] S. J. Tans, M. H. Devoret, H. J. Dai, A. Thess, R. E. Smalley, L. J. Geerligs, and C. Dekker, Individual single-wall carbon nanotubes as quantum wires, *Nature* 386, 474 (1997).

[46] D. Mann, A. Javey, J. Kong, Q. Wang, and H. J. Dai, Ballistic transport in metallic nanotubes with reliable Pd ohmic contacts, *Nano Lett.* 3, 1541 (2003).

[47] R. A. Jishi, M. S. Dresselhaus, and G. Dresselhaus, Electron-Phonon Coupling and the Electrical-Conductivity of Fullerene Nanotubules, *Phys. Rev. B* 48, 11385 (1993).

[48] Z. Yao, C. L. Kane, and C. Dekker, High-field electrical transport in single-wall carbon nanotubes, *Phys. Rev. Lett.* 84, 2941 (2000).

[49] P. L. McEuen, and J. Y. Park, Electron transport in single-walled carbon nanotubes, *MRS Bulletin* 29, 272 (2004).

[50] A. Javey, J. Guo, M. Paulsson, Q. Wang, D. Mann, M. Lundstrom, and H. J. Dai, High-field quasiballistic transport in short carbon nanotubes, *Phys. Rev. Lett.* 92 (2004).

[51] L. Balents, and M. P. A. Fisher, Correlation effects in carbon nanotubes, *Phys. Rev. B* 55, 11973 (1997).

[52] M. Bockrath, D. H. Cobden, P. L. McEuen, N. G. Chopra, A. Zettl, A. Thess, and R. E. Smalley, Single-electron transport in ropes of carbon nanotubes, *Science* 275, 1922 (1997).

[53] J. Nygard, D. H. Cobden, M. Bockrath, P. L. McEuen, and P. E. Lindelof, Electrical transport measurements on single-walled carbon nanotubes, *Applied Physics a-Materials Science & Processing* 69, 297 (1999).

[54] M. Bockrath, D. H. Cobden, J. Lu, A. G. Rinzler, R. E. Smalley, T. Balents, and P. L. McEuen, Luttinger-liquid behaviour in carbon nanotubes, *Nature* 397, 598 (1999).

[55] C. Kane, L. Balents, and M. P. A. Fisher, Coulomb interactions and mesoscopic effects in carbon nanotubes, *Phys. Rev. Lett.* 79, 5086 (1997).

[56] R. Egger, and A. O. Gogolin, Effective low-energy theory for correlated carbon nanotubes, *Phys. Rev. Lett.* 79, 5082 (1997).

[57] Z. Yao, H. W. C. Postma, L. Balents, and C. Dekker, Carbon nanotube intramolecular junctions, *Nature* 402, 273 (1999).

[58] H. W. C. Postma, M. de Jonge, Z. Yao, and C. Dekker, Electrical transport through carbon nanotube junctions created by mechanical manipulation, *Phys. Rev. B* 62, 10653 (2000).

[59] H. W. C. Postma, T. Teepen, Z. Yao, M. Grifoni, and C. Dekker, Carbon nanotube single-electron transistors at room temperature, *Science* 293, 76 (2001).

[60] J. Kong, E. Yenilmez, T. W. Tombler, W. Kim, H. J. Dai, R. B. Laughlin, L. Liu, C. S. Jayanthi, and S. Y. Wu, Quantum interference and ballistic transmission in nanotube electron waveguides, *Phys. Rev. Lett.* 87, 106801 (2001).

[61] J. Zhang, H. L. Zou, Q. Qing, Y. L. Yang, Q. W. Li, Z. F. Liu, X. Y. Guo, and Z. L. Du, Effect of chemical oxidation on the structure of single-walled carbon nanotubes, *J. Phys. Chem. B* 107, 3712 (2003).

[62] K. Kamaras, M. E. Itkis, H. Hu, B. Zhao, and R. C. Haddon, Covalent bond formation to a carbon nanotube metal, *Science* 301, 1501 (2003).

[63] M. Shim, A. Javey, N. W. S. Kam, and H. J. Dai, Polymer functionalization for air-stable n-type carbon nanotube field-effect transistors, *J. Am. Chem. Soc.* 123, 11512 (2001).

[64] J. Kong, and H. J. Dai, Full and modulated chemical gating of individual carbon nanotubes by organic amine compounds, *J. Phys. Chem. B* 105, 2890 (2001).

[65] S. Banerjee, and S. S. Wong, Functionalization of carbon nanotubes with a metal-containing molecular complex, *Nano Lett.* 2, 49 (2002).

[66] Q. D. Chen, L. M. Dai, M. Gao, S. M. Huang, and A. Mau, Plasma activation of carbon nanotubes for chemical modification, *J. Phys. Chem. B* 105, 618 (2001).

[67] T. Sainsbury, and D. Fitzmaurice, Templated assembly of semiconductor and insulator nanoparticles at the surface of covalently modified multiwalled carbon nanotubes, *Chem. Mater.* 16, 3780 (2004).

[68] K. Balasubramanian, and M. Burghard, Chemically functionalized carbon nanotubes, *Small* 1, 180 (2005).

[69] S. Niyogi, M. A. Hamon, H. Hu, B. Zhao, P. Bhowmik, R. Sen, M. E. Itkis, and R. C. Haddon, Chemistry of single-walled carbon nanotubes, *Acc. Chem. Res.* 35, 1105 (2002).

[70] E. V. Basiuk, M. Monroy-Pelaez, I. Puente-Lee, and V. A. Basiuk, Direct solvent-free amination of closed-cap carbon nanotubes: A link to fullerene chemistry, *Nano Lett.* 4, 863 (2004).

[71] H. Park, J. J. Zhao, and J. P. Lu, Distinct properties of single-wall carbon nanotubes with monovalent sidewall additions, *Nanotechnology* 16, 635 (2005).

[72] K. Mylvaganam, and L. C. Zhang, Nanotube functionalization and polymer grafting: An ab initio study, *J. Phys. Chem. B* 108, 15009 (2004).

[73] Z. F. Chen, W. Thiel, and A. Hirsch, Reactivity of the convex and concave surfaces of single-walled carbon nanotubes (SWCNTs) towards addition reactions: Dependence on the carbon-atom pyramidalization, *ChemPhysChem* 4, 93 (2003).

[74] H. Hu, P. Bhowmik, B. Zhao, M. A. Hamon, M. E. Itkis, and R. C. Haddon, Determination of the acidic sites of purified single-walled carbon nanotubes by acid-base titration, *Chem. Phys. Lett.* 345, 25 (2001).

[75] E. Katz, and I. Willner, Biomolecule-functionalized carbon nanotubes: Applications in nanobioelectronics, *ChemPhysChem* 5, 1085 (2004).

[76] K. A. S. Fernando, Y. Lin, and Y. P. Sun, High aqueous solubility of functionalized single-walled carbon nanotubes, *Langmuir* 20, 4777 (2004).

[77] J. Chen, A. M. Rao, S. Lyuksyutov, M. E. Itkis, M. A. Hamon, H. Hu, R. W. Cohn, P. C. Eklund, D. T. Colbert, R. E. Smalley, and R. C. Haddon, Dissolution of full-length single-walled carbon nanotubes, *J. Phys. Chem. B* 105, 2525 (2001).

[78] M. A. Hamon, J. Chen, H. Hu, Y. S. Chen, M. E. Itkis, A. M. Rao, P. C. Eklund, and R. C. Haddon, Dissolution of single-walled carbon nanotubes, *Adv. Mater.* 11, 834 (1999).

[79] C. A. Dyke, and J. M. Tour, Overcoming the insolubility of carbon nanotubes through high degrees of sidewall functionalization, *Chem. Eur. J.* 10, 813 (2004).

[80] V. N. Khabashesku, W. E. Billups, and J. L. Margrave, Fluorination of single-wall carbon nanotubes and subsequent derivatization reactions, *Acc. Chem. Res.* 35, 1087 (2002).

[81] J. L. Stevens, A. Y. Huang, H. Q. Peng, L. W. Chiang, V. N. Khabashesku, and J. L. Margrave, Sidewall amino-functionalization of single-walled carbon nanotubes through fluorination and subsequent reactions with terminal diamines, *Nano Lett.* 3, 331 (2003).

[82] K. Balasubramanian, M. Friedrich, C. Y. Jiang, Y. W. Fan, A. Mews, M. Burghard, and K. Kern, Electrical transport and confocal Raman studies of electrochemically modified individual carbon nanotubes, *Adv. Mater.* 15, 1515 (2003).

[83] S. Banerjee, and S. S. Wong, Selective metallic tube reactivity in the solution-phase osmylation of single-walled carbon nanotubes, *J. Am. Chem. Soc.* 126, 2073 (2004).

[84] J. B. Cui, M. Burghard, and K. Kern, Reversible sidewall osmylation of individual carbon nanotubes, *Nano Lett.* 3, 613 (2003).

[85] M. Born, and R. Oppenheimer, Zur Quantentheorie der Molekeln, *Ann. Phys. (Leipzig)* 84, 457 (1927).

[86] P. Hohenberg, and W. Kohn, Inhomogeneous Electron Gas, *Phys. Rev. B* 136, B864 (1964).

[87] H. Englisch, and R. Englisch, Exact Density Functionals for Ground-State Energies .2. Details and Remarks, *Phys. Status Solidi B* 124, 373 (1984).

[88] H. Englisch, and R. Englisch, Exact Density Functionals for Ground-State Energies .1. General Results, *Phys. Status Solidi B* 123, 711 (1984).

[89] M. Levy, Electron-Densities in Search of Hamiltonians, *Phys. Rev. A* 26, 1200 (1982).

[90] M. Levy, Universal Variational Functionals of Electron-Densities, 1st-Order Density-Matrices, and Natural Spin-Orbitals and Solution of the V-Representability Problem, *Proc. Natl. Acad. Sci. U. S. A.* 76, 6062 (1979).

[91] T. L. Gilbert, Hohenberg-Kohn Theorem for Nonlocal External Potentials, *Phys. Rev. B* 12, 2111 (1975).

[92] L. H. Thomas, The calculation of atomic fields., *Proc. Camb. Phil. Soc.* 23, 542 (1927).

[93] E. Fermi, Un metodo statistico per la determinazione de alcune proprieta dell'atome., *Rend. Accad. Naz. Lincei.* 6, 602 (1927).

[94] E. Fermi, Eine statistische Methode zur Bestimmung einiger Eigenschaften des Atoms und ihre Anwendung auf die Theorie des periodischen Systems der Elemente., *Z. Phys.* 48, 73 (1928).

[95] E. H. Lieb, Thomas-Fermi and Related Theories of Atoms and Molecules, *Rev. Mod. Phys.* 53, 603 (1981).

[96] E. Teller, On Stability of Molecules in Thomas-Fermi Theory, *Rev. Mod. Phys.* 34, 627 (1962).

[97] M. Foley, and P. A. Madden, Further orbital-free kinetic-energy functionals for ab initio molecular dynamics, *Phys. Rev. B* 53, 10589 (1996).

[98] E. Smargiassi, and P. A. Madden, Orbital-Free Kinetic-Energy Functionals for 1st-Principles Molecular-Dynamics, *Phys. Rev. B* 49, 5220 (1994).

[99] F. Perrot, Hydrogen Hydrogen Interaction in an Electron-Gas, *J. Phys.: Condens. Matter* 6, 431 (1994).

[100] M. Pearson, E. Smargiassi, and P. A. Madden, Abinitio Molecular-Dynamics with an Orbital-Free Density-Functional, *J. Phys.: Condens. Matter* 5, 3221 (1993).

[101] L. W. Wang, and M. P. Teter, Kinetic-Energy Functional of the Electron-Density, *Phys. Rev. B* 45, 13196 (1992).

[102] W. Kohn, and L. J. Sham, Self-Consistent Equations Including Exchange and Correlation Effects, *Phys. Rev.* 140, 1133 (1965).

[103] J. P. Perdew, and Y. Wang, Accurate and Simple Analytic Representation of the Electron-Gas Correlation-Energy, *Phys. Rev. B* 45, 13244 (1992).

[104] J. P. Perdew, K. Burke, and M. Ernzerhof, Generalized gradient approximation made simple, *Phys. Rev. Lett.* 77, 3865 (1996).

[105] J. P. Perdew, K. Burke, and M. Ernzerhof, Generalized gradient approximation made simple (vol 77, pg 3865, 1996), *Phys. Rev. Lett.* 78, 1396 (1997).

[106] A. D. Becke, A New Mixing of Hartree-Fock and Local Density-Functional Theories, *J. Chem. Phys.* 98, 1372 (1993).

[107] A. D. Becke, Density-Functional Thermochemistry .3. The Role of Exact Exchange, *J. Chem. Phys.* 98, 5648 (1993).

[108] M. C. Payne, M. P. Teter, D. C. Allan, T. A. Arias, and J. D. Joannopoulos, Iterative Minimization Techniques for Abinitio Total-Energy Calculations - Molecular-Dynamics and Conjugate Gradients, *Rev. Mod. Phys.* 64, 1045 (1992).

[109] M. D. Towler, A. Zupan, and M. Causa, Density functional theory in periodic systems using local Gaussian basis sets, *Comput. Phys. Commun.* 98, 181 (1996).

[110] T. A. Arias, Multiresolution analysis of electronic structure: Semicardinal and wavelet bases, *Rev. Mod. Phys.* 71, 267 (1999).

[111] B. Delley, An All-Electron Numerical-Method for Solving the Local Density Functional for Polyatomic-Molecules, *J. Chem. Phys.* 92, 508 (1990).

[112] B. Delley, From molecules to solids with the DMol(3) approach, *J. Chem. Phys.* 113, 7756 (2000).

[113] L. Kleinman, and D. M. Bylander, Efficacious Form for Model Pseudopotentials, *Phys. Rev. Lett.* 48, 1425 (1982).

[114] D. Vanderbilt, Soft Self-Consistent Pseudopotentials in a Generalized Eigenvalue Formalism, *Phys. Rev. B* 41, 7892 (1990).

[115] J. C. Slater, and G. F. Koster, Simplified LCAO method for the periodic potential problem, *Phys. Rev.* 94, 1489 (1954).

[116] F. Bloch, Quantum mechanics of electrons in crystals, *Z. Phys.* 52, 555 (1928).

[117] P. O. Lowdin, On the non-orthogonality problem connected with the use of atomic wave functions in the theory of molecules and crystals, *J. Chem. Phys.* 18, 365 (1950).

[118] D. J. Chadi, (110) Surface Atomic Structures of Covalent and Ionic Semiconductors, *Phys. Rev. B* 19, 2074 (1979).

[119] S. Froyen, and W. A. Harrison, Elementary Prediction of Linear Combination of Atomic Orbitals Matrix-Elements, *Phys. Rev. B* 20, 2420 (1979).

[120] L. Goodwin, A. J. Skinner, and D. G. Pettifor, Generating Transferable Tight-Binding Parameters - Application to Silicon, *Europhys. Lett.* 9, 701 (1989).

[121] J. Dorantesdavila, A. Vega, and G. M. Pastor, Self-Consistent Theory of Overlap Interactions in the Tight-Binding Method, *Phys. Rev. B* 47, 12995 (1993).

[122] J. Dorantesdavila, and G. M. Pastor, Alternative Local Approach to Nonorthogonal Tight-Binding Theory - Environment Dependence of the Interaction Parameters in an Orthogonal Basis, *Phys. Rev. B* 51, 16627 (1995).

[123] D. A. Mirabella, C. M. Aldao, and R. R. Deza, Effects of Orbital Nonorthogonality on Band-Structure within the Tight-Binding Scheme, *Phys. Rev. B* 50, 12152 (1994).

[124] B. A. McKinnon, and T. C. Choy, Significance of Nonorthogonality in Tight-Binding Models, *Phys. Rev. B* 52, 14531 (1995).

[125] R. Hoffmann, An Extended Huckel Theory. I. Hydrocarbons, *J. Chem. Phys.* 39, 1397 (1963).

[126] A. B. Anderson, Derivation of Extended Huckel Method with Corrections - One Electron Molecular-Orbital Theory for Energy-Level and Structure Determinations, *J. Chem. Phys.* 62, 1187 (1975).

[127] S. Datta, *Electronic Transport in Mesoscopic Systems* (Cambridge University Press, Cambridge, United Kingdom, 1995).

[128] M. Buttiker, Four-teminal phase-coherent conductance, *Phys. Rev. Lett.* 57, 1761 (1986).

[129] M. B. Nardelli, Electronic transport in extended systems: Application to carbon nanotubes, *Phys. Rev. B* 60, 7828 (1999).

[130] L. Chico, L. X. Benedict, S. G. Louie, and M. L. Cohen, Quantum conductance of carbon nanotubes with defects, *Phys. Rev. B* 54, 2600 (1996).

[131] F. Garciamoliner, and V. R. Velasco, Matching Methods for Single and Multiple Interfaces - Discrete and Continuous Media, *Physics Reports-Review Section of Physics Letters* 200, 83 (1991).

[132] M. P. Anantram, and T. R. Govindan, Conductance of carbon nanotubes with disorder: A numerical study, *Phys. Rev. B* 58, 4882 (1998).

[133] H. Hu, B. Zhao, M. A. Hamon, K. Kamaras, M. E. Itkis, and R. C. Haddon, Sidewall functionalization of single-walled carbon nanotubes by addition of dichlorocarbene, *J. Am. Chem. Soc.* 125, 14893 (2003).

[134] M. Holzinger, O. Vostrowsky, A. Hirsch, F. Hennrich, M. Kappes, R. Weiss, and F. Jellen, Sidewall functionalization of carbon nanotubes, *Angew. Chem., Int. Ed.* 40, 4002 (2001).

[135] M. Holzinger, J. Abraha, P. Whelan, R. Graupner, L. Ley, F. Hennrich, M. Kappes, and A. Hirsch, Functionalization of single-walled carbon nanotubes with (R-)oxycarbonyl nitrenes, *J. Am. Chem. Soc.* 125, 8566 (2003).

[136] Z. F. Chen, S. Nagase, A. Hirsch, R. C. Haddon, W. Thiel, and P. V. Schleyer, Side-wall opening of single-walled carbon nanotubes (SWCNTs) by chemical modification: A critical theoretical study, *Angew. Chem., Int. Ed.* 43, 1552 (2004).

[137] H. J. Monkhorst, and J. D. Pack, Special points for Brillouin-zone integrations, *Phys. Rev. B* 13, 5188 (1976).

[138] CASTEP is a density functional theory package with a plane-wave pseudopotential method distributed by Accelrys Inc.; V. Milman, B. Winkler, J. A. White, C. J. Pickard, M. C. Payne, E. V. Akhmatskaya, R. H. Nobes, *Int. J. Quantum Chem.* 77, 895 (2000).

[139] Dmol3 is a density functional theory package based atomic basis distributed by Accelrys Inc.; B. Delley, *J. Chem. Phys.* 113, 7756 (2000).

[140] Q. Liu, and R. Hoffmann, Theoretical Aspects of a Novel Mode of Hydrogen-Hydrogen Bonding, *J. Am. Chem. Soc.* 117, 10108 (1995).

[141] R. Rytz, and G. Calzaferri, Electronic transition oscillator strengths in solids: An extended Huckel tight-binding approach, *J. Phys. Chem. B* 101, 5664 (1997).

[142] E. T. Mickelson, I. W. Chiang, J. L. Zimmerman, P. J. Boul, J. Lozano, J. Liu, R. E. Smalley, R. H. Hauge, and J. L. Margrave, Solvation of fluorinated single-wall carbon nanotubes in alcohol solvents, *J. Phys. Chem. B* 103, 4318 (1999).

[143] P. J. Boul, J. Liu, E. T. Mickelson, C. B. Huffman, L. M. Ericson, I. W. Chiang, K. A. Smith, D. T. Colbert, R. H. Hauge, J. L. Margrave, and R. E. Smalley, Reversible sidewall functionalization of buckytubes, *Chem. Phys. Lett.* 310, 367 (1999).

[144] S. Pekker, J. P. Salvetat, E. Jakab, J. M. Bonard, and L. Forro, Hydrogenation of carbon nanotubes and graphite in liquid ammonia, *J. Phys. Chem. B* 105, 7938 (2001).

[145] B. N. Khare, M. Meyyappan, A. M. Cassell, C. V. Nguyen, and J. Han, Functionalization of carbon nanotubes using atomic hydrogen from a glow discharge, *Nano Lett.* 2, 73 (2002).

[146] B. N. Khare, M. Meyyappan, J. Kralj, P. Wilhite, M. Sisay, H. Imanaka, J. Koehne, and C. W. Baushchlicher, A glow-discharge approach for functionalization of carbon nanotubes, *Appl. Phys. Lett.* 81, 5237 (2002).

[147] K. S. Kim, D. J. Bae, J. R. Kim, K. A. Park, S. C. Lim, J. J. Kim, W. B. Choi, C. Y. Park, and Y. H. Lee, Modification of electronic structures of a carbon nanotube by hydrogen functionalization, *Adv. Mater.* 14, 1818 (2002).

[148] R. K. Saini, I. W. Chiang, H. Q. Peng, R. E. Smalley, W. E. Billups, R. H. Hauge, and J. L. Margrave, Covalent sidewall functionalization of single wall carbon nanotubes, *J. Am. Chem. Soc.* 125, 3617 (2003).

[149] C. A. Dyke, and J. M. Tour, Solvent-free functionalization of carbon nanotubes, *J. Am. Chem. Soc.* 125, 1156 (2003).

[150] J. L. Bahr, and J. M. Tour, Highly functionalized carbon nanotubes using in situ generated diazonium compounds, *Chem. Mater.* 13, 3823 (2001).

[151] K. H. An, J. G. Heo, K. G. Jeon, D. Bae, C. S. Jo, C. W. Yang, C. Y. Park, Y. H. Lee, Y. S. Lee, and Y. S. Chung, X-ray photoemission spectroscopy study of fluorinated single-walled carbon nanotubes, *Appl. Phys. Lett.* 80, 4235 (2002).

[152] P. G. Collins, K. Bradley, M. Ishigami, and A. Zettl, Extreme oxygen sensitivity of electronic properties of carbon nanotubes, *Science* 287, 1801 (2000).

[153] G. U. Sumanasekera, C. K. W. Adu, S. Fang, and P. C. Eklund, Effects of gas adsorption and collisions on electrical transport in single-walled carbon nanotubes, *Phys. Rev. Lett.* 85, 1096 (2000).

[154] S. H. Jhi, S. G. Louie, and M. L. Cohen, Electronic properties of oxidized carbon nanotubes, *Phys. Rev. Lett.* 85, 1710 (2000).

[155] J. J. Zhao, A. Buldum, J. Han, and J. P. Lu, Gas molecule adsorption in carbon nanotubes and nanotube bundles, *Nanotechnology* 13, 195 (2002).

[156] G. U. Sumanasekera, B. K. Pradhan, H. E. Romero, K. W. Adu, and P. C. Eklund, Giant thermopower effects from molecular physisorption on carbon nanotubes, *Phys. Rev. Lett.* 89 (2002).

[157] H. J. Choi, J. Ihm, S. G. Louie, and M. L. Cohen, Defects, quasibound states, and quantum conductance in metallic carbon nanotubes, *Phys. Rev. Lett.* 84, 2917 (2000).

[158] C. C. Kaun, B. Larade, H. Mehrez, J. Taylor, and H. Guo, Current-voltage characteristics of carbon nanotubes with substitutional nitrogen, *Phys. Rev. B* 65 (2002).

[159] A. N. Andriotis, M. Menon, D. Srivastava, and G. Froudakis, Extreme hydrogen sensitivity of the transport properties of single-wall carbon-nanotube capsules, *Phys. Rev. B* 64, art. no. (2001).

[160] S. B. Fagan, A. J. R. da Silva, R. Mota, R. J. Baierle, and A. Fazzio, Functionalization of carbon nanotubes through the chemical binding of atoms and molecules, *Phys. Rev. B* 67 (2003).

[161] P. Delaney, H. J. Choi, J. Ihm, S. G. Louie, and M. L. Cohen, Broken symmetry and pseudogaps in ropes of carbon nanotubes, *Nature* 391, 466 (1998).

[162] P. Delaney, H. J. Choi, J. Ihm, S. G. Louie, and M. L. Cohen, Broken symmetry and pseudogaps in ropes of carbon nanotubes, *Phys. Rev. B* 60, 7899 (1999).

[163] J. J. Zhao, and J. P. Lu, A nonorthogonal tight-binding total energy model for molecular simulations, *Phys. Lett. A* 319, 523 (2003).

[164] A. H. Nevidomskyy, G. Csanyi, and M. C. Payne, Chemically active substitutional nitrogen impurity in carbon nanotubes, *Phys. Rev. Lett.* 91 (2003).

[165] H. Kim, J. Lee, S. J. Kahng, Y. W. Son, S. B. Lee, C. K. Lee, J. Ihm, and Y. Kuk, Direct observation of localized defect states in semiconductor nanotube junctions, *Phys. Rev. Lett.* 90, 216107 (2003).

[166] M. Melle-Franco, M. Marcaccio, D. Paolucci, F. Paolucci, V. Georgakilas, D. M. Guldi, M. Prato, and F. Zerbetto, Cyclic voltammetry and bulk electronic properties of soluble carbon nanotubes, *J. Am. Chem. Soc.* 126, 1646 (2004).

[167] E. Joselevich, Chemistry and electronics of carbon nanotubes go together, *Angew. Chem., Int. Ed.* 43, 2992 (2004).

[168] S. Frank, P. Poncharal, Z. L. Wang, and W. A. de Heer, Carbon nanotube quantum resistors, *Science* 280, 1744 (1998).

[169] T. W. Ebbesen, H. J. Lezec, H. Hiura, J. W. Bennett, H. F. Ghaemi, and T. Thio, Electrical conductivity of individual carbon nanotubes, *Nature* 382, 54 (1996).

[170] S. Sanvito, Y. K. Kwon, D. Tomanek, and C. J. Lambert, Fractional quantum conductance in carbon nanotubes, *Phys. Rev. Lett.* 84, 1974 (2000).

[171] H. T. Soh, C. F. Quate, A. F. Morpurgo, C. M. Marcus, J. Kong, and H. J. Dai, Integrated nanotube circuits: Controlled growth and ohmic contacting of single-walled carbon nanotubes, *Appl. Phys. Lett.* 75, 627 (1999).

[172] A. Bachtold, M. S. Fuhrer, S. Plyasunov, M. Forero, E. H. Anderson, A. Zettl, and P. L. McEuen, Scanned probe microscopy of electronic transport in carbon nanotubes, *Phys. Rev. Lett.* 84, 6082 (2000).

[173] J. Nygard, D. H. Cobden, and P. E. Lindelof, Kondo physics in carbon nanotubes, *Nature* 408, 342 (2000).

[174] L. F. Yang, J. W. Chen, H. T. Yang, and J. M. Dong, Quantum interference in carbon nanotube electron resonators, *Phys. Rev. B* 69, 153407 (2004).

[175] J. Jiang, J. M. Dong, and D. Y. Xing, Quantum interference in carbon-nanotube electron resonators, *Phys. Rev. Lett.* 91, 056802 (2003).

[176] W. J. Liang, M. Bockrath, D. Bozovic, J. H. Hafner, M. Tinkham, and H. Park, Fabry-Perot interference in a nanotube electron waveguide, *Nature* 411, 665 (2001).

[177] Z. Zhang, D. A. Dikin, R. S. Ruoff, and V. Chandrasekhar, Conduction in carbon nanotubes through metastable resonant states, *Europhys. Lett.* 68, 713 (2004).

[178] D. Orlikowski, M. B. Nardelli, J. Bernholc, and C. Roland, Theoretical STM signatures and transport properties of native defects in carbon nanotubes, *Phys. Rev. B* 61, 14194 (2000).

[179] M. P. Lopezsancho, J. M. Lopezsancho, and J. Rubio, Interpretation of the Electron-Energy-Loss Spectrum for Hydrogen-Covered Transition-Metal Surfaces in Terms of a Configuration-Interaction Approach, *Phys. Rev. B* 31, 4143 (1985).

[180] A. Buldum, and J. P. Lu, Contact resistance between carbon nanotubes, *Phys. Rev. B* 63 (2001).

[181] C. Buia, A. Buldum, and J. P. Lu, Quantum interference effects in electronic transport through nanotube contacts, *Phys. Rev. B* 67 (2003).

[182] D. Tomanek, and S. G. Louie, 1st-Principles Calculation of Highly Asymmetric Structure in Scanning-Tunneling-Microscopy Images of Graphite, *Phys. Rev. B* 37, 8327 (1988).

[183] J. C. Charlier, P. Lambin, and T. W. Ebbesen, Electronic properties of carbon nanotubes with polygonized cross sections, *Phys. Rev. B* 54, R8377 (1996).

[184] A. Rubio, D. Sanchez-Portal, E. Artacho, P. Ordejon, and J. M. Soler, Electronic states in a finite carbon nanotube: A one-dimensional quantum box, *Phys. Rev. Lett.* 82, 3520 (1999).